

Diss. ETH No. ...13925

Static Inductance Extraction by Means of the Monte Carlo Method and Comparison With Related Approaches

A dissertation submitted to the
SWISS FEDERAL INSTITUTE OF TECHNOLOGY
ZURICH

for the degree of
Doctor of Technical Sciences

presented by
GÖTZ LEONHARDT
Dipl.-Phys., Westfälische Wilhelms Universität Münster
born November 16th, 1967
citizen of Germany

accepted on the recommendation of
Prof. Dr. Wolfgang Fichtner, examiner
Dr. Niels Kuster, co-examiner

2000

Zusammenfassung

Die vorliegende Arbeit wurde im Rahmen des Swiss Priority Programms MINAST der schweizerischen Bundesregierung durchgeführt. Während dieser Arbeit wurden die Finite Element Methode, die Momentenmethode und die Methode der Finiten Differenzen im Zeitbereich im Hinblick auf ihre Eignung zur Induktivitätsbestimmung untersucht. Besonderes Augenmerk wurde dabei auf den entsprechenden Rechenaufwand gelegt, die Genauigkeit, die Robustheit, die Benutzerfreundlichkeit und die Automatisierbarkeit innerhalb einer kommerziellen Softwareumgebung.

Die Induktivitätsbestimmung von Leitergeometrien und eine darauf folgende Netzwerksimulation, bei der die elektrischen Leiter durch konzentrierte Elemente dargestellt werden, kann eine sehr effiziente Möglichkeit sein, die Ausbreitung von elektrischen Signalen zu berechnen. Ausserdem werden mit steigenden Frequenzen und dichteren Layouts induktive Effekte für das elektrische Verhalten von Schaltungen immer wichtiger. Die Signalverzögerung zu ignorieren oder eine Simulation nur mit Widerständen und Kapazitäten genügt oft nicht mehr. Diese Arbeit gibt einen Überblick über die Darstellung elektromagnetischer Felder auf Leiterbahnen mit Hilfe von Induktivitäten, Widerständen und Kapazitäten. Die Grenzen der verschiedenen Modelle werden diskutiert. Die theoretischen Grundlagen von Widerstand, Induktivität und Kapazität werden auch im Hinblick auf die jeweils geeigneten numerischen Methoden untersucht. Weil schon eine ganze Reihe von Methoden zur Kapazitätsbestimmung bekannt sind, ist es besonders interessant, ob und wie diese zur Induktivitätsbestimmung benutzt werden können.

Die zur Induktivitätsbestimmung benutzten Gleichungen sind einfach. Zahlreiche Veröffentlichungen behandeln dieses Thema schon seit Anfang des Jahrhunderts. Numerische Berechnungen sind aber immer noch

auf vergleichsweise kleine Leitergeometrien beschränkt. Wegen der langreichweitigen induktiven Wechselwirkung zwischen Leitern genügen die bekannten Methoden daher oft nicht mehr den industriellen Anforderungen. In dieser Arbeit wurden die Grenzen der Finite Element Methode und der Momentenmethode untersucht. Mögliche Verbesserungen durch den Einsatz hybrider Methoden werden diskutiert. Verschiedene Beispielgeometrien wurden ausgewählt um die Vor- und Nachteile dieser Methoden zu zeigen. Die Resultate von numerischer Induktivitätsbestimmung wurden innerhalb von Netzwerksimulationen benutzt, wobei die Ergebnisse mit denen der Methode der Finiten Differenzen im Zeitbereich und mit Messresultaten verglichen wurden.

Aufgrund der festgestellten Einschränkungen der bekannten Methoden wurde eine neue Methode zur statischen Induktivitätsbestimmung entwickelt. Diese basiert auf einer Berechnung der Stromdichteverteilung im Leiterinnern mit der Methode der Finiten Elemente und einer nachfolgenden Bestimmung der magnetischen Feldenergie mittels einer Monte Carlo Integration. Die Monte Carlo Integration konnte durch Einsatz verschiedener Varianzreduktionsverfahren stark beschleunigt werden. Wegen der geringen Speicheranforderungen der neu entwickelten Methode ist diese speziell geeignet für grosse und komplizierte Leitergeometrien. Sogar im Falle von kleineren Beispielen kann die neue Methode zum Teil mit der Momentenmethode bezüglich Zeitanforderung konkurrieren. Abschliessend wird ein Ausblick gegeben auf mögliche und sinnvolle Entwicklungen in der Zukunft, die auch eine Induktivitätsbestimmung unter Berücksichtigung des Skin Effektes ermöglichen.

Abstract

As part of the joint industry/university project MINAST funded by the Swiss Government, the Finite Element Method, the Method of Moments and the Finite Difference Time Domain Method have been examined with respect to their suitability for inductance extraction within a commercial software package. Special attention was paid to aspects like computational effort, accuracy, robustness, user-friendliness and automatizability.

Inductance extraction of conductor geometries and subsequent circuit simulation with interconnects represented by lumped elements can be an efficient way for simulating the electric signal propagation. Furthermore, due to increasing frequencies and denser layouts inductive effects of conductors become increasingly important for the electrical circuit behavior. Simply neglecting the signal delay on interconnects or modeling it with capacitances and resistances only often is no longer sufficient. This work presents a theory of the electro magnetic fields on interconnects in terms of inductances, resistances and capacitances. Limits are discussed for the validity of these lumped element models. The theory of resistances, capacitances and inductances is also given in order to clarify which numerical methods are suitable for their computation. Due to the fact that already a variety of methods exists for capacitance extraction it is particularly interesting how these methods can be used for inductance extraction.

The equations used for inductance extraction are simple. This topic is already covered by numerous publications dating back to the beginning of this century. Numerical simulations, however, are still limited to rather small conductor geometries. Due to the long range interaction between conductors introduced by inductive effects, however, existing numerical

methods often no longer meet the demand of industry. During this work the limits of the Finite Element Method and the Method of Moments have been investigated in detail. Hybrid methods are discussed with respect to possible improvements. Several examples have been chosen in order to show respective advantages and disadvantages. Inductance results have been used within circuit simulations and results have been compared with full wave simulation results from the Finite Difference Time Domain method and from measurements.

Due to some limitations encountered during the investigation of the already existing methods a new method for static inductance extraction based on a current density computation by means of the Finite Element Method and a subsequent magnetic field energy estimate by means of Monte Carlo sampling has been developed. The Monte Carlo sampling process could be highly accelerated with the use of variance reduction techniques. Due to low memory requirements the newly developed method is especially suited for large and complicated conductor geometries. Even in case of smaller examples the new method can compete with the Method of Moments with respect to time requirements. Finally an outlook is given on possible and reasonable future developments for inductance extraction including the skin effect.

Contents

1	Introduction	1
1.1	Motivation and Context of This Work	1
1.2	Chapter Abstracts	8
2	Full Wave Equations and Lumped Element Circuit Representation	9
2.1	The Maxwell Equations	10
2.2	Solution in the Frequency Domain	10
2.3	Use of Potentials	12
2.4	Full Wave Solution	12
2.5	Quasistatic Approximation	15
2.5.1	Electric Field and Capacitance	16
2.5.2	Capacitance Matrix	17
2.5.3	Magnetic Field and Inductance	22
2.5.4	Inductance Matrix	25
2.5.5	Electric Current and Resistance	28
2.5.6	Resistance Matrix	28

2.6	Static Approximation	30
2.7	Other Potential Formulations	31
2.8	Analytical Solutions	32
2.8.1	Impedance of a Rectangular Conductor	33
2.8.2	Skin Effect	34
2.9	Generation of Equivalent Circuits	36
2.9.1	Including Capacitances	36
2.9.2	Including Resistances	37
2.9.3	Merging RLC	38
2.9.4	Example	38
2.9.5	Validity	38
2.10	Conclusions	41
3	Application of the Finite Element Method	43
3.1	Boundary Conditions	44
3.1.1	Example	48
3.2	Grid Refinement	50
3.2.1	Example	52
3.3	Extraction of Magnetic Field Energy	54
3.4	More Realistic Examples	57
3.4.1	Results	60
3.5	Discussion	62
3.6	Quasistatic Approximation	64
3.7	Conclusions	65

4	Static Inductance Extraction by Means of the Monte Carlo Method	67
4.1	Monte Carlo Sampling	68
4.2	Error Estimate	68
4.3	Convergence	71
4.4	Implementation	75
4.4.1	Implementation of a Probability Density	75
4.5	Example Bonding Wire	77
4.6	Variance Reduction Techniques	79
4.6.1	Probability Densities 1 and 2	81
4.6.2	Probability Density 3	82
4.6.3	Probability Density 4	84
4.6.4	Probability Density 5	85
4.6.5	Computational Effort	86
4.7	Examples	86
4.7.1	DIP Package Lead Frame	87
4.7.2	Substrate	90
4.7.3	Meander and Coil	92
4.7.4	Further Analysis	94
4.7.5	IGBT Bus Bar	95
4.8	Conclusions	97
5	Related Approaches	99
5.1	Capacitance Extraction by Means of the Monte Carlo Method	99

5.1.1	Convergence	101
5.1.2	Inductance Extraction with Floating Random Walk	102
5.1.3	Current Density Computation	103
5.2	Method of Moments	104
5.3	PEEC Method	108
5.3.1	Examples	111
5.3.2	Meander and Coil	111
5.3.3	Substrate	113
5.4	Conclusions and Outlook	115
6	Comparison With Full Wave Results	117
6.1	Bonding Wire With FD-TD	118
6.2	Bonding Wire With Monte Carlo Algorithm	119
6.3	Results	120
6.4	Conclusion	121
7	Conclusions	123
A	Vector Calculus	125
A.1	Vector Calculus	125
A.2	Time Average of Complex Vector Fields	126
A.3	Divergence of the Magnetic Vector Potential	126
B	Symbols	127
B.1	Static Self- and Mutual-Inductance of Rectangular Con- ductors	128

Introduction

1.1 Motivation and Context of This Work

With increasing package densities, larger circuits and higher clock rates for circuit operation, electro magnetic properties of the electric interconnects cannot be neglected during development. This is because the circuit behavior is not only determined by the active elements such as transistors, but also by the delay of signals accumulated during propagation on interconnecting transmission lines, by cross talk between signal lines and radiation effects, or summarized, by the electro magnetic fields generated during circuit operation. During circuit development typically no emphasis is put on the use of advanced simulation programs. Thumb rules are used whenever possible and more complicated geometries are often treated as two dimensional problems. However, dense and complicated structures sometimes do not allow these approximations to be applied. Other simplifications are possible. Depending on the size of geometries and smallest electro magnetic wavelength sometimes the full set of the Maxwell equations has to be solved. However, due to today's still limited computational resources and time constraints during development only very small parts of a layout can be simulated in this way. In order to simulate larger parts of a circuit it is possible to describe the electro magnetic contact behavior of small parts of a layout with scattering parameters [1], use these results in a circuit simulator program and perform simulations on a higher model scale. Various possibilities exist in order to incorporate field simulation results into a circuit model. Frequency dependent scattering parameters can for example be used in time domain circuit simulations by means of recursive convolution algorithms, or lumped parameter models can be adjusted in order to best

reproduce the simulated field behavior.

If the wavelength is large compared to conductor dimensions, lumped elements such as resistors, capacitors and inductors can be extracted from conductor geometries directly. These can be inserted into a circuit model according to circuit topology. Lumped element models are handled by circuit simulation programs in a natural way. Circuit developers often possess a feeling of how certain lumped elements affect circuit operation, i.e. where to expect cross talk and damping and where to expect oscillations. On the other hand it is much more difficult to identify critical parts in a circuit layout, when only some S-parameter information is given. Extraction of lumped circuit elements directly from conductor geometries however signifies another approximation. Capacitances and inductances are extracted during separate simulations, where both characterize the same part of a conductor (Resistance values are extracted together with inductance values). Simulation results then have to be introduced into a circuit in some order. This order is not critical for the circuit behavior when the electrical conductor behavior is either mostly capacitive or mostly inductive. It is in fact critical for the circuit behavior when the resulting impedances of inductor and capacitor are in the same range of magnitude. In the latter case some experience is required in handling of these lumped element models. However, recently some work has been done in order to overcome this limitation.

This work mostly deals with numerical methods for inductance extraction. Despite the fact that already a large amount of work has been done in the area of magnetic field simulation, there still is a need for stable and fast algorithms which require less user interaction. The aim of this work was to find some “simple” solution for inductance extraction of three dimensional geometries including the skin effect. In order to do this, some of the most relevant techniques have been investigated. Since some of them can be used for capacitance extraction as well, capacitance extraction is also briefly covered. Theory starts from the Maxwell equations. Here it is shown how a problem can be decomposed into smaller problems since this is important in order to distribute computational load. Emphasis is put on static inductance extraction, because a new simulation algorithm has been developed in order to circumvent some problems arising from the use of other methods. During static inductance extraction all time derivatives of the corresponding field equations are set equal zero. It is shown that for a large class of applications this is an acceptable approximation.

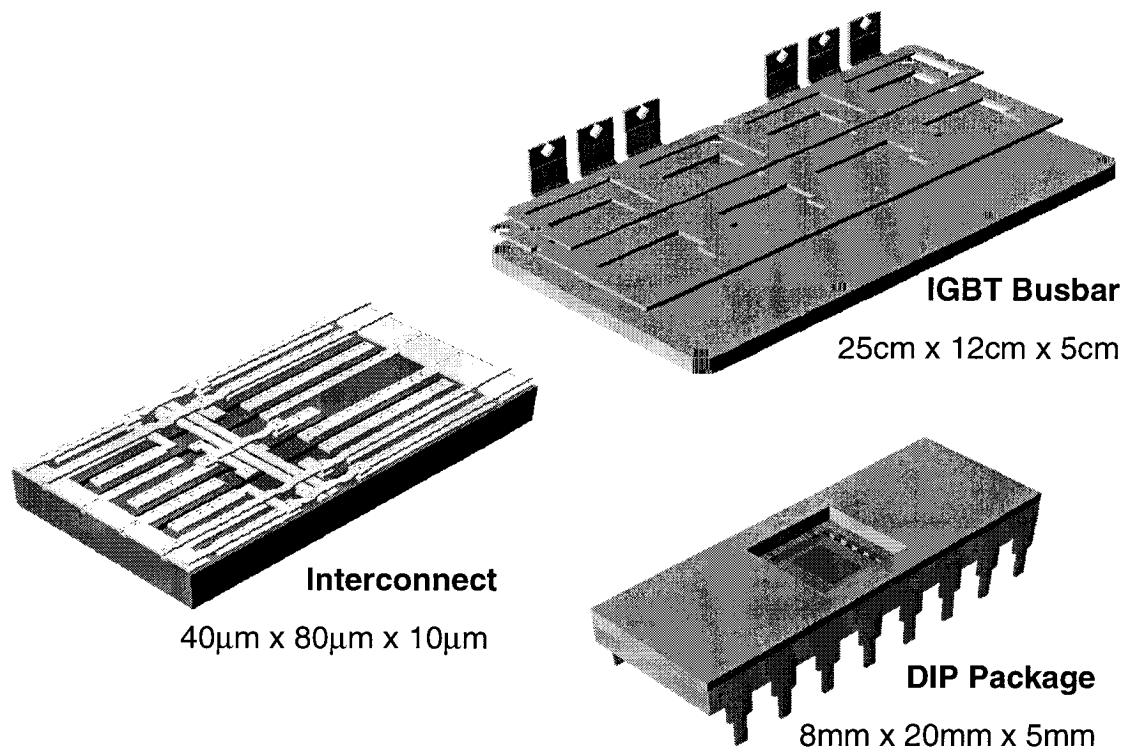


Figure 1.1: *Example geometries: The interconnect structure has been generated from a layout and process description. The DIP-Package has been designed manually. The IGBT-Busbar has been generated from an AutoCadTM boundary description (c.f. Fig. 1.2).*

Figure 1.1 shows some typical geometries for which three dimensional field simulations can be interesting during development. Note that in all examples many electrical contacts are distributed all over the geometries. They are typically connected with other - often nonlinear - parts of a circuit, which are not shown. Hence the electrical behavior of the conductors at their contacts is of primary interest. The field distribution inside the conductors and within their vicinity is of interest when it can somehow be related to the contact behavior. This information might be helpful for geometry optimization, e.g. when field singularities can be related to some malfunction of a circuit. In this case the geometry could be altered such that this singularity vanishes. However, relating field distributions to a certain electric contact behavior certainly would require a lot of experience and currently no general strategy is available for performing this task automatically. Today's typical approach for automatic geometry optimization is to introduce some parameters for geometry variation. Then a set of target values for optimization is defined, e.g. optimal signal transmission and minimum reflection. Field

simulations are performed with geometry parameters chosen by an optimization method. Finally the optimal set of geometry parameters is generated automatically.

Figure 1.1 also shows the size of geometries. All geometries shown have in common that typical electro magnetic wavelengths during operation are large compared to the largest dimension of the geometries. The shortest relevant wavelength λ_{min} can be estimated from the typical rise time t_r [2] with

$$\lambda_{min} \approx ct_r, \quad (1.1)$$

where c denotes the speed of light. Typical rise times are given in Tab. 1.1.

Geometry	t_r	f_r	λ_{min}
Interconnect	10^{-9} s	10^9 Hz	0.3m
DIP Package	10^{-8} s	10^8 Hz	3.0m
IGBT Busbar	10^{-6} s	10^6 Hz	300.0m

Table 1.1: *Smallest relevant wavelength λ_{min} estimated with Eq. (1.1) for conductor geometries shown in Fig. 1.1 and typical signal rise time t_r ($c = 3.0 \cdot 10^9$ m/s), and associated frequency f_r . Signal rise times in case of on-chip interconnect structures will become shorter within the near future [3], signal rise times for the DIP package are related to typical rise times in PCB design, the signal rise time occurring in high power module design where IGBT busbars are used for power transmission is taken from [4].*

As will be shown later within this work, this allows the use of lumped circuit elements for efficient description of the electro magnetic contact behavior with only a small error introduced. In case of the DIP package and the IGBT busbar example, capacitive effects are small. Hence the impedance between contacts is mostly inductive and resistive. The interconnect example however also exhibits strong capacitive behavior. Some current approaches dealing with this problem are briefly mentioned.

During this work, simulations have been embedded in a simulation flow as shown in Fig. 1.2. In order to carry out electro magnetic field simulations, some given geometry description has to be translated into a

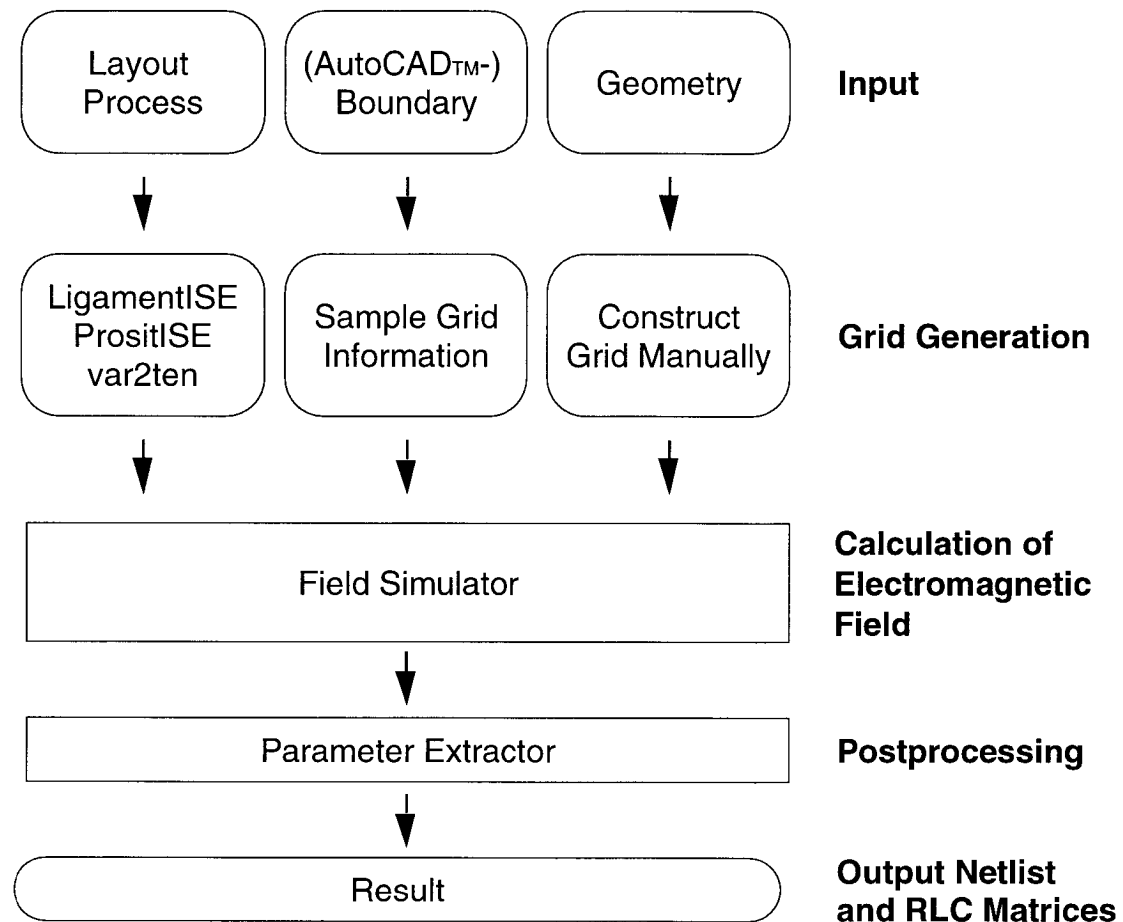


Figure 1.2: Schematic simulation flow with three possibilities for model generation. The result of an electro magnetic field simulation is a netlist, which can be used for further circuit simulations on a higher model scale.

grid model. This geometry description can be given in three ways. The least complicated interface is sketched on the right hand side in Fig. 1.2. Here, the grid is constructed manually in order to reflect all given geometry data. Constructing the grid manually can be cumbersome for complicated geometries with many corners and with many material interfaces. Another interface is sketched in the center of Fig. 1.2. Here, the geometry description is given in AutoCADTM Format, which is directly available after a geometry design with AutoCADTM. For the grid generation the distance between adjacent grid lines has to be defined. The material information is then sampled from the AutoCADTM description and inserted into the generated grid accordingly. The third interface is sketched on the left hand side in Fig. 1.2. This interface is suitable when the geometry is available as a layout and additional process information,

for example in case of an integrated circuit geometry. For processing the given geometry information during this work simulation tools from ISE [5, 6, 7] have been used. `LigamentISE` generates a command for the three dimensional process simulation program `PrositISE` and `var2ten` translates the geometry information into a structured grid.

For grid models basically two choices exist – structured grids and unstructured grids. In the case of structured grids the neighborhood of elements can be determined from element’s indices. The number of neighbors is constant for every grid element apart from grid elements located at grid boundaries. This fact sometimes leads to more grid elements than actually needed for an accurate simulation. Another choice are so called unstructured grids, where no such constraint exists. However grid generation itself is a difficult task and obtaining a valid grid automatically is not always guaranteed. Due to this fact, use of structured grids is favored during this work.

In some cases efficient recursive grid refinement techniques are used for error minimization [8]. After generation of the initial grid no new grid generation step is required during the simulation. Initial solutions are used for computation of a grid refinement indicator. This indicator shows where grid refinement is necessary for obtaining a better solution. Existing grid elements are subdivided where this indicator value is large. Computation of a refinement indicator and subsequent division of grid elements is repeated until a valid over all solution is obtained.

Generation of structured grids can be simple – typically a given topology is scanned and structured grid elements are initialized corresponding to the material hit in the given geometry description as in case of the IGBT-Busbar example in Fig. 1.1. The interconnect example shown in the same figure was generated from a pseudo process simulation with given layout and process description [5, 6]. Due to the Manhattan-style geometry, conversion of the geometry into a structured grid model is straightforward. The DIP-Package example in Fig. 1.1 was generated manually, i.e. grid lines and material information was edited manually with use of the structured grid editor `TEDISE` [9]. The simulation flow is shown in Fig. 1.2). Designing a grid manually is of course the most time consuming way of setting up a simulation. However, due to still existing difficulties in the field of automatic model generation, this task sometimes cannot be avoided.

Once the geometry description has been translated into a grid model,

electric contacts have to be placed where currents enter and leave the conductors. In case of the interconnect example contacts are placed automatically where conductors touch grid boundaries. Since the border of a simulation domain corresponds to the generated grid boundary, this naturally corresponds to what an engineer expects when he selects a simulation domain from a layout, when interconnects intersect with the boundary of the simulation domain. In case of the DIP package and the IGBT busbar example, contacts have to be placed automatically, because contact locations currently cannot be deduced from a geometry description (However, this is only a matter of standardization. Once contacts can be defined within geometry descriptions, they can be translated into a corresponding grid model as well).

After an introduction into the relevant theory and possible formulations, static inductance extraction by means of the Finite Element Method is investigated. Because of some limitations a new method for static inductance extraction with very low memory requirements has been developed. It is based on current density computations by means of the Finite Element Method with subsequent energy estimates by means of Monte Carlo sampling. The sampling is highly accelerated with use of different variance reduction techniques. Then inductance extraction by means of the multipole accelerated Moment Method is discussed and compared with Monte Carlo sampling. Results are compared with broad band measurements and full wave simulations carried out with the Finite-Difference Time-Domain method. In this context also the limit of lumped element approximations is demonstrated. An outlook is given on how to proceed and extend the capabilities of existing approaches to inductance extraction towards more complicated geometries.

Some results on inductance extraction by means of the Monte Carlo method have been presented at conferences [10, 11], one journal contribution presents the comparison of full wave simulation results with measurement results and results obtained from lumped element circuit simulation [12] and one journal contribution gives an extended insight into the newly developed static inductance extraction by means of the Monte Carlo method [13]. The newly developed method for static inductance extraction has also been commercialized [14] during this work. It is coupled with the Finite Element program `SOLIDISISE`, which supplies current density and electric field simulation results. Simulation results are post processed and equivalent circuit models are generated.

1.2 Chapter Abstracts

The following chapters of this thesis are organized as follows.

Chapter 2 – deals with formulations of the Maxwell equations in the frequency domain, with the static and quasistatic approximation and with basic simulation concepts like net list generation for circuit simulation from resistance, inductance and capacitance matrices. It is shown how models can be partitioned in order to distribute computational load and how circuit models are automatically constructed by the newly developed program.

Chapter 3 – discusses the three dimensional static inductance extraction by means of the Finite Element Method and possible extensions to inductance extraction including the skin effect.

Chapter 4 – presents the new approach for static inductance extraction by means of current density computations with the Finite Element method and subsequent energy estimates by means of Monte Carlo sampling. Several variance reduction techniques are combined and used for acceleration of the sampling process.

Chapter 5 – reviews some related approaches like the floating random walk method and the multipole accelerated Moment method. Possible extensions and limitations are also discussed. The newly developed method is compared with related approaches where possible.

Chapter 6 – briefly reviews the Finite-Difference Time-Domain method for full wave simulation in the time domain and gives examples and comparisons with full wave measurement and lumped element simulation results.

Chapter 7 – summarizes the work and gives an outlook towards possible future developments.

Full Wave Equations and Lumped Element Circuit Representation

This chapter reviews the Maxwell equations in the context of modeling the electro magnetic behavior of metallic interconnects. Starting from the full wave equations, potential formulations are reviewed which require less unknowns to be solved than the full set of Maxwell equations. The quasistatic approximation is motivated and the static approximation is reviewed, both with respect to the errors introduced and the gain achieved in terms of reducing the complexity of the problem. When possible, respective field solutions are related to lumped elements such as resistors, inductors and capacitors. These lumped elements can be introduced into a circuit model in order to reflect the electromagnetic contact behavior with a minimal number of parameters. Circuit models can be used within a circuit simulator like SPICE [15] for simulations on a higher model scale, i.e. multiple circuit models can easily be coupled and active elements like transistors can also be included. Representation of the electromagnetic contact behavior by means of lumped element models introduces a further field approximation, which is also discussed. Basic field theory is given in order to clarify which field variables are mandatory and in order to clarify which further simplifications could be carried out.

Numerical methods are treated within the following chapters. However, the following chapters will often refer to the theory presented in this chapter. Circuit model results are compared with full wave solutions

and measurements in the final chapter.

2.1 The Maxwell Equations

The governing equations of classical electrodynamics are the Maxwell equations [16] which consist of a system of coupled partial differential equations

$$\nabla \cdot \mathbf{D}(\mathbf{r}, t) = \rho(\mathbf{r}, t) \quad (2.1a)$$

$$\nabla \cdot \mathbf{B}(\mathbf{r}, t) = 0 \quad (2.1b)$$

$$\nabla \times \mathbf{E}(\mathbf{r}, t) = -\frac{\partial}{\partial t} \mathbf{B}(\mathbf{r}, t) \quad (2.1c)$$

$$\nabla \times \mathbf{H}(\mathbf{r}, t) = \mathbf{J}(\mathbf{r}, t) + \frac{\partial}{\partial t} \mathbf{D}(\mathbf{r}, t). \quad (2.1d)$$

Further material relations exist which relate the magnetic flux density to magnetic field, electric displacement current to electric field and electric current density to electric field

$$\mathbf{B}(\mathbf{r}, t) = \mu \mathbf{H}(\mathbf{r}, t) \quad (2.2a)$$

$$\mathbf{D}(\mathbf{r}, t) = \varepsilon \mathbf{E}(\mathbf{r}, t) \quad (2.2b)$$

$$\mathbf{J}(\mathbf{r}, t) = \sigma \mathbf{E}(\mathbf{r}, t). \quad (2.2c)$$

The material parameters are the magnetic permeability μ , the dielectric permittivity ε and the electric conductivity σ .

In typical applications only isotropic materials are involved and simulation methods are investigated with scalar material parameters only. Moreover, typical circuit packages are usually composed of homogeneous materials. Hence, all material parameter variations are step function like. The magnetic permeability μ is assumed constant, as magnetic materials are not treated. It is further assumed, that ε and σ do not depend on the electric field strength, on the frequency or on the temperature. The later assumptions lead to a linear system of equations.

2.2 Solution in the Frequency Domain

Electric circuits are operated in the time domain, i.e. contacts are excited with time dependent signals and therefore only time dependent

circuit simulation results can tell that a circuit does actually operate as desired. However, an electromagnetic characterization of conductors in time domain cannot be reused during different circuit simulations. The computational intensive three-dimensional field simulations have to be redone each time a circuit is simulated with different excitation. A solution is to perform electromagnetic field simulations in frequency domain and include frequency dependent results in time domain circuit simulations.

Here, the following time periodic behavior of all field variables f is assumed

$$f(\mathbf{r}, t) = \Re[\hat{f}(\mathbf{r})e^{j\omega t}]. \quad (2.3)$$

In Eq. (2.3) $f(\mathbf{r}, t)$ stands for a single field variable, \mathbf{r} and t denote location and time respectively and ω denotes the angular frequency of the field. The term $\hat{f}(\mathbf{r})e^{j\omega t}$ is the phasor representation of f . Note that only the real part of the phasor representation has a physical meaning and the complex number \hat{f} carries the phase information [17]. A clear disadvantage of frequency domain simulations is the use of complex variables whereas in time domain calculations only real variables are required.

Since linear superpositions of single frequency solutions also fulfill the linearized Maxwell equations, Fourier transformation algorithms can be used for the derivation of time domain results. Another more efficient possibility for incorporation of frequency domain results into time domain simulations is the use of recursive convolution algorithms. Recursive convolution algorithms first appeared in the context of modeling of dispersive media in time domain simulations [18, 19]. Integration of frequency domain models into time domain circuit simulations has been demonstrated in [20, 21, 22]. Recursive convolution algorithms require the frequency behavior to be represented as a rational polynomial. A very efficient technique for generation is **A**symptotic **W**aveform **E**valuation (AWE) [23]. Guaranteed stable models can be generated with **P**adé approximation via the **L**anczos Process (PVL) [24].

From here on, whenever not explicitly stated, the phasor representation is used for all field variables f . Therefore notation with the “hat” symbol for complex variables and the time dependence $e^{j\omega t}$ are omitted. With predefined time periodic field behavior, the time derivative $\partial/\partial t$ becomes

$j\omega$ and the Maxwell equations Eqs. (2.1c-2.1d) are

$$\nabla \times \mathbf{E}(\mathbf{r}) = -j\omega\mathbf{B}(\mathbf{r}) \quad (2.4a)$$

$$\nabla \times \mathbf{H}(\mathbf{r}) = \mathbf{J}(\mathbf{r}) + j\omega\mathbf{D}(\mathbf{r}). \quad (2.4b)$$

With use of the material relations, all field variables can be deduced from six scalars only, e.g. from fields \mathbf{E} and \mathbf{H} .

2.3 Use of Potentials

In this section, potential formulations are reviewed which further reduce the number of field variables necessary for a complete field description.

The magnetic vector potential \mathbf{A} [25] with

$$\mathbf{B}(\mathbf{r}, \omega) = \nabla \times \mathbf{A}(\mathbf{r}) \quad (2.5)$$

fulfills Eq. 2.1b automatically, because $\nabla \cdot (\nabla \times \mathbf{f}) = 0$ for any vector field \mathbf{f} . Equation (2.5), however, does not yield a unique definition for \mathbf{A} , because the gradient of a scalar field $\nabla\Phi$ can be added without change of the curl of the sum. Useful definitions of \mathbf{A} depend on respective approximations of the Maxwell equations and are given below.

From Eqs. (2.4a) and (2.5) it follows that

$$\nabla \times \mathbf{E}(\mathbf{r}) = -j\omega\nabla \times \mathbf{A}(\mathbf{r}). \quad (2.6)$$

The curl operator is applied to both sides of Eq. (2.6). The difference between fields \mathbf{E} and \mathbf{A} can hence be only the gradient of a scalar field, e.g. $\nabla\Phi$,

$$\mathbf{E}(\mathbf{r}) = -j\omega\mathbf{A}(\mathbf{r}) - \nabla\Phi(\mathbf{r}). \quad (2.7)$$

2.4 Full Wave Solution

With Eq. (2.1a) and material relation Eq. (2.2b) it follows that

$$\nabla\mathbf{E} = -j\omega\nabla\mathbf{A} - \Delta\Phi = \frac{\rho}{\varepsilon} \quad (2.8)$$

Note that during derivation of Eq. (2.8), the dielectric permittivity has been set constant in space. In order to solve for a complete field distribution, solutions in domains with each constant dielectric permittivity have to be matched at the domain boundaries. For matching conditions c.f. [25].

With use of the vector identity Eq. (A.2) the curl of the magnetic field in Eq. (2.1d) can be written as

$$\nabla \times \mathbf{H} = \frac{1}{\mu}(\nabla \nabla \mathbf{A} - \Delta \mathbf{A}). \quad (2.9)$$

Note that in Eq. (2.9) the magnetic permeability μ has been set constant as assumed in Sec. 2.1. Equation (2.1d) is reformulated with Eqs. (2.7) and (2.2b).

$$\nabla \nabla \mathbf{A} - \Delta \mathbf{A} = \mu \mathbf{J} + \mu \varepsilon (\omega^2 \mathbf{A} - \nabla \dot{\Phi}) \quad (2.10)$$

The Helmholtz Theorem states that vector fields are defined when both curl and divergence are defined. Here, the ‘‘Lorentz Gauge’’ [25]

$$\nabla \mathbf{A} = -j\omega \varepsilon \mu \dot{\Phi} \quad (2.11)$$

is a useful definition of the divergence of \mathbf{A} . Equation (2.8) simplifies to

$$\Delta \Phi + \omega^2 \varepsilon \mu \Phi = -\frac{\rho}{\varepsilon}, \quad (2.12)$$

and Eq. (2.10) becomes

$$\Delta \mathbf{A} + \omega^2 \varepsilon \mu \mathbf{A} = -\mu \mathbf{J}. \quad (2.13)$$

Equations (2.12) and (2.13) are both inhomogeneous Helmholtz equations with one and three components, respectively. Solutions can be obtained with use of Green’s functions G

$$(\Delta + k^2)G(\mathbf{r}, \mathbf{r}') = -4\pi\delta(\mathbf{r} - \mathbf{r}'), \quad (2.14)$$

where $k^2 = \omega^2 \varepsilon \mu$, δ stands for the delta-function and

$$G^\pm(\mathbf{r}, \mathbf{r}') = \frac{e^{\pm jk|\mathbf{r}-\mathbf{r}'|}}{|\mathbf{r} - \mathbf{r}'|}. \quad (2.15)$$

In Eq. (2.15) the plus-minus sign denotes expanding and contracting waves respectively. This can be deduced from the full solution in time, which is given by

$$G^\pm(\mathbf{r}, \mathbf{r}', t) = G^\pm(\mathbf{r}, \mathbf{r}')e^{j\omega t}. \quad (2.16)$$

With the “plus” sign and increasing time, the phase argument $+k|\mathbf{r} - \mathbf{r}'| + \omega t$ stays constant when the distance $|\mathbf{r} - \mathbf{r}'|$ decreases. Hence the “plus”-sign corresponds to incoming waves. The “minus”-sign leads to inverse behavior and hence corresponds to outgoing waves. Since initially fields are zero at infinity, only outgoing waves and hence only the “minus” sign is considered during the following analysis.

The full inhomogeneous solution of Eq. (2.12) is calculated by superposition of Green’s functions

$$\Phi(\mathbf{r}) = \frac{1}{4\pi\epsilon} \int_V \frac{\rho(\mathbf{r}')e^{-jk|\mathbf{r}-\mathbf{r}'|}}{|\mathbf{r} - \mathbf{r}'|} d^3r'. \quad (2.17)$$

The same holds for the three solutions (one for every coordinate direction) of Eq. (2.13)

$$A_i(\mathbf{r}) = \frac{1}{4\pi\epsilon} \int_V \frac{J_i(\mathbf{r}')e^{jk|\mathbf{r}-\mathbf{r}'|}}{|\mathbf{r} - \mathbf{r}'|} d^3r', \quad (2.18)$$

where $i = x, y, z$ denotes the respective coordinate direction.

When current and charge densities are given, computation of a field solution with Eqs. (2.17) and (2.18) is straight forward. However, since the electromagnetic contact behavior is typically characterized by S-parameters or impedance values, current and charge densities have to be computed, too, when either the electric potentials at contacts or the total conductor currents are known.

In order to solve for the three unknown components of $\mathbf{J}(\mathbf{r})$ and the unknown field $\rho(\mathbf{r})$, four additional equations are required. The current density $\mathbf{J}(\mathbf{r})$ can be calculated with Eq. (2.7) and material relation Eq. (2.2c). The charge density $\rho(\mathbf{r})$ can be calculated from the continuity equation

$$\nabla\mathbf{J}(\mathbf{r}) + j\omega\rho(\mathbf{r}) = 0, \quad (2.19)$$

which has always to be fulfilled [1]. Use of Eq. (2.19) however introduces a coupling into Eqs. (2.17) and (2.18). Therefore these equations cannot be solved independently.

2.5 Quasistatic Approximation

The quasistatic approximation reduces the mathematical complexity of the Maxwell equations and leads to results with sufficient accuracy, when certain conditions are met. The influence of the displacement current in Eq. (2.4b) is small when

$$\sigma \gg \omega \varepsilon. \quad (2.20)$$

Equation (2.20) is fulfilled in conducting media for even high frequencies, because $\varepsilon = 8.85 \cdot 10^{-12} \text{F/m}$ is a small number and the electrical conductivity of metals is typically $\sigma > 10^7 \text{S/m}$. Within this approximation, the time derivative of the displacement current $\partial/\partial t \mathbf{D}$ in Eq. (2.1d) is discarded leading to

$$\nabla \times \mathbf{H}(\mathbf{r}) = \mathbf{J}(\mathbf{r}). \quad (2.21)$$

Following the same steps as in Sec. 2.4, this simplification leads to a difference in Eq. (2.10)

$$\nabla \nabla \mathbf{A} - \Delta \mathbf{A} = \mu \mathbf{J}. \quad (2.22)$$

Here, the ‘‘Coulomb Gauge’’ [25] $\nabla \mathbf{A} = 0$ is better suited for adjustment of $\nabla \mathbf{A}$. Equation (2.8) then reduces to

$$\Delta \Phi = -\frac{\rho}{\varepsilon} \quad (2.23)$$

and Eq. (2.22) becomes

$$\Delta \mathbf{A} = -\mu \mathbf{J}. \quad (2.24)$$

Both equations are inhomogeneous Laplace equations and can be solved with use of Green’s functions

$$\Delta G(\mathbf{r}, \mathbf{r}') = -4\pi \delta(\mathbf{r} - \mathbf{r}'), \quad (2.25)$$

where in this case

$$G(\mathbf{r}, \mathbf{r}') = \frac{1}{|\mathbf{r} - \mathbf{r}'|}. \quad (2.26)$$

The difference between Eq. (2.15) and Eq. (2.26) is the missing retardation term $e^{-jk|\mathbf{r}-\mathbf{r}'|}$, which accounts for the wave propagation delay

in case of the full wave solution. Since there is no wave propagation delay within the quasistatic approximation, the wave velocity appears to be infinite. Obviously this approximation yields good results, when the wavelength is large compared to the conductor dimensions.

As in the previous section, fields Φ and \mathbf{A} can be calculated directly when charge and currents are known.

$$\Phi(\mathbf{r}) = \frac{1}{4\pi\epsilon} \int_V \frac{\rho(\mathbf{r}')}{|\mathbf{r} - \mathbf{r}'|} d^3r' \quad (2.27)$$

and for the three coordinate directions separately

$$A_i(\mathbf{r}) = \frac{\mu}{4\pi} \int_V \frac{J_i(\mathbf{r}')}{|\mathbf{r} - \mathbf{r}'|} d^3r', \quad (2.28)$$

where $i = x, y, z$ denotes the respective coordinate direction.

In order to calculate the electromagnetic contact behavior, one could basically follow the steps in the preceding section Sec. 2.4. However, one more simplification can be applied when considering that electric and magnetic field are “basically” decoupled within this approximation [26]. Generally electric and magnetic fields always are coupled, because one field can be determined from the other by Eqs. (2.1c) and (2.1d). However when time derivatives become smaller, due to small coupling, this task becomes increasingly difficult to perform (by means of measurements or from numerical simulation results). It is therefore a common engineering approach [26] to simulate (and measure) electric and magnetic field independently. Note, that still only limited theoretical foundation is available for this decoupling behavior in case of general geometries.

2.5.1 Electric Field and Capacitance

This section describes the calculation of the electric field only. With appropriate boundary conditions, the electric field can be described with a capacitance value. Several ways are presented to compute a capacitance value.

When $\mathbf{B} = \mathbf{0}$ it follows from Eqs. (2.5) and (2.7) that $\mathbf{A} = \mathbf{0}$. The electric field can now be calculated from the scalar potential alone.

$$\mathbf{E} = -\nabla\Phi \quad (2.29)$$

From Eq. (2.23) it is known that Φ depends entirely on ρ . For an over-all characterization of the field for a given potential the **capacitance**

$$C = \frac{Q}{U} \quad (2.30)$$

can be used. In Eq. (2.30) Q denotes the total conductor charge and U denotes the respective *constant* potential between conductor and infinity. The total conductor charge can be calculated with Gauss' law

$$Q = \int_{\Gamma} -\varepsilon \nabla \Phi d\Gamma, \quad (2.31)$$

where Γ is a closed surface around the conductor and $d\Gamma$ denotes the outward normal on Γ . Because of the constant conductor potential, inside conductors $\rho = 0$. This is true for frequencies where metals serve as electric conductors. Conductors are separated by insulators where also $\rho = 0$. Therefore the Laplace equation Eq. (2.23) has to be solved with $\Phi = 1V$ on the conductor surface and $0V$ at infinity

$$\Delta \Phi(\mathbf{r}) = 0. \quad (2.32)$$

Note that with non constant dielectric permittivity ε Eq. (2.32) becomes [25]

$$\nabla \varepsilon(\mathbf{r}) \nabla \Phi(\mathbf{r}) = 0. \quad (2.33)$$

The conductor charge can also be determined from a solution of the corresponding integral equation Eq. (2.27) where ρ in fact denotes a surface charge and $Q = \int_V \rho(\mathbf{r}) d^2r$ with V the conductor surface. When electric field and electric displacement current are available inside the insulator, C can be calculated from the electric field energy [25].

$$\begin{aligned} W &= \frac{1}{2} C U^2 \\ &= \frac{1}{2} \int_V \mathbf{E}(\mathbf{r}) \mathbf{D}(\mathbf{r}) d^3r \end{aligned} \quad (2.34)$$

2.5.2 Capacitance Matrix

The capacitive behavior of a multi conductor-system is described by a capacitance matrix $\underline{\mathbf{C}}$ with

$$\underline{\mathbf{C}} \mathbf{U} = \mathbf{Q}. \quad (2.35)$$

In Eq. (2.35) \mathbf{U} denotes the vector of conductor potentials and \mathbf{Q} denotes the vector of total conductor charges. Capacitance matrix entries C_{ij} correspond to charges accumulated on conductor j , when an electric potential of 1V is applied to conductor i and all other conductors are kept at zero potential. Note that only the inverse relation Eq. (2.27) between charge and potential is available directly.

With N_C conductors, N_C linear independent vectors of conductor potentials U_i and corresponding vectors of total conductor charges Q_i are required for calculation of all entries in $\underline{\mathbf{C}}$. The matrix $\underline{\mathbf{C}}$ can then be calculated with Eq. (2.35). As in the previous section, total conductor charges can be calculated with Gauss's law Eq. (2.31). Furthermore, Q can be calculated by integration of surface charges when the integral equation approach Eq. (2.27) is used. Third, capacitance matrix entries can be calculated from the electric field energy. The electric field energy of a given electric potential distribution is [25]

$$\begin{aligned} W_{ii} &= \frac{1}{2} \mathbf{U}_i^T \underline{\mathbf{C}} \mathbf{U}_i \\ &= \frac{1}{2} \int_V \mathbf{E}_i(\mathbf{r}) \mathbf{D}_i(\mathbf{r}) d^3r, \end{aligned} \quad (2.36)$$

where fields $\mathbf{E}_i(\mathbf{r})$ and $\mathbf{D}_i(\mathbf{r})$ belong to the i -th vector of conductor potentials U_i . Single entries in the capacitance matrix can be calculated by choosing $U_{ij} = 1\text{V}$, when $i = j$ and $U_{ij} = 0\text{V}$, when $i \neq j$ with U_{ij} the j -th column of the i -th vector of conductor potentials. Then in Eq. (2.36) $\mathbf{U}_i^T \underline{\mathbf{C}} \mathbf{U}_j = C_{ij}$. From Eq. (2.34) one also knows that

$$\frac{1}{2} (U_i + U_j)^T \underline{\mathbf{C}} (U_i + U_j) = \frac{1}{2} \int_V (\mathbf{E}_i(\mathbf{r}) + \mathbf{E}_j(\mathbf{r})) (\mathbf{D}_i(\mathbf{r}) + \mathbf{D}_j(\mathbf{r})) d^3r$$

Hence with these conductor potentials

$$C_{ij} = \int_V \mathbf{E}_i(\mathbf{r}) \cdot \mathbf{D}_j(\mathbf{r}) d^3r. \quad (2.37)$$

According to [27], entries in the capacitance matrix $\underline{\mathbf{C}}$ have the following features:

1. Since Eq. (2.37) is symmetric in i and j , also C is symmetric, i.e. $C_{ij} = C_{ji}$.

2. $C_{ii} > 0 \forall i$. When conductor i is placed at some positive potential and all other conductors are placed at zero potential, conductor i must carry a positive charge.
3. $C_{ij} < 0 \forall j \neq i$. When all other conductors are placed at zero potential, they must carry a negative charge. Hence, all entries in \mathbf{C} generally are nonzero. Conductors can be shielded by covering them with a material with high dielectric permittivity.
4. $\sum_j C_{ij} \geq 0 \forall i$. The sum of capacitance matrix entries in row i equals the sum of all conductor charges, when 1V electric potential is applied to conductor i and 0V is applied to all other conductors. Between conductors, the electric displacement current is divergence free. Hence the sum of flux integrals Eq. (2.31) is zero, when there exists an outer boundary around the system of conductors with no electric field penetration. The sum is greater than zero, when electric field flux emanates towards infinity. When the sum of row entries vanishes, the capacitance matrix is singular, because one column can be determined from the other columns.
5. \mathbf{C} is positive definite, because the electric field energy $1/2 \mathbf{U}^T \mathbf{C} \mathbf{U} > 0 \forall \mathbf{U} \neq 0$.
6. When different conductors i and j are electrically connected and thus a new conductor with index λ is formed, the reduced capacitance matrix $\tilde{\mathbf{C}}$ can be computed by setting potentials $U_i = U_j = 1\text{V}$ and all other conductor potentials to 0V. The new diagonal entry can be calculated from the total conductor charge. It is given by $\tilde{C}_{\lambda\lambda} = C_{ii} + C_{jj} + C_{ij} + C_{ji}$. Off diagonal entries are given by $C_{\lambda k} = C_{ik} + C_{jk}$.

Some numerical methods are based on a partitioning of conductor surfaces. The capacitance matrix of the partitions is often called the matrix of *partial* capacitances [28, 1]. The electrical behavior of single partitions is then described with analytical formulas. A complicated capacitor can hence be understood as a system of small capacitors. The total capacitance can be calculated with feature (6) by successively combining conductors. When electric field flux starts from the system of conductors towards infinity, feature (4) becomes $\sum_j C_{ij} > 0 \forall i$. Then the capacitance matrix \mathbf{C} is an M-matrix. Proof: Because of feature (2) and (3) \mathbf{C} is non singular. Consider matrix \mathbf{B} with

$$\mathbf{B} = \mathbf{1} - \mathbf{D}^{-1} \mathbf{C}$$

and $\underline{\mathbf{D}}$ the diagonal of $\underline{\mathbf{C}}$. With features (2) and (3) it follows that all entries $B_{ij} \geq 0$ and

$$\sum_j B_{ij} < 1 \quad \forall i.$$

Hence, the largest eigenvalue of $\underline{\mathbf{B}}$ is smaller than 1. It is shown in [29] that the inverse of $\underline{\mathbf{D}}^{-1}\underline{\mathbf{C}}$ can be computed with a Neumann expansion

$$\underline{\mathbf{D}}\underline{\mathbf{C}}^{-1} = \sum_i \underline{\mathbf{B}}^i. \quad (2.38)$$

Hence, all entries of the inverse capacitance matrix are positive. This feature, non singularity of $\underline{\mathbf{C}}$ plus features (2) and (3) satisfy the requirements for $\underline{\mathbf{C}}$ to be an M-matrix. Note, that because of feature (2) also the inverse $\underline{\mathbf{C}}^{-1}$ is dense, as could be expected, because $\underline{\mathbf{C}}^{-1}$ is related to Eq. (2.27).

In order to estimate the range of a capacitive interaction between conductors, one has to solve either Eq. (2.29) or Eq. (2.27) with given electric conductor potential. However, an heuristic estimate can be obtained by assuming a very simple relation between charge and potential. Consider two conductors with distance much larger than their dimensions. Then Eq. (2.27) can be split into two parts. The “self” part is given by

$$\Phi_{\text{self}} = \frac{1}{4\pi\epsilon} \int_{\Gamma_{\text{self}}} \frac{\rho(\mathbf{r}')}{|\mathbf{r} - \mathbf{r}'|} d\Gamma_{\text{self}}, \quad (2.39)$$

where both \mathbf{r} and \mathbf{r}' are located on the same conductor. The singularity in Eq. (2.39) does not lead to infinite electric potentials. As an example geometry a disc with radius R and constant charge density ρ is considered. U is evaluated in the center of the disc, i.e. where the singularity is located

$$\begin{aligned} \Phi(0) &= \frac{1}{4\pi\epsilon} \int_{x^2+y^2 < R^2} \frac{\rho}{\sqrt{x^2+y^2}} dx dy \\ &= \frac{1}{4\pi\epsilon} \int_0^R \frac{\rho}{r} 2\pi r dr \\ &= \frac{1}{2\epsilon} \rho R. \end{aligned} \quad (2.40)$$

If $Q_{\text{self}} = \pi\rho R^2$ denotes the total charge on the conductor, the “self” part Eq. (2.39) can be approximated with a constant

$$\Phi_{\text{self}} \approx aQ_{\text{self}}. \quad (2.41)$$

The “coupling” part is similar to Eq. (2.39)

$$\Phi_{\text{coupling}} = \frac{1}{4\pi\epsilon} \int_{\Gamma_{\text{other}}} \frac{\rho(\mathbf{r}')}{|\mathbf{r} - \mathbf{r}'|} d\Gamma_{\text{other}}. \quad (2.42)$$

In Eq. (2.42) \mathbf{r} and \mathbf{r}' are located on different conductors. Since the average distance $|\mathbf{r} - \mathbf{r}'|$ is larger than the distance in the self contribution Eq. (2.39), ρ being constant, Φ_{coupling} is smaller than Φ_{self} . Moreover, when the two conductors are sufficiently apart, the relative change of the distance during integration is small. In this case Eq. (2.42) can be approximated by a constant b divided by the average conductor distance \bar{r} . Here, Q_{other} denotes the total charge on the other conductor

$$\Phi_{\text{coupling}} \approx \frac{b}{\bar{r}} Q_{\text{other}}. \quad (2.43)$$

In matrix notation Eqs. (2.41) and (2.43) are given by

$$\begin{pmatrix} a & b/\bar{r} \\ b/\bar{r} & a \end{pmatrix} \begin{pmatrix} Q_1 \\ Q_2 \end{pmatrix} = \begin{pmatrix} \Phi_1 \\ \Phi_2 \end{pmatrix}, \quad (2.44)$$

where indices 1 and 2 denote different conductors. The inverse of Eq. (2.44) can be calculated analytically. According to Eq. (2.35), this is the capacitance matrix of the two conductor system

$$\begin{pmatrix} a/(a^2 - b^2/\bar{r}^2) & -b/(a^2\bar{r} - b^2/\bar{r}) \\ -b/(a^2\bar{r} - b^2/\bar{r}) & a/(a^2 - b^2/\bar{r}^2) \end{pmatrix} \begin{pmatrix} \Phi_1 \\ \Phi_2 \end{pmatrix} = \begin{pmatrix} Q_1 \\ Q_2 \end{pmatrix}. \quad (2.45)$$

Equation (2.45) shows, that both the self and the coupling capacitance depend on the conductor distance r . The self capacitance increases when r decreases. The self capacitance becomes $1/a$, when \bar{r} approaches infinity. The coupling capacitance decreases $\propto 1/\bar{r}$. However, if more than only two conductors are involved, the coupling behavior is different. As an example consider the interconnect geometry shown in Fig. 1.1) where multiple interconnects are located on a plane. With \bar{r} being the approximate distance between one interconnect and others, the number of neighboring interconnects at distance \bar{r} increases $\propto \bar{r}$. Coupling capacitance between interconnects with same distance is equal. The self capacitance of all interconnects is finite. Because of feature 4 in Sec. 2.5.2, the sum of all coupling capacitances is finite, too.

$$\int_R^\infty C_{i,\bar{r}} r dr < \infty$$

The integral of all coupling capacitances can only be finite, when the coupling capacitance decreases faster than $\propto 1/\bar{r}^2$ (within this simple model). This behavior is commonly known as shielding. Because of the shielding effect, usually only neighboring conductors are considered for interconnect capacitance extraction. Note, that in case of multilayer geometries the number of neighbor conductors increases even stronger than r . Hence, the shielding effect will be more pronounced.

2.5.3 Magnetic Field and Inductance

This section describes the calculation of the magnetic field and the corresponding current between conductor contacts. In order to generate a contact current, an electro magnetic force (EMF) \mathcal{U} has to be applied between conductor contacts. The following derivation leads to the skin effect, which results from the limited penetration of alternating magnetic fields into conductors.

From Eqs. (2.7) and (2.2c) the current density can be determined. Equation (2.24) then yields

$$\Delta \mathbf{A}(\mathbf{r}) - j\mu\sigma\omega \mathbf{A}(\mathbf{r}) = \mu\sigma \nabla \Phi(\mathbf{r}). \quad (2.46)$$

Note that Eq. (2.46) does not enforce current continuity $\nabla \mathbf{J} = 0$, i.e.

$$\nabla [-\sigma j\omega \mathbf{A}(\mathbf{r}, \omega) - \sigma \nabla \Phi(\mathbf{r}, \omega)] = 0. \quad (2.47)$$

One could argue that the first term $\nabla \sigma \mathbf{A}$ vanishes due to the Coulomb gauge (when $\sigma \equiv \text{const.}$). However, so far nothing has been said about the second term $\Delta \Phi$. Hence current continuity could be enforced when

$$-\sigma \Delta \Phi(\mathbf{r}) = 0 \quad (2.48)$$

is required. In the Appendix in Sec. A.3 it is shown that despite use of the Coulomb gauge $\nabla \mathbf{A} \neq 0$ when current continuity is not fulfilled, i.e. when only a part of a conductor rather than the full current return path is modeled (Eq. (A.5)). This however occurs in case of the example geometries shown in Fig. 1.1, where electric contacts are defined somewhere on conductor surfaces and hence only parts of current loops are modeled. Therefore both Eq. (2.46) and Eq. (2.47) have to be used for solving the skin effect problem.

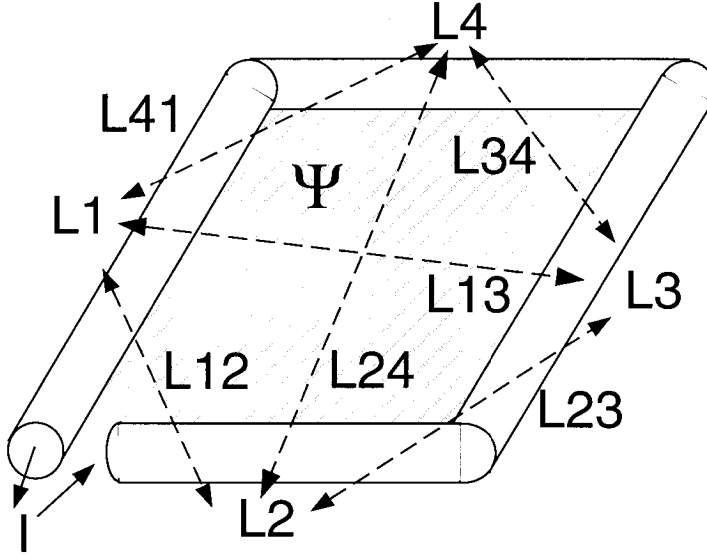


Figure 2.1: Current loop composed out of four linear conductors and surface for calculation of the magnetic flux Ψ .

Here, due to induced currents a line integral of Eq. (2.7) between contacts does not correspond to the EMF. The conservative field however can be clearly identified as $\mathbf{E}_{cons.}(\mathbf{r}) = -\nabla\Phi(\mathbf{r})$. Hence, at one contact $\Phi = 0V$ and $\Phi = U$ at the other ¹.

The inductance L is related to the magnetic field flux Ψ through a closed current loop (cf. Fig. 2.1) with

$$\Psi = LI. \quad (2.49)$$

When the current changes, due to changing flux an EMF U is induced around the current loop. According to the law of Lenz [25], this EMF is directed such that the current is minimized ($U = -Ld/dtI$). The power P put into the system is given by $P = UI$. Hence, when the current is increased over a time T from zero to the final value $I(T)$, the total

¹The skin effect problem greatly simplifies in case of two dimensional problems where a current distribution perpendicular to the cut plane is calculated. Since \mathbf{A} points in the direction in which no changes occur, it can be modeled with one variable instead of three as required for the tree dimensional problems. Moreover Eq. (2.47) is automatically fulfilled. Therefore A and Φ can be calculated separately. Due to symmetry the potential drop perpendicular to the cut plane is constant all over the cut, i.e. $\nabla\Phi = \text{const}$. Hence Eq. (2.46) has to be solved with one (complex) variable only [30].

energy W put into the system is

$$\begin{aligned} W &= \int_0^T P(t) dt \\ &= \int_0^T LI(t) \frac{d}{dt} I(t) dt \\ &= \frac{1}{2} LI^2, \end{aligned} \tag{2.50}$$

where I denotes the final total conductor current (ohmic resistance of course is neglected throughout this derivation). When the current becomes constant, the EMF vanishes and W is stored in the generated magnetic field. The magnetic field energy density w is given by [25]

$$w(\mathbf{r}) = \frac{1}{2} \mathbf{H}(\mathbf{r}) \cdot \mathbf{B}(\mathbf{r}). \tag{2.51}$$

With Eq. (A.4) the average total magnetic field energy can be calculated by integration over whole space.

$$W = \frac{1}{2} \Re \left[\int_V \mathbf{H}^*(\mathbf{r}) \cdot \mathbf{B}(\mathbf{r}) d^3r \right] \tag{2.52a}$$

$$= \frac{1}{2} \Re \left[\int_V \mathbf{H}^*(\mathbf{r}) \cdot \nabla \times \mathbf{A}(\mathbf{r}) d^3r \right] \tag{2.52b}$$

$$= \frac{1}{2} \Re \left[\int_V \nabla(\mathbf{H}^*(\mathbf{r}) \times \mathbf{A}(\mathbf{r})) + \mathbf{A}(\mathbf{r})(\nabla \times \mathbf{H}^*(\mathbf{r})) d^3r \right] \tag{2.52c}$$

$$= \frac{1}{2} \Re \left[\int_\Gamma \mathbf{H}^*(\mathbf{r}) \cdot \mathbf{A}(\mathbf{r}) d^2r \right] + \frac{1}{2} \Re \left[\int_V \mathbf{A}(\mathbf{r}) \cdot \mathbf{J}^*(\mathbf{r}) d^3r \right] \tag{2.52d}$$

In Eq. (2.52b) $\mathbf{B}(\mathbf{r})$ was replaced by $\nabla \times \mathbf{A}(\mathbf{r})$. In Eq. (2.52c) the vector identity Eq. (A.1) was used. In Eq. (2.52d) Eq. (2.1d) was used in order to replace the magnetic field $\mathbf{H}(\mathbf{r})$ by the current density $\mathbf{J}(\mathbf{r})$. Equation (2.52d) is composed out of two terms, where the first term is a surface integral only. When the current distribution is only local, it can be shown that this term vanishes [25] when the surface approaches infinity. Therefore only the second term remains, which is in fact an integral only within the regions carrying non zero current, i.e. inside the conducting regions.

With Eq. (2.28), Eq. (2.52d) can be expressed as a double integral.

$$\begin{aligned} W &= \frac{1}{2} \Re \left(\int_V \mathbf{A}(\mathbf{r}) \cdot \mathbf{J}^*(\mathbf{r}) d^3r \right) \\ &= \frac{1}{2} \Re \left(\frac{\mu}{8\pi} \int_V \int_V \frac{\mathbf{J}(\mathbf{r}) \mathbf{J}^*(\mathbf{r}')}{|\mathbf{r} - \mathbf{r}'|} d^3r d^3r' \right) \end{aligned} \quad (2.53)$$

Determining the inductance from the magnetic field flux through a closed current loop poses some difficulties. In order to carry out the necessary numerical integration one has to define an integration surface which is somehow limited by the current distribution. Another problem arises from the definition of the outer boundary of the integration surface. In case of one dimensional current distributions it is straight forward. However in the more realistic case of distributed currents its definition is not clear. Due to these problems the second formulation, i.e. inductance extraction from the magnetic field energy is often preferred. The integration volume is limited to the conductors and hence clearly defined. Another possibility for inductance extraction is the computation of the complex impedance, when a circuit is driven with an alternating current I . L can then be computed from the complex part of the impedance.

$$\mathcal{U} = [R(\omega) + j\omega L(\omega)] I, \quad (2.54)$$

where R denotes the ohmic resistance. Note the dependence of R and L on the frequency.

Figure 2.1 shows a decomposition of the loop conductor into four parts. Inductance values of the conductor parts are commonly known as *partial* inductances [31].

2.5.4 Inductance Matrix

The inductive behavior of a multi conductor system is described by the inductance matrix $\underline{\mathbf{L}}$, with

$$\mathcal{U} = (\underline{\mathbf{R}}(\omega) + j\omega \underline{\mathbf{L}}(\omega)) \mathbf{I}, \quad (2.55)$$

where \mathcal{U} denotes the vector of EMF's between conductor contacts, R is the resistance matrix and \mathbf{I} denotes the vector of currents through conductors.

Inductance matrix entries L_{ij} correspond to the induced voltage between contacts of conductor i , when the current in conductor j changes with rate 1A/s. Entries in an inductance matrix L_{ij} typically describe the induced voltage in current loop i due to a changing current in current loop j . Inductance matrices however can also be used to describe the induced voltage across a conductor part due to a changing current in another conductor part. The total inductance of the current loop in Fig. 2.1 is given by

$$L = \sum_i L_i + \sum_{i \neq j} L_{ij}, \quad (2.56)$$

where L_i denotes a diagonal entry in the inductance matrix and the L_{ij} denote offdiagonal entries.

So far only treatment of loop conductors and conductors with two contacts has been described. Conductors with more than two contacts, e.g. a T-shaped conductor with three contacts, can also be described with an inductance matrix. A conductor with $N + 1$ contacts can be considered an N-port [32]. Each port consists of two contacts. A useful choice of contact pairs is to define one conductor contact as base contact and use this base contact in every port. Then ports at the same conductor only differ in the second contact². Once this port behavior is determined, ports can be redefined and transformation exist for calculation of the new port behavior. According to Eq. (2.55) L_{ij} corresponds to the induced voltage across port i due to a changing current in port j .

Computation of an inductance matrix is similar to the computation of a capacitance matrix (c.f. Sec. 2.5.2). However, the size of an inductance matrix is given by the number of ports N_P rather than by the number of conductors N_C . Hence, N_P linear independent vectors of port currents are required for calculation of all entries in \underline{L} , which can then be calculated with Eq. (2.55). Entries in L can also be computed by evaluation of the magnetic field energy using an approach very similar to the approach for computation of entries in the capacitance matrix. When choosing port current vectors with $I_{ij} = 1\text{A}$, when $i = j$ and $I_{ij} = 0\text{A}$, when $i \neq j$ where I_{ij} denotes the j -th column of the i -th vector of port currents,

²Conductors with only two contacts are “1-ports”.

then similar to Eq. (2.36), Eq. (2.53) and Eq. (2.37)

$$\begin{aligned}
 W_{ij} &= \Re \left(\frac{1}{2} \mathbf{I}_i^T \underline{\mathbf{L}} \mathbf{I}_j \right) \\
 &= \Re \left(\frac{1}{2} \int_V \mathbf{A}_i(\mathbf{r}) \cdot \mathbf{J}^*(\mathbf{r}) d^3r \right) \\
 &= \Re \left(\frac{1}{2} \frac{\mu}{4\pi} \int_V \int_V \frac{\mathbf{J}_i^*(\mathbf{r}) \cdot \mathbf{J}_j(\mathbf{r}')}{|\mathbf{r} - \mathbf{r}'|} d^3r' d^3r \right). \quad (2.57)
 \end{aligned}$$

In Eq. (2.57) $\mathbf{J}_i(\mathbf{r})$ denotes the current distribution which belongs to the vector of port currents I_i . Because of the choice of port currents in Eq. (2.57) $W_{ij} = I_{ii}L_{ij}I_{jj} = L_{ij}$.

Entries in the inductance matrix L have the following features:

1. Since Eq. (2.57) is symmetric in \mathbf{r} and \mathbf{r}' , also L is symmetric, i.e. $L_{ij} = L_{ji}$.
2. Since the magnetic field energy is positive for any current distribution ($W = 1/2 \mathbf{I}^T \underline{\mathbf{L}} \mathbf{I} > 0 \forall \mathbf{I} \neq 0$), L is positive definite .
3. Diagonal entries $L_i > 0 \forall i$, because of feature (2) and only the i -th component of the vector of port currents $\neq 0$.
4. There is no shielding (when $\mu = \text{const.}$). Hence, there is no upper limit for the sum of coupling inductances .
5. Due to Eq. (2.57) there is no inductive coupling between conductors when current directions are orthogonal .
6. Inductive coupling is negative when current directions are antiparallel .

The range of an inductive interaction depends on how a circuit is composed. Estimating the coupling inductance between small parallel conductor parts can be done with Eq. (2.57) where it turns out that $L_{12} \propto 1/r$ with L_{12} the coupling inductance and r the approximate distance. The inductive coupling between two distant conductor loops is different. It can be analyzed when a loop is split into four straight conductors as shown in Fig. 2.1. Inductive coupling of one distant straight conductor with this loop can now be split into couplings with the parallel and with the anti parallel conductor. As parallel and anti parallel contributions

almost cancel each other out, only a higher order coupling $\propto 1/r^2$ is left. The inductive coupling between two distant conductor loops correspondingly decreases $\propto 1/r^3$, where r again is the distance between the two conductor loops.

There is one difficulty associated with the use of partial inductances, which is only rarely mentioned. When the total loop inductance is small due to a small enclosed flux surface but the sum of absolute values of partial inductance is large, then numerical errors of calculated partial inductances can add up to a large relative error of the total loop inductance.

2.5.5 Electric Current and Resistance

This section deals with current distributions inside conductors and the description of ohmic losses by **resistance** values. The calculation of current distributions already has been explained in Sec. 2.5.3. Resistance values can be extracted from the ohmic power loss

$$P = \Re \left\{ \int_V \mathbf{J}^*(\mathbf{r}) \cdot \mathbf{E}(\mathbf{r}) d^3r \right\} \quad (2.58)$$

and from the complex relation between applied EMF and total conductor current Eq. (2.54), where the total conductor current is a flux integral $\Re \left\{ \int_{\kappa} \mathbf{J}(\mathbf{r}) \cdot \mathbf{n}(\mathbf{r}) d^2r \right\}$ with κ any cross section inside the conductor and $\mathbf{n}(\mathbf{r})$ a normal on κ .

2.5.6 Resistance Matrix

The resistance matrix \mathbf{R} has already been mentioned in Eq. (2.55). Consequently the same set of current distributions is required for the computation of a resistance matrix as is required for the computation of an inductance matrix and the resistance matrix is of same size as the inductance matrix. Inside the conductor current continuity $\nabla \mathbf{J}(\mathbf{r}) = 0$ is fulfilled. With similar arguments as in Sec. 2.5.2 it can be shown that entries in the resistance matrix are given by

$$R_{ij} = \Re \left(\int_V \mathbf{E}_i(\mathbf{r}) \cdot \mathbf{J}_j(\mathbf{r}) d^3r \right), \quad (2.59)$$

where the electric field $\mathbf{E}_i(\mathbf{r})$ and the current density $\mathbf{J}_j(\mathbf{r})$ correspond to EMFs of port current vectors \mathbf{I}_i and \mathbf{I}_j respectively when port current vectors are defined as in Sec. 2.5.4.

It is now shown that the inverse of the resistance matrix, the admittance matrix $\underline{\mathbf{Y}}$, has exactly the same properties as the capacitance matrix Eq. (2.35).

$$\underline{\mathbf{Y}}\mathbf{U} = \mathbf{I} \quad (2.60)$$

Let us assume a system of N conductors surrounded by an insulator with high dielectric permittivity $\varepsilon \rightarrow \infty$. During capacitance analysis the displacement current $\mathbf{D}(\mathbf{r})$ cannot penetrate into this region and is therefore limited. This corresponds to the situation described in feature (4) of the properties of the capacitance matrix in Sec. 2.5.2, where the capacitance matrix is singular and therefore one column can be determined from the others (because $\nabla\mathbf{D}(\mathbf{r}) = 0$). Conductor charges are determined from the flux of the displacement current $\mathbf{D}(\mathbf{r})$ through surfaces around the conductors (Eq. (2.31)).

It is now shown that this is equivalent to determining the total current through $N - 1$ ports. The corresponding situation for the resistance extraction is a conductor with N contacts, i.e. $N - 1$ ports. As in case of capacitance extraction, here total port currents for given EMFs are determined from $N - 1$ flux integrals of a divergence free vector field $\mathbf{J}(\mathbf{r})$ through surfaces in front of contacts. According to features of the capacitance matrix in Sec. 2.5.2 features of the resistance matrix are:

1. In Eq. (2.59) it is shown that $Y_{ij} = Y_{ji}$.
2. $Y_{ii} > 0 \forall i$. When the EMF at port i is positive the resulting port current is positive.
3. $Y_{ij} < 0 \forall j \neq i$. When other EMF's are zero, this results in negative port currents.
4. $\sum_j Y_{ij} > 0$. The sum of admittance matrix entries equals the total current through the contact which is common to all ports.
5. $\underline{\mathbf{Y}}$ is positive definite, because the ohmic power loss $\mathbf{U}^T \underline{\mathbf{Y}} \mathbf{U} > 0 \forall \mathbf{U} \neq 0$.

As the admittance matrix $\underline{\mathbf{Y}}$ is an M-matrix, as expected all entries of the inverse $\underline{\mathbf{R}}$ are positive or zero.

2.6 Static Approximation

When applying the static approximation all time dependence of the Maxwell equations Eqs. (2.1a-2.1d) is neglected. In the frequency domain this corresponds to $\omega = 0$. Furthermore, since there is no phase delay, all field variables become real. Note that electric and magnetic fields are completely decoupled. The electric field can be characterized with capacitance values as in the quasistatic approximation.

Current density computation is done with Eq. (2.7) and Eq. (2.2c), which here become

$$\mathbf{J}(\mathbf{r}) = -\sigma \nabla \Phi. \quad (2.61)$$

Hence Eq. (2.46) in the static case becomes

$$\Delta \mathbf{A}(\mathbf{r}) = \mu \sigma \nabla \Phi(\mathbf{r}). \quad (2.62)$$

Current continuity Eq. (2.47) is fulfilled when $\nabla \sigma \nabla \Phi(\mathbf{r}) = 0$ inside conductors. Obviously, within the static approximation the current density distribution is independent of the magnetic field. Since the applied EMF corresponds to the contact values of the electric scalar potential, the current density can be determined from a solution of

$$\nabla \sigma \nabla \Phi(\mathbf{r}) = 0 \quad (2.63)$$

inside the conductors with appropriate Dirichlet boundary conditions at the contacts. In a second step the corresponding magnetic field can be calculated by solving Eq. (2.62). As the three components of the magnetic vector potential are not coupled, Eq. (2.62) can in fact be solved component wise, i.e. computation of the magnetic vector potential involves three independent solutions of a inhomogeneous Poisson equation.

Since there is no phase delay due to alternating current, for inductance extraction only the magnetic flux formalism or the magnetic field energy formalism can be used for inductance extraction (Sec. 2.5.3). Resistance values can be calculated both from the applied EMF and resulting total current or from the ohmic power loss as described in Sec. 2.5.5.

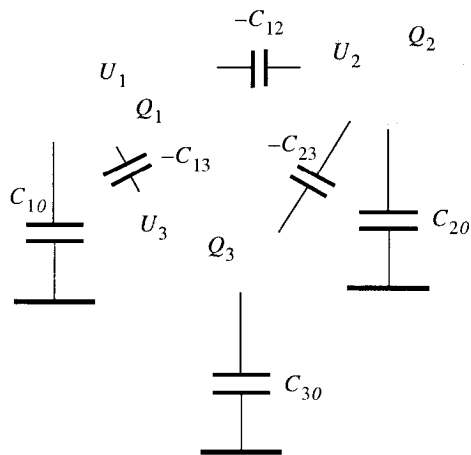


Figure 2.2: Three conductors with equivalent circuit consisting entirely of capacitors. Capacitor values are calculated from entries in the capacitance matrix C_{ij} . Here, $C_{i0} = \sum_j C_{ij}$.

2.7 Other Potential Formulations

Solution of the skin effect problem with Eq. (2.46) and Eq. (2.47) has one major disadvantage. Inside conductors fields are calculated from the magnetic vector potential \mathbf{A} and from the electric scalar potential Φ . Outside conductors where $\sigma = 0$ the full magnetic vector potential \mathbf{A} has to be computed, which can in fact be too costly for use in Finite Element Methods as explained in the following chapter. Since only a small part of a simulation domain is usually “filled” with conducting material a vector potential should be used only here in order to save variables. We use the current vector potential \mathbf{T} [33] with

$$\mathbf{J}(\mathbf{r}) = \nabla \times \mathbf{T}. \quad (2.64)$$

Note that this definition automatically fulfills current continuity $\nabla \cdot \mathbf{J} = 0$. Definition of a current vector potential is only required inside conductors. Equation (2.21) then leads to the magnetic field, which hence is defined up to the gradient of a scalar function

$$\mathbf{H}(\mathbf{r}) = \mathbf{T}(\mathbf{r}) - \nabla \phi(\mathbf{r}). \quad (2.65)$$

Outside conductors $\mathbf{H}(\mathbf{r})$ can be deduced from a magnetic scalar potential $\phi(\mathbf{r})$ alone. With Coulomb Gauge for the electric vector potential $\nabla \cdot \mathbf{T}(\mathbf{r}) = 0$ the skin effect differential equation Eq. (2.46) here becomes

$$\frac{1}{\sigma} \Delta \mathbf{T}(\mathbf{r}) - j\omega\mu \mathbf{T}(\mathbf{r}) = j\omega\mu \nabla \phi(\mathbf{r}). \quad (2.66)$$

The Maxwell equation Eq. (2.1b) is not fulfilled automatically and has to be enforced by another equation

$$\nabla (\mu \mathbf{T}(\mathbf{r}) - \mu \Delta \phi(\mathbf{r})) = 0. \quad (2.67)$$

A scalar magnetic potential works well in simply connected domains. However, when a loop integral $\oint \mathbf{H}(\mathbf{r}) d\mathbf{r}$ is evaluated around a conductor, due to the law of Biot Savart, the result is the total current through this loop. In order to obtain this result from a simulation model, so called “cut planes” have to be introduced in holes in conductors. At the cut the scalar magnetic potential has to jump according to the total current inside the conductor. Without a jump, no current flow can be modeled. Cut planes can be avoided by use of layers with defined current vector potential. When current vector potentials are used outside conductors, a high electrical resistivity has to be assumed [34].

Obviously modeling partial inductances is impossible using this formulation, because cut planes cannot be defined. However, various formulations exist where both current vector potential and magnetic vector potential exist outside conductors. These allow modeling of partial inductances, the advantage of reducing the number of variables, however, is lost.

Cut planes have to be introduced only when differential equations are solved. The corresponding integral equation to Eq. (2.28) also exists. Here, during solution field variables are required only inside conductors. Hence, the definition of cut planes is avoided. Here, however, still four coupled equations have to be solved, as in case of the magnetic vector potential and electric scalar potential formulation. Since the magnetic vector potential and the electric scalar potential are directly related to the total conductor current and the contact potential, this formulation is more attractive. The author does not know any computer program where Eq. (2.66) is solved with an integral equation approach. An integral equation approach with magnetic vector potential and electric scalar potential has in fact been prepared several times.

2.8 Analytical Solutions

Analytical solutions are discussed here for two purposes. First, in order to show their limits and to motivate the need for numerical solution approaches. Second, in order to show to what extent analytical solutions can be incorporated into a numerical solution approach.

2.8.1 Impedance of a Rectangular Conductor

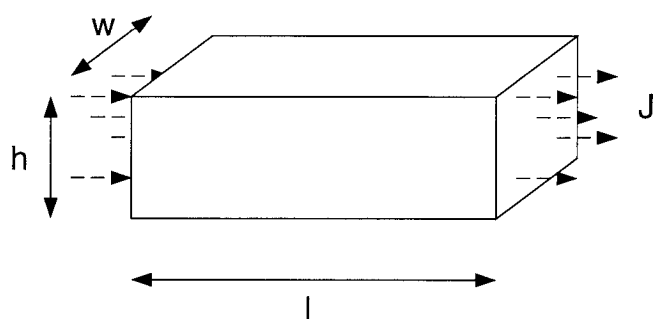


Figure 2.3: Rectangular conductor with length l , width w , height h and current density J indicated. The current density is constant inside the brick.

For the simple conductor geometry shown in Fig. 2.3 the relation between EMF U and total current is given by a one dimensional impedance matrix Eq. (2.55)

$$Z = R + j\omega L. \quad (2.68)$$

The ohmic resistance R of this rectangular conductor with cross section wh and length l with constant current density J can be calculated from the ohmic power loss P Eq. (2.58). The electric field E can be calculated from the difference between contact potentials U and the conductor length l . With Eq. (2.2c) this integration becomes

$$P = \sigma \frac{U^2}{l^2} whl. \quad (2.69)$$

Since $P = RI^2$ and the total conductor current is given by the current density times the cross section of the conductor $I = Jwh$ this reduces to

$$R = \frac{l}{\sigma wh}. \quad (2.70)$$

The inductance L can be calculated from the magnetic field energy with Eq. (2.53) and Eq. (2.50). Since the current density is constant, in this case $J^2 = I^2/(w^2h^2)$ with I the total current. Hence,

$$W = \frac{\mu}{8\pi} \int_0^w \int_0^h \int_0^l \int_0^w \int_0^h \int_0^l \frac{J^2}{\sqrt{(x-x')^2 + (y-y')^2 + (z-z')^2}} dz' dy' dx' dz dy dx. \quad (2.71)$$

Table 2.1: *Electrical conductivities for different materials [1].*

Silver	$6.17 \cdot 10^7 \text{ S/m}$
Copper	$5.80 \cdot 10^7 \text{ S/m}$
Aluminum	$3.72 \cdot 10^7 \text{ S/m}$
Solder	$0.71 \cdot 10^7 \text{ S/m}$

The singularity vanishes, as can be seen from a similar integral during evaluation of the approximate self capacitance of a disc (Eq. (2.40)). Integration of Eq. (2.71) can be carried out analytically [35]. The resulting expression is given in Sec. B.1 in the Appendix. Unfortunately, it is rather complicated and therefore cannot be used in computer programs where excessive evaluation is required. More suitable approximate and flexible formulas exist [36] where the computational effort can be adjusted such that results lie within a required error range. Other approximate formulas for many kinds of geometries are given in a quite famous book by Grover from 1946 [37]. Other approximate formulas with emphasis in transmission line analysis are given in [38], where also capacitances for two dimensional conductor geometries can be found.

2.8.2 Skin Effect

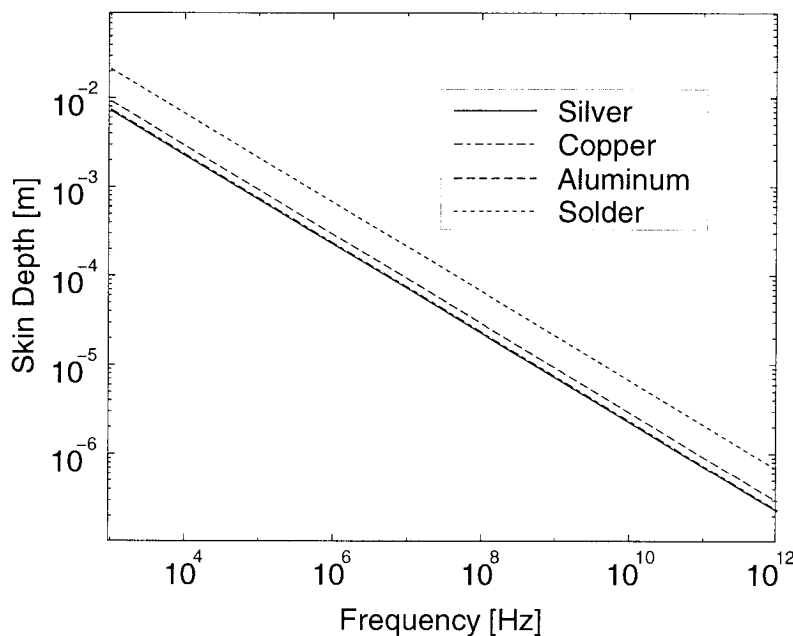


Figure 2.4: *Skin depth for different materials and frequencies. Conductivity values are shown in Tab. 2.1*

With non zero frequency, it can be seen from Eq. (2.4a) that electric and magnetic fields are coupled. In conducting regions, Eq. (2.2c) relates the electric field to the current density.

After combination of Eqs. (2.4a) and (2.2c), neglect of free charges and assumption of constant electric conductivity, one obtains

$$\Delta \mathbf{E} - j\omega\mu\sigma\mathbf{E} = 0. \quad (2.72)$$

For derivation of the skin depth, i.e. the penetration depth of an electric field into a conductor, one assumes an infinitely extended conductor with surface at $x = 0$. Coordinates with $x < 0$ are not part of the conductor and coordinates with $x > 0$ lie within the conducting material [39]. This is a one-dimensional problem. From here, only variations in x-direction are considered. The differential equation Eq. (2.72) can be solved with an exponential function ansatz.

$$E_i = ae^{-\kappa x} + be^{\kappa x}, \quad (2.73)$$

where the index i stands either for y or z . In Eq. (2.73) the coefficients a and b have to be determined from boundary conditions. Obviously the electric field has to decrease when x is becoming large. Therefore in this case $b = 0$. After insertion, Eq. (2.72) yields a parameter $\kappa = \sqrt{j\omega\mu\sigma}$. The total r.m.s. value of the current flowing on the conductor surface I leads to the definition of the skin depth δ [39], $I\sqrt{2} = J_s\delta$, where J_s is the current density at $x = 0$. Hence

$$\delta = \sqrt{\frac{2}{\mu\sigma\omega}}. \quad (2.74)$$

The skin depth is shown for common conductor materials at different frequencies in Fig. 2.8.2. Electric conductivities for the respective materials are given in Tab. 2.1.

Further analytical solutions for two dimensional geometries are given in [40], [39]. These usually consist of series expansions where coefficients are matched according to boundary conditions. Note, that there is no analytical solution for the skin effect problem in general three dimensional conductor geometries.

When the skin depth is large compared to the diameter of a conductor, it follows that the current density is not influenced by the changing magnetic field. Hence in this situation the static approximation of the

Geometry	f_r	Diameter	δ	Approximation
Interconnect	10^9Hz	$\approx 10^{-6}\text{m}$	$2.7 \cdot 10^{-6}\text{m}$	static
DIP Package	10^8Hz	$\approx 10^{-3}\text{m}$	$8.5 \cdot 10^{-6}\text{m}$	quasistatic
IGBT Busbar	10^6Hz	$\approx 10^{-2}\text{m}$	$8.5 \cdot 10^{-5}\text{m}$	quasistatic

Table 2.2: Highest relevant frequency f_r during operation of conductor geometries shown in Fig. 1.1, approximate diameter of conductors, associated skin depth δ (Eq. (2.74)) and recommended approximation of the Maxwell equations.

Maxwell equations can be applied. With Tab. 2.2 one can estimate the skin depth associated with operation of conductor geometries shown in Fig. 1.1. The static approximation is recommended when the skin depth is large compared to the approximate conductor diameter. Otherwise the quasistatic approximation is recommended. Despite of this rather rigorous estimate one has to keep in mind what input impedances of the connected circuit are like. Due to small changes sometimes the static approximation can be used despite the fact that the skin depth is much smaller than the approximate conductor diameter.

2.9 Generation of Equivalent Circuits

This section describes how equivalent circuits are generated from \mathbf{R} , \mathbf{L} and \mathbf{C} matrices. First, a circuit with capacitances only is built. Inductors and resistors are added in a subsequent step.

2.9.1 Including Capacitances

In an equivalent circuit of capacitors every conductor is represented as a single node. The electric potential on this node corresponds to the electric potential of the conductor used for capacitance analysis. Since there is a capacitive coupling between all conductors, capacitors are placed between all possible pairs of nodes. The capacitances of these circuit capacitors \tilde{C}_{ij} can be calculated from the capacitance matrix by considering the accumulated conductor charges for given electric potentials

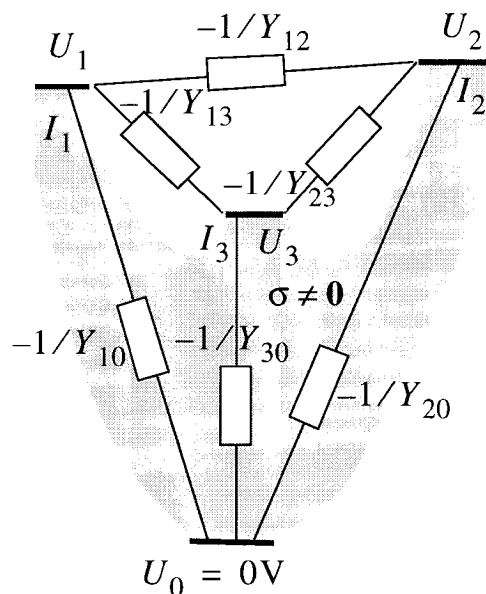


Figure 2.5: Conductor with four contacts and equivalent circuit of resistors. The resistive behavior is determined by a 3×3 admittance matrix $\underline{\mathbf{Y}}$ Eq. (2.60). Resistance values are calculated from entries in the admittance matrix Y_{ij} . Here, $Y_{i0} = \sum_j Y_{ij}$.

[1].

$$Q_i = \sum_{j \neq i} \tilde{C}_{ij} (\Phi_i - \Phi_j), \quad (2.75)$$

where the Φ_i are the conductor potentials. With Eq. (2.35) and by comparison of coefficients one obtains

$$\tilde{C}_{ij} = \begin{cases} -C_{ij} & \text{when } j \neq i \\ \sum_j C_{ij} & \text{when } j = i, \end{cases} \quad (2.76)$$

with C_{ij} the entries in the capacitance matrix $\underline{\mathbf{C}}$ in Eq. (2.35) and $\tilde{C}_{ii} \equiv C_{i0}$ the capacitive coupling with ground (Fig. 2.2).

2.9.2 Including Resistances

Each port for resistance analysis is represented by two nodes in the equivalent circuit. Since the capacitance matrix Eq. (2.35) and admittance matrix Eq. (2.60) have same properties, the equivalent circuit is built in the same way. Figure 2.5 shows a conductor with four contacts where ports 1,2,3 are defined between contact pairs (0,1), (0,2) and (0,3) respectively. As in Sec. 2.9.1 matrix entries are chosen for the respective port conductances. Since conductances cannot be introduced in circuit simulators directly, resistance values are calculated from the respective conductances $R = 1/Y$. Self conductances, which here result in resistors

parallel to the port are calculated in the same way as self capacitances, i.e. $Y_{i0} = \sum_j Y_{ij}$, the sum of all row entries.

2.9.3 Merging RLC

This is the most easy part. Self inductances associated with ports are simply put in series with respective port resistances. Inductive couplings are inserted in the circuit model directly.

Coupling of capacitance circuits with resistance and inductance circuits is somewhat arbitrary. The only information on topology available is which ports belong to which conductors. Where to insert the capacitance is hence unclear. Therefore capacitance nodes which represent conductors are electrically connected with arbitrary port contact. The error introduced and quality of results is discussed below in Sec. 2.9.5

2.9.4 Example

Figure 2.9.4 shows a grid model of two conductors with names of contacts and respective current directions indicated. One conductor – a via structure – has three contacts, the other has two contacts. Current direction and contact names are also indicated. The capacitive behavior is therefore described with a 2×2 capacitance matrix. Three ports are required to describe the resistive and inductive behavior. Hence \mathbf{R} and \mathbf{L} are 3×3 matrices. The bottom of the figure shows the generated equivalent circuit where contacts are represented by nodes and contact names from above are indicated, too.

2.9.5 Validity

This section describes the validity of the generated circuit model. Since capacitors are inserted at arbitrary nodes at conductors, circuit models are not symmetric whereas original conductors are. However, circuit models are accurate when the additional impedance associated with capacitors is large compared to resistance and inductance. A large impedance acts like an open contact and therefore does not influence the circuit behavior. In this case a circuit model like the coarse one

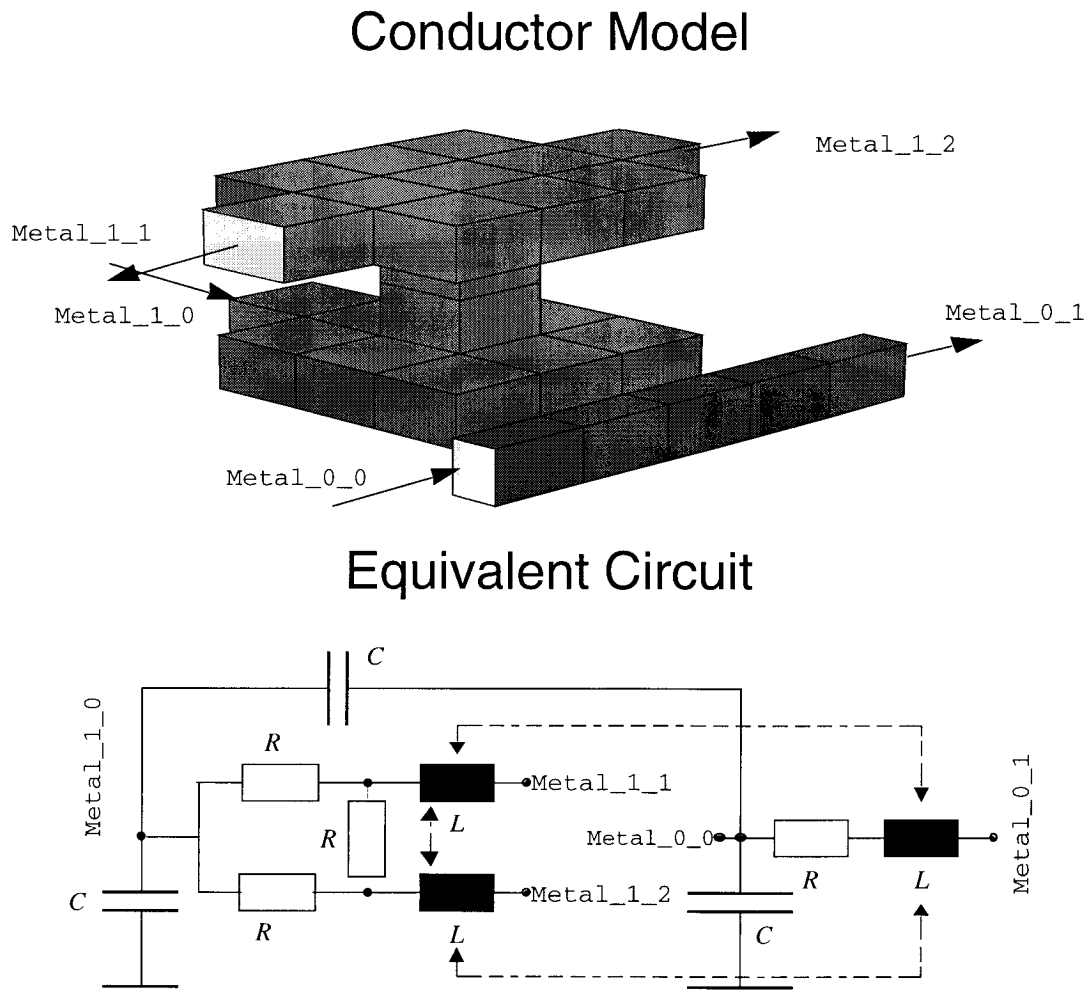


Figure 2.6: *Top: Grid model of a via structure with three contacts and additional conductor with two contacts. Bottom: Equivalent circuit with resistors, inductors and capacitors.*

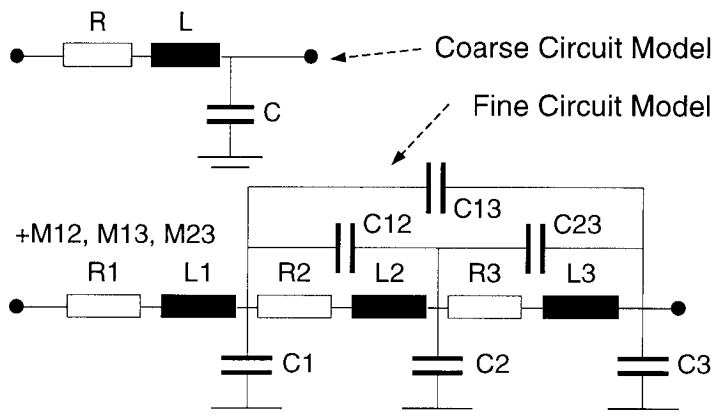


Figure 2.7: *Coarse and fine circuit model of the same conductor.*

in Fig. 2.7 is a suitable model. It is shown in [27], that circuit models consisting only of resistors and capacitors are generally stable, i.e. they mostly reflect the actual contact behavior. Hence circuit models are quite accurate when the inductance is small compared to the ohmic resistance. When all impedances, impedance from capacitor, from inductor and from resistor are in the same range of magnitude, things get more involved and in this situation a simple circuit model like the coarse one in Fig. 2.7 does not yield correct results. A standard approach is to refine the conductor, simulate **RLC** matrices of the resulting set of conductors and reconnect circuit models on circuit level. A typical result of such a procedure – a fine circuit model – is shown in Fig. 2.7. Note, that one cannot simply divide RLC by the number of circuit partitions and use these as RLC of the circuit partitions since those may differ from the average. In [27] it is stated furthermore, that in this case circuit models converge slowly, i.e. one has to divide a circuit many times in order to obtain convergence. A major disadvantage of this method is the increased demand for costly RLC simulations and during circuit simulation the high number of lumped elements with capacitive and inductive coupling. Only recently another approach has been introduced, where basically the concept of resistors, inductors and capacitors is given up and only the frequency dependent electrical contact behavior is simulated. Since electric and magnetic fields are not simulated separately it is called the electro magnetoquasistatic approximations. Here, current distributions are not only determined by the contact EMF, but also by the emerging surface charges [41].

The relative influence of inductance and capacitance differs for the examples shown in Fig. 1.1. In case of the interconnect example, inductances just become important with increasing clock rates. Hence, the influence of inductances is just as important as the influence of capacitances. Therefore a fine resolution of circuit models is required. Pins of the DIP package are long, narrow and quite distant. Hence, inductance dominates capacitance and coarse models will yield quite accurate results. The capacitance of an IGBT module can be estimated from a plate capacitor $C = \epsilon A/d$ where A is the surface size of metal plates and d their distance. In Fig. 1.1 $A \approx 20 \cdot 10\text{cm}^2$ and $d \approx 1\text{cm}$. This yields an approximate capacitance $C \approx 20\text{pF}$ and results in an impedance at $f = 10^6\text{Hz}$ (Tab. 2.2) of $|1/j\omega C| \approx 8 \cdot 10^3\Omega$ which is much larger than the impedance associated with typical inductances of 100nH . The impedance associated with such inductance values is $|j\omega L| \approx 0.6\Omega$.

2.10 Conclusions

A complete overview has been given on Maxwell equations in linear media, use of potentials, quasistatic and static approximation, translation of results into lumped element models for subsequent circuit simulation, validity of these models and measures for improvement. Features of inductance, resistance and capacitance matrices and concepts of partial inductances and partial capacitances have been reviewed. Since some numerical routines are based on a split geometry, these features are important for possible simplifications. Furthermore partial entities can be used for splitting conductor geometries which are too large and complicated to be simulated in one step. Finally, the need for numerical analysis is shown by discussion of analytical solutions to more simple problems.

Seite Leer /
Blank leaf

Application of the Finite Element Method

The following chapter reviews the use of the **F**inite **E**lement **M**ethod (FEM) for inductance extraction. The FEM is a powerful and versatile numerical method for the solution of partial differential equations. A global overview can be found in [42]. Application of FEM to electro magnetism is discussed in a more recent book [43]. A complete synopsis of possible boundary conditions for different potential formulations is given in [33].

During this work, the capabilities of an existing FEM program SOLIDIS_{ISE} [8] have been extended towards static inductance extraction. Partial inductance values are computed from the total conductor current and the corresponding magnetic field energy.

First, the influence of different boundary conditions is discussed and simulation results for a simple geometry are given. In order to minimize the simulation error. SOLIDIS_{ISE} provides several grid refinement strategies. Their efficiency is compared. Results are used for the simulation of two bigger example geometries. Possible extensions towards inductance extraction including the skin effect are discussed, references in literature are given and conclusions are drawn.

3.1 Boundary Conditions

As discussed in Sec. 2.6 the following partial differential equations are solved by the FEM program. First, the scalar electric potential is determined inside conductors with

$$\nabla\sigma\nabla\Phi(\mathbf{r}) = 0, \quad (3.1)$$

Note that Eq. (3.1) also allows varying electrical conductivity σ , whereas Eq. (2.63) only allows constant σ inside conductors. The current density $\mathbf{J}(\mathbf{r})$ is computed from the electric scalar potential with Eq. (2.61). In subsequent steps each component of the magnetic vector potential is simulated with Eq. (2.62) which is given here, again.

$$\Delta\mathbf{A}(\mathbf{r}) = -\mu\mathbf{J}(\mathbf{r}). \quad (3.2)$$

Self- and mutual inductance value are extracted from the magnetic field energy using Eq. (2.57).

The most simple boundary conditions for the simulation of the magnetic vector potential are the homogeneous Dirichlet boundary condition with \mathbf{A} normal on the grid boundary Γ ,

$$\mathbf{A} \times \mathbf{n} = 0 \quad \text{on } \Gamma \quad (3.3)$$

and the homogeneous Neumann boundary condition with no flux of \mathbf{A} through the boundary [33]

$$\mathbf{A} \cdot \mathbf{n} = 0 \quad \text{on } \Gamma. \quad (3.4)$$

The Dirichlet boundary condition acts like a surface of an ideal conductor. When a magnetic field is generated outside the conductor, surface currents are induced such that the inner of the conductor is field free. Correspondingly the normal component of the magnetic flux density is zero on the boundary

$$\mathbf{B}(\mathbf{r}) \cdot \mathbf{n}(\mathbf{r}) = 0 \quad \text{on } \Gamma. \quad (3.5)$$

The Neumann boundary condition introduces a symmetry into the magnetic field distribution. In contrast to the Dirichlet boundary condition no surface currents exist, i.e.

$$\mathbf{H}(\mathbf{r}) \times \mathbf{n}(\mathbf{r}) = 0 \quad \text{on } \Gamma. \quad (3.6)$$

There are two possibilities to understand the influence of a grid boundary on an inductance result. First, the calculated inductance might not be correct when the fields are somehow deflected by the grid boundaries. Field deflection will be small when the distance between conductor and grid boundaries is large, such that the field is totally enclosed inside the grid boundaries. It is however unclear, how far the field stretches and how large the error might be – once fields are somehow deflected. Another possibility for estimating the influence of grid boundaries is to think in terms of Greens functions, i.e. in terms of mirror currents outside the grid boundaries. A simulated magnetic vector potential hence corresponds to the magnetic vector potential generated by all initial and mirrored current distributions. The simulated inductance, due to Eq. (2.57) therefore is the self inductance plus inductive couplings with all mirrored current distributions.

Mirrored currents – when only one boundary is present – are shown in Fig. 3.1. When multiple boundaries are present as in case of an FEM grid, mirrored currents are themselves reflected and lead to second order mirrored currents which themselves are reflected and so on. A periodic continuation of mirror currents in case of the Dirichlet boundary condition is shown in Fig. 3.2. The left shows a “primitive cell”, known from solid state physics. This primitive cell includes the source current distribution in the center rectangle and the mirrored currents, which are mirrored at the boundaries of the center rectangle. These mirrored currents including their surrounding rectangles can be interpreted as source currents with respective center rectangle of a new primitive cell. Periodic continuation of these primitive cells is shown on the right in Fig. 3.2. Note, that reflected currents do not necessarily point in the opposite direction of the source current. Hence, the inductance is not necessarily reduced by the existence of a Dirichlet boundary condition. Only in case of currents flowing perpendicular to the grid boundary, first order mirrored currents point in the opposite direction and thus lead to negative inductive coupling which reduces the simulated self inductance of the source current ¹. Note, that sometimes the influence of mirrored currents on the simulated inductance result is desired, e.g. during the

¹Current distributions perpendicular to the shown cut through boundaries are a one dimensional phenomenon. Hence, all investigations concerning current distributions perpendicular to grid boundaries directly apply to capacitance extraction, where the current distribution can be replaced by a charge distribution and the one dimensional magnetic vector potential can be replaced by the one dimensional electric potential and also a Laplace equation is solved (Eq. (2.23)) .

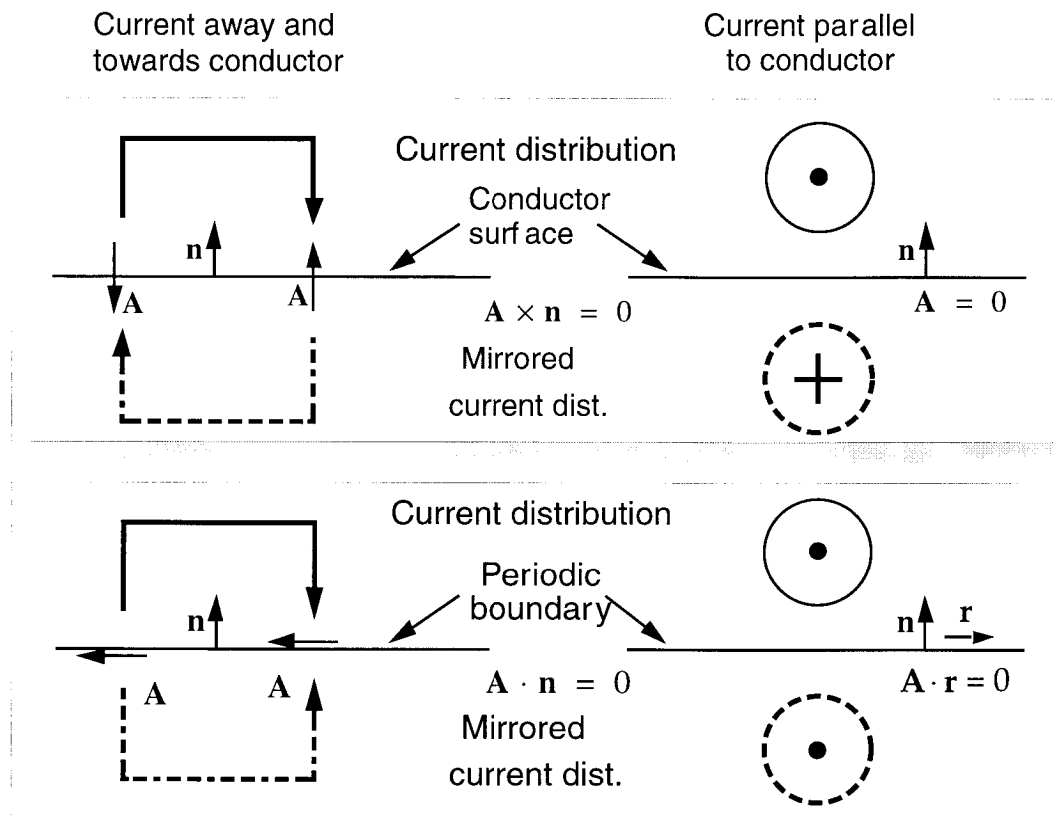


Figure 3.1: Boundary conditions for the magnetic vector potential and corresponding mirror current distributions outside the grid. Left: side view of currents. Right: current flows towards (·) or away from viewer (+). Top: Dirichlet boundary condition Eq. (3.3). Bottom: Neumann boundary condition Eq. (3.4).

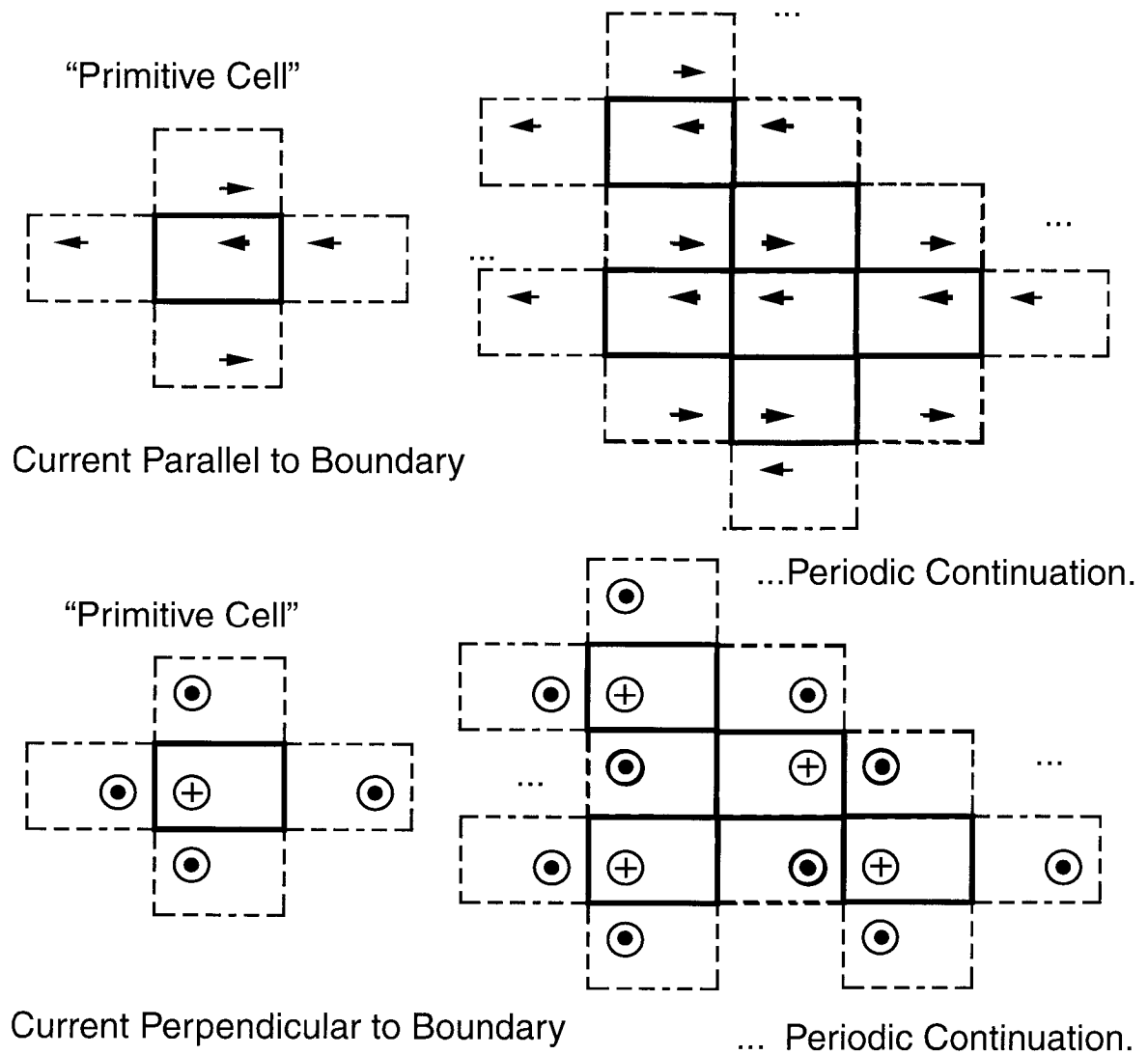


Figure 3.2: Ideally conducting boundary condition and periodic continuation of geometry. Top: current flows parallel to boundary. Bottom: current flows vertical to boundary. Left: "Primitive Cell". Right: periodic continuation.

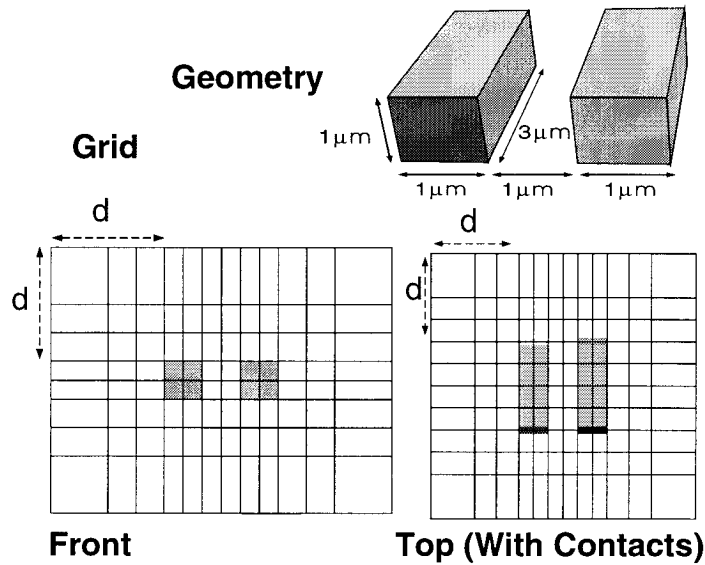


Figure 3.3: *Simple test structure. Top: Conductor geometry – two rectangular bricks with distance $1\mu\text{m}$, length $3\mu\text{m}$ and cross section $1\mu\text{m}^2$. Bottom: Cuts through grid with distance d between conductors and grid boundary.*

simulation of transmission lines or when symmetric geometries are simulated.

One possibility to minimize the influence of mirrored current distributions on inductance results is the so called “ballooning” method [44], where the FEM grid domain is extended such that simulation results do not change when the simulation domain is chosen even larger.

3.1.1 Example

A very simple test structure shown in Fig. 3.3 has been chosen in order to investigate how grid boundaries affect simulation results. The test structure is shown on top of the figure. It consists of two rectangular conductors where current flows from the front face to the opposite face. The current density inside the conductors is constant. Self- and coupling inductances of the structure can be calculated analytically with Eq. (B.2). In the bottom of Fig. 3.3 two cuts through the FEM grid are shown. The distance d between conductors and grid boundary is indicated also.

Several simulations with different values of d , Neumann and Dirichlet boundary conditions have been carried out. How accuracy of FEM simulations is assured is explained in the following section (Sec. 3.2). Results of self and coupling inductance simulations and theoretical results are shown in Fig. 3.4.

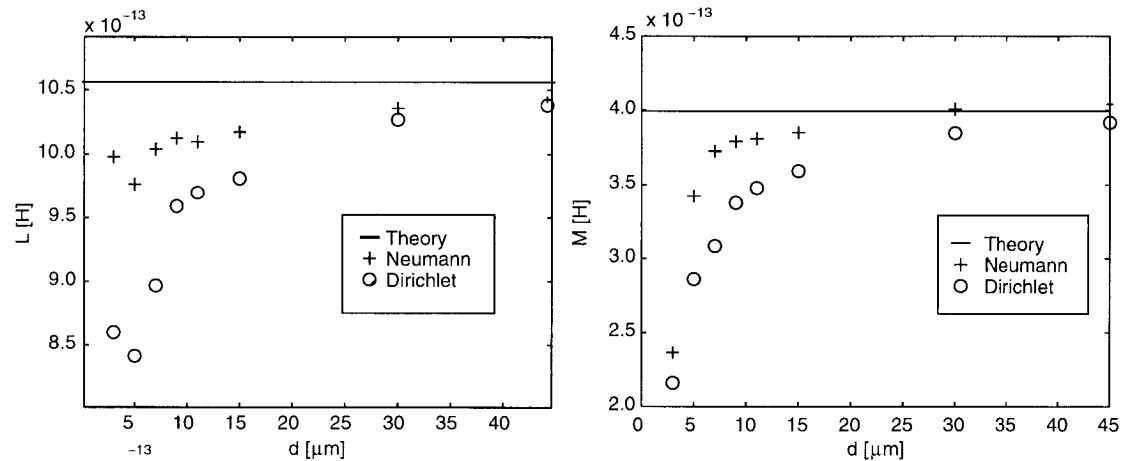


Figure 3.4: *Dependence of inductance values on distance d (c.f. Fig. 3.3) between conductors and grid boundary. Left: Self inductance L . Right: Inductive coupling M .*

Both boundary conditions lead to simulated inductance values below theoretical results, where the influence of the Neumann boundary condition is smaller than the influence of the Dirichlet boundary. Since inductance corresponds to magnetic field energy, it seems that the conductors are “bound” within the periodic continuation of conductors shown in Fig. 3.2 where the difference between the simulated and the theoretical inductance value corresponds to the energy which is necessary to remove a conductor from the periodic continuation.

Convergence of simulation results with respect to the distance from the boundary d is slow. In order to obtain simulation results with 5% accuracy, a minimum distance between conductors and grid boundary of $d > 30\mu\text{m}$ is required. In order to obtain results with less than 1% relative error, a distance $d > 45\mu\text{m}$ is required which leads to a rather large grid compared to the dimensions of the whole geometry shown in Fig. 3.3.

The relative error of the coupling inductance is always larger than the relative error of the self inductance. This is reasonable, because for larger distances between conductors the influence of mirrored current distributions is increased.

Note, that when using “ballooning”, only a differential error criterion is available. A user of the method has to enlarge the simulation domain such that simulated inductance values change less than a predefined

ratio. Therefore usually at least two simulations are necessary in order to confirm that a required (relative) accuracy is reached.

3.2 Grid Refinement

SOLIDIS_{ISE} uses nodal elements with eight corners and bilinear expansion functions. Hence each field component f is given by a polynomial

$$f(x, y, z) = a + bx + cy + dz + exy + fyz + gzx + hxyz \quad (3.7)$$

with constants a, b, c, d, e, f, g, h . These constants are determined by the nodal values on the corners of each element and usually differ from one grid element to another. Note, that the scalar electric potential Φ requires a set of coefficients only inside the conductor and each component of the magnetic vector potential requires a set of coefficients on the whole grid.

The accuracy of a numerical solution is improved by increasing the number of elements. This grid refinement technique is commonly known as “h-refinement”. Other grid refinement techniques have not been investigated during this work. These other refinement techniques include “p-refinement”, where the degree of the polynomial in Eq. (3.7) is increased and the number of grid elements stays constant, and the combination “hp-refinement”, where both techniques are applied at the same time. All refinement techniques lead to a higher number of unknowns in the resulting linear equation. In order to minimize the number of unknowns, grid refinement should only be applied where necessary. Construction of an optimal grid still is a difficult task where a variety of strategies are used [45].

A very efficient grid refinement strategy is to compute error indicators from an existing solution. The aim during this work was to find an error indicator which can be computed very easily and directly leads to the optimal grid, i.e. to a small error of the calculated inductance with least number of unknowns in the corresponding linear equation. As the current density is constant in the example shown in Fig. 3.3 grid refinement is investigated only with respect to the magnetic vector potential.

Three error indicators have been investigated.

- **The energy indicator** is given by

$$I_{energy} = W_{mag} = \frac{1}{2} \int_V (\nabla \times \mathbf{A})^T \frac{1}{\mu} (\nabla \times \mathbf{A}) dV, \quad (3.8)$$

where V denotes the volume of a grid element and W_{mag} denotes the magnetic field energy stored in this element.

- **The mixed mode indicator** is given by

$$I_{mixed} = W_{mag} \frac{\|f_{mixed}\|}{\|f_{mixed} + f_{linear}\|}, \quad (3.9)$$

where f_{mixed} stands for a subspace of f in Eq. (3.7) which contains exclusively mixed modes, i.e. $f_{mixed}(x, y, z) = exy + fyz + gzx + hxyz$. Correspondingly f_{linear} contains only linear modes. The ratio between mixed and linear mode contribution is weighted by the magnetic field energy stored in the element. The constant part in Eq. (3.7) is omitted, because it does not contribute to the elements energy.

- **The higher mode indicator** is given by

$$I_{hm} = \frac{1}{2} \alpha_{hm}^2 \lambda_{hm}, \quad (3.10)$$

where λ_{hm} denotes the highest eigenvalue of the stiffness matrix of grid elements and α_{hm} is the highest modal coefficient determined by projecting the field solution on the highest orthogonal mode. Hence Eq. (3.10) denotes the magnetic field energy contribution of the highest mode.

Note that all secondary fields as the curl of the magnetic vector potential $\nabla \times \mathbf{A}$ are calculated like in the center of grid elements and hence are constant in each grid element.

Refined grids are constructed in the following manner: Field solution and corresponding error indicators are computed on the initial grid. The average of all indicator values defines a threshold value. All grid elements with error indicator above the threshold value are refined during the grid refinement step. Refinement of a grid element is done by splitting it into eight equally shaped smaller grid elements. Computation of a field solution and subsequent grid refinement is repeated until the error of the simulated inductance is sufficiently small. `SOLIDISISE` however

imposes an additional constraint on grids: the degree of refinement of neighboring grid elements can only differ by one, i.e. once a grid element is split and the neighbor is not, the first element cannot be split any further during subsequent grid refinement steps. In order to circumvent such dead locks during refinement the error indicator can “diffuse” across element boundaries. Increasing the number of diffusion steps however leads to less significance of the original error indicator, i.e. all error indicators lead to similar grid refinement once the number of diffusion steps is increased too much.

3.2.1 Example

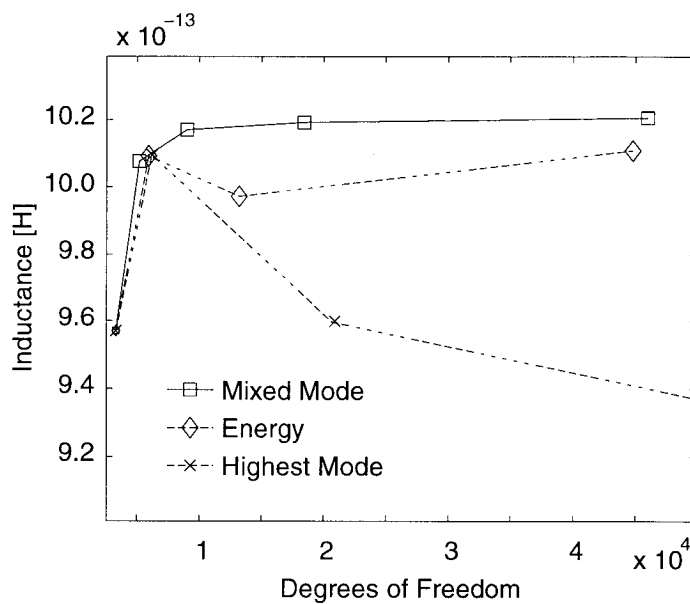


Figure 3.5: *Dependence of simulated self inductance on grid refinement (number of degrees of freedom used for modeling the magnetic vector potential) and grid refinement technique. Distance between conductors and grid boundary $d = 15\mu\text{m}$ (c.f. Fig. 3.3).*

As an example for different grid refinement techniques the same simple structure (Fig. 3.3) as in the previous section Sec. 3.1 has been investigated. Due to the sometimes high number of required degrees of freedom for obtaining a result with sufficient accuracy, the distance between bricks and grid boundary was chosen $d = 10\mu\text{m}$. Since the current density is constant in bricks, no grid refinement is necessary for improving the quality of the current density solution. Here, grid refinement is investigated with respect to the magnetic vector potential only.

Figure 3.5 shows the dependence of the simulated self inductance of one rectangular brick on the number of degrees of freedom used for modeling the magnetic vector potential and the dependence on the deployed error

indicator. The magnetic field energy was calculated from the magnetic vector potential and the electric current density with Eq. (2.53). Note that subsequent values on the x-axis denote results from subsequent grid refinement steps. During this simulation the number of diffusion steps for diffusion of the grid refinement indicator has been set to two for all refinement methods. Less than two diffusion steps caused dead locks during grid refinement and therefore three different results were obtained. More than two diffusion steps lead to the same convergence characteristics as shown in Fig. 3.5, whereas due to additional broadening of the refinement indicators the number of degrees of freedom was larger after the same number of grid refinement steps. Here, also the energy indicator and the mixed mode indicator lead to almost the same result whereas the highest mode indicator did not. The mixed mode indicator in this example however performs slightly better than the energy indicator. The number of degrees of freedom does not increase as fast after each grid refinement step and better results are obtained with less degrees of freedom. Hence, the mixed mode indicator seems to hit the critical locations in the grid better than the energy indicator.

Results of the field simulations are shown in Fig. 3.6. Current flows perpendicular to the cut plane. The maximum of the magnetic vector potential lies in the center of the brick and decreases with increasing distance. The maximum of the magnetic field flux amplitude is located where the gradient of the magnetic vector potential is maximum, i.e. on a ring around the brick. Note that the magnetic vector potential in fact decreases very quickly. Already at the boundary of the shown detail, its magnitude is below the resolution of the visualization tool. This clearly shows how sensitive a simulated inductance value reacts on close grid boundaries. The magnetic flux density also decays very quickly.

Figure 3.7 shows a cut through the initial grid of the geometry in Fig. 3.3 and refined grids after four grid refinement steps with different error indicators used. Both energy indicator Eq. (3.8) and mixed mode indicator Eq. (3.9) generate rather similar grids with strong refinement near the conductor walls. Hence the influence of the additional weighting term in Eq. (3.9) seems to be close to unity, which means that energy contributions mostly stem from mixed modes in Eq. (3.7). The higher mode indicator Eq. (3.10) puts emphasis on refinement at the corners of the geometry where equipotentials of the magnetic vector potential are diagonal with respect to initial grid lines. Because of the low quality results obtained, this does not seem to be an appropriate strategy.

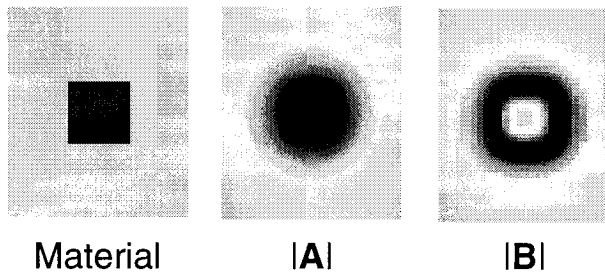


Figure 3.6: *Left: cut through brick shown in Fig. 3.3, only material shown. Current flows perpendicular to the shown cut. Center: Absolute value of magnetic vector potential. Right: Corresponding magnitude of magnetic field flux (Color map is linearly scaled).*

3.3 Extraction of Magnetic Field Energy

Computation of the magnetic field energy with Eq. (2.52d) relies on a field solution in a small part of the whole grid only. Sometimes it can be useful to reduce numerical errors by extracting results from the whole grid (e.g. in `DESSISISE` during computation of ohmic losses). It has already been shown in Sec. 2.5.3 that the magnetic field energy can also be extracted from the magnetic flux density with Eq. (2.52a). Here, energy computation not only involves an integration of field variables inside the conductor volume but on the whole grid. Figure 3.8 shows the calculated self inductance with increasing grid refinement. During grid refinement the mixed mode error indicator Eq. (3.9) was used, because in Sec. 3.2.1 this indicator performed best. The distance between bricks and grid boundary was $7\mu\text{m}$.

It shall briefly be noted again that as in case of the error indicators magnetic field flux density and magnetic field both are calculated from the derivative of the magnetic vector potential in the center of grid elements only. Hence both fields are constant inside grid elements. The magnetic flux density is calculated from the magnetic vector potential with Eq. (2.5) and the magnetic field is calculated from the magnetic flux density with Eq. (2.2a). Obviously magnetic field computation from these secondary fields with Eq. (2.52a) performs a lot worse than energy computation with Eq. (2.52d), where only a small part of calculated field values is taken into account. Where the latter method leads to convergence with approximately 10000 degrees of freedom, the first method needs more than 70000 degrees of freedom in order to yield results with

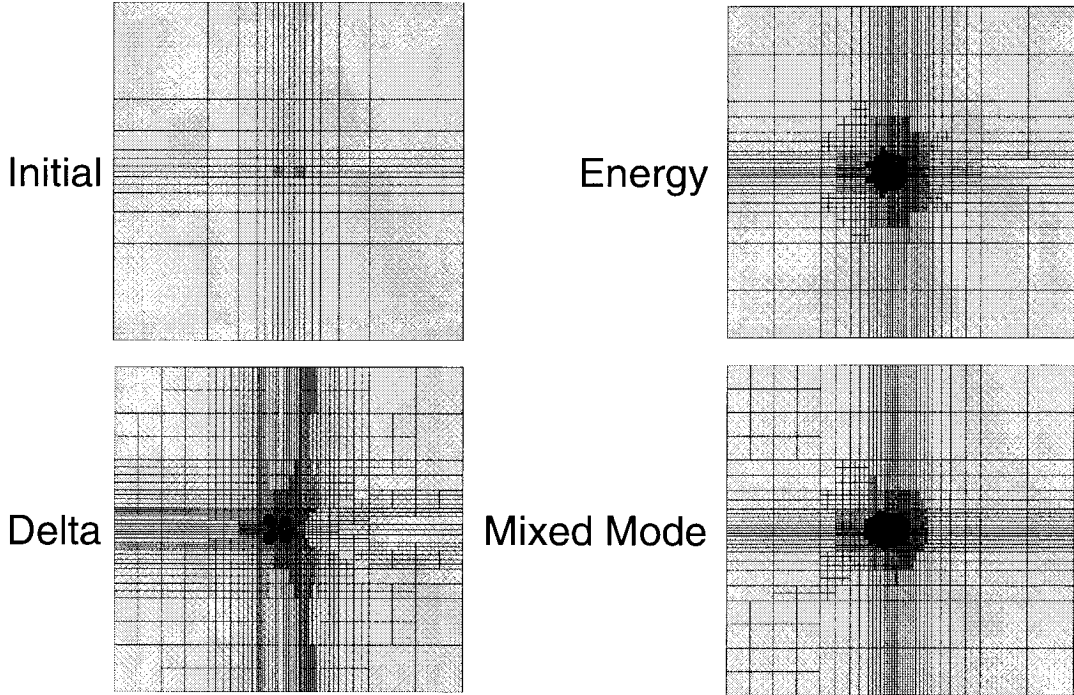


Figure 3.7: *Cut through refined grids. Refinement strategy is indicated next to the pictures. Here, the distance d between conductors and grid boundary is $10\mu m$.*

same accuracy. Furthermore, the calculated energy value always lies below the energy calculated with Eq. (2.52d).

In this paragraph the error of the simulated magnetic field energy introduced by taking the curl of the magnetic vector potential in the center of elements only is analyzed. The integral Eq. (2.52a) is evaluated for one grid element only. Because of $\int \mathbf{H}(\mathbf{r}) \cdot \mathbf{B}(\mathbf{r}) d^3r = 1/\mu \int_V B_x^2(x, y, z) + B_y^2(x, y, z) + B_z^2(x, y, z) dx dy dz$, only the energy stored in one coordinate direction (x-direction) is evaluated. Because of Eq. (2.5)

$$B_x(x, y, z) = \partial_y A_z - \partial_z A_y. \quad (3.11)$$

With FEM interpolation (Eq. (3.7)) this becomes

$$B_x(x, y, z) = c_z + e_z x + f_z z + h_z xz - d_y - f_y z - g_y x - h_y xy, \quad (3.12)$$

where the α_i with $\alpha = a, b, \dots, g$ and $i = x, y, z$ denote the coefficients in Eq. (3.7) and the coordinate direction of \mathbf{A} respectively. Again due to symmetry integration Eq. (2.52a) is carried out for one coordinate direction only (again x-direction). In order to simplify Eq. (3.12), coefficients

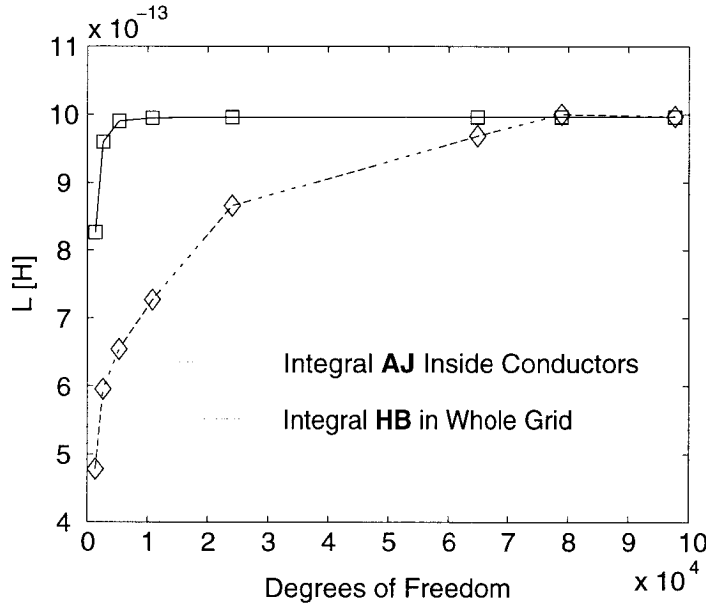


Figure 3.8: Inductance extraction with different magnetic field energy extraction methods. **AJ** denotes energy computation with Eq. (2.52d). **HB** denotes energy computation with Eq. (2.52a). Here, distance between conductors and grid boundary $d = 7\mu\text{m}$.

can be collected

$$B_x(x) = \alpha + \beta x. \quad (3.13)$$

Here, α includes all terms in Eq. (3.12) independent of x and β includes the remainder. Hence

$$\begin{aligned} & \int_0^\Delta (\alpha + \beta x)^2 dx \\ &= \int_0^\Delta \alpha^2 + 2\alpha\beta x + \beta^2 x^2 dx \\ &= \alpha^2\Delta + \alpha\beta\Delta^2 + \frac{1}{3}\beta^2\Delta^3, \end{aligned} \quad (3.14)$$

where Δ denotes the width of an element in x -direction. Using the curl of the magnetic vector potential in the center of grid elements $\bar{B}_x = \alpha + \beta\Delta/2$ only leads to

$$\begin{aligned} & \int_0^\Delta \alpha^2 + \alpha\beta\Delta + \frac{1}{4}\beta^2\Delta^2 dx \\ &= \alpha^2\Delta + \alpha\beta\Delta^2 + \frac{1}{4}\beta^2\Delta^3. \end{aligned} \quad (3.15)$$

Results differ in the final term $\beta^2\Delta^3$ only, where the energy is generally smaller when only the curl of the magnetic vector potential in the center of elements is taken into account. Note that the difference is weighted

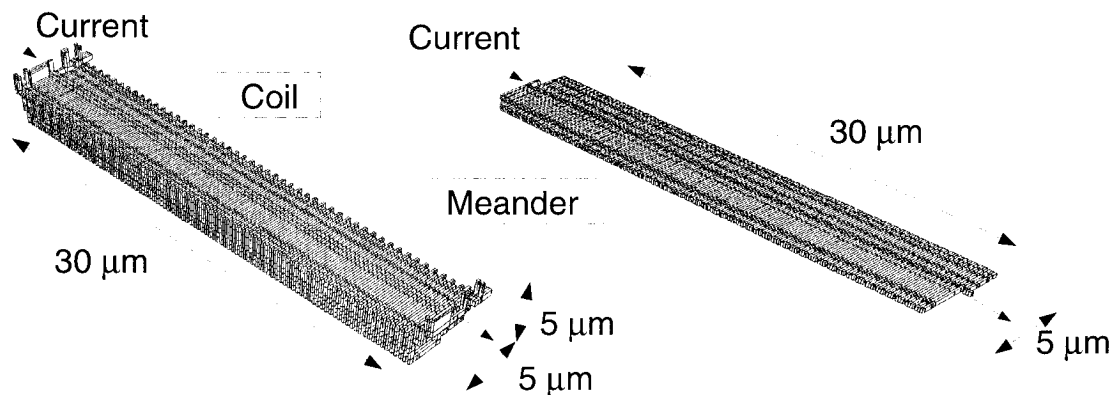


Figure 3.9: *Coil and meander conductor with dimensions and current flow indicated. These conductor geometries are used as a benchmark for comparison with other inductance extraction methods.*

with the mixed mode coefficient β and with the element width Δ . The result shown in Fig. 3.8) shows convergence only for a relatively high number of degrees of freedom used for modeling the magnetic vector potential, i.e. where Δ becomes small and hence this difference vanishes. This result therefore indicates, that a large part of the field energy is stored in the mixed modes of Eq. (3.7). Moreover it is shown, that energy extraction with integral Eq. (2.52a) is not necessarily better than with Eq. (2.52d) despite the fact that the latter integration is carried out only in a small part of the grid.

3.4 More Realistic Examples

The geometry shown in Fig. 3.3 is very small and simple compared to realistic problems. Two more complicated conductor structures have been chosen as benchmark for comparison with other inductance extraction approaches (c.f. Fig. 3.9). The left shows a coil geometry with length $30\mu\text{m}$ and square cross section of size $5 \times 5\mu\text{m}^2$. The coil consists of 50 windings. The right shows a meander structure with same length, width of $5\mu\text{m}$ and height less than $1\mu\text{m}$. The electrical conductivity is in both cases $\sigma = 89.2 \cdot 10^6 \text{S/m}$.

Figure 3.10 shows a cut through the grid used for computation of the magnetic vector potential of the meander structure shown in Fig. 3.9. It also shows a zoom with top view of the meander structure and a

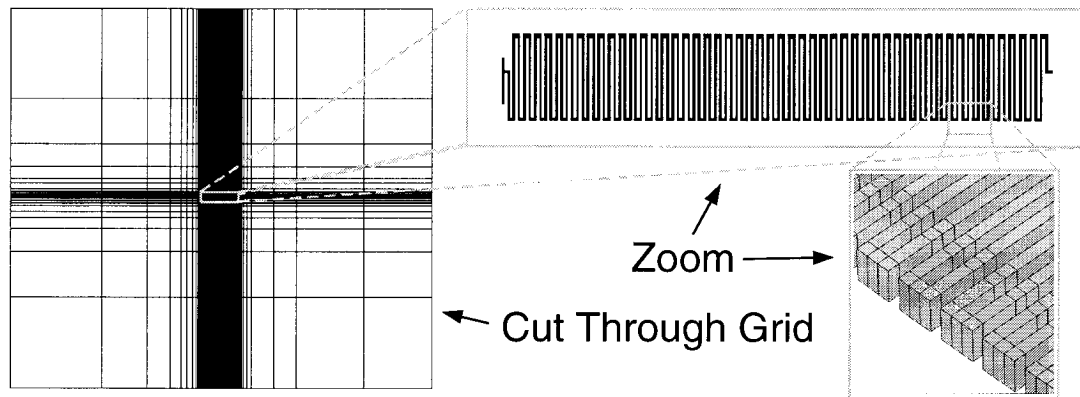


Figure 3.10: *Left: Cut through grid of a meander structure. Top left: geometry without grid. Bottom left: three dimensional view of corners with grid lines shown, too.*

magnification of conductor bends. In the center the grid is just as fine as it is necessary for resolution of the geometry. Note, that some additional grid lines have been added in order to allow the magnetic vector potential to decrease smoothly towards the boundary.

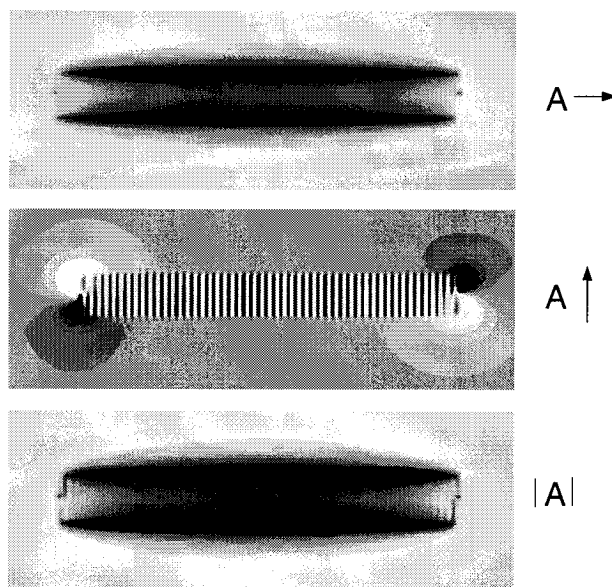


Figure 3.11: *Magnetic vector potential of a meander structure. Top: longitudinal component. Center: vertical component. Bottom: absolute value.*

Figure 3.11 shows three times the same cut through the meander structure with simulation results of the magnetic vector potential. The top shows the longitudinal component which corresponds to the net current flow from left to right (Eq. (2.24)). The center shows the transversal component of the magnetic vector potential. This picture clearly reflects the alternating current direction. Note also, that the transverse

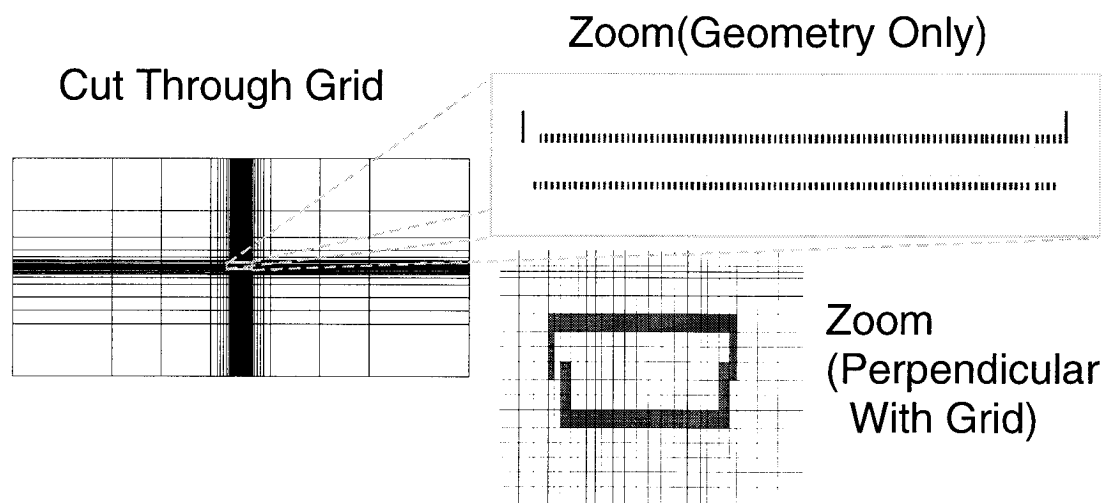


Figure 3.12: *Grid of coil geometry.*

component of the magnetic vector potential decreases very quickly with increasing distance from the conductor. This becomes clear when considering Eq. (2.28). Positive and negative contributions to the magnetic vector potential cancel each other out when the distance between alternating current and point of evaluation becomes large. The bottom picture shows the magnitude of all components of the magnetic vector potential. Here, the longitudinal component dominates the transverse component.

Figure 3.12 shows a cut through the grid used for modeling the magnetic vector potential of the coil geometry. Two zooms are given where one displays the conductor geometry in this cut without grid line and the other shows a perpendicular cut with geometry and grid lines. Basically, grid lines are inserted only where necessary in order to represent the geometry. However, as in case of the meander geometry, additional grid lines are inserted between the geometry and the grid boundary in order to allow the magnetic vector potential to decrease smoothly towards the grid boundary. Other grid lines are inserted in the coil center in order to better model the circular distribution of the magnetic vector potential. Simulation results of the magnetic vector potential are shown in Fig. 3.13, where the left picture shows the magnitude of $\mathbf{A}(\mathbf{r})$ in the same cut as shown on the right top of Fig. 3.12. The right picture shows $\mathbf{A}(\mathbf{r})$ in the cut on the right bottom of Fig. 3.12. Here, the vector field direction is indicated with arrows in the center of each grid element. The magnitude of $\mathbf{A}(\mathbf{r})$ is highest at the conductor and decreases with

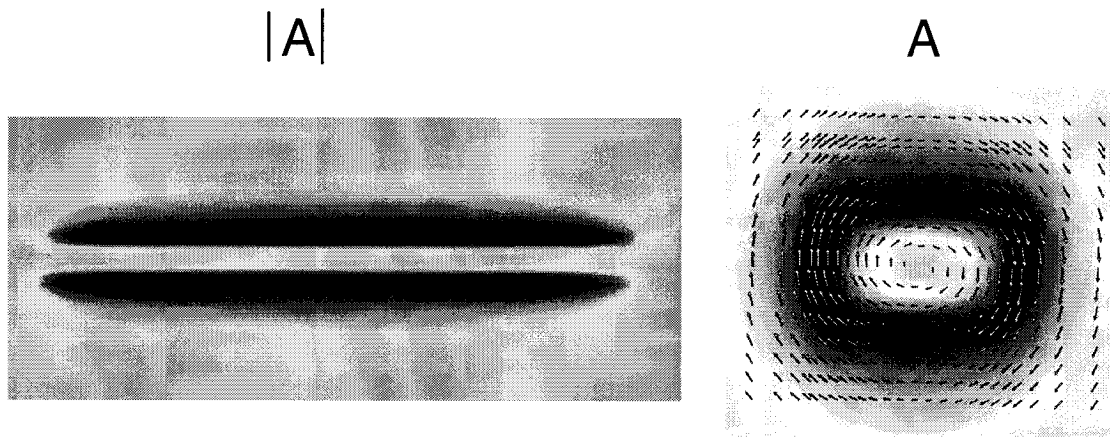


Figure 3.13: *Magnetic vector potential. Left: longitudinal cut with absolute value. Right: perpendicular cut with the direction of the magnetic vector potential shown.*

increasing distance from the conductor. Moreover it is zero in the center of the coil, because the direction of $\mathbf{A}(\mathbf{r})$ changes from one side of the coil to the other.

According to the results in Sec. 3.1 homogeneous Neumann boundary conditions Eq. (3.4) have been chosen for computation of the magnetic vector potential. The distance between conductors and grid boundary has been adjusted such that simulation results did not change when the distance was chosen to be even larger. Because the initial grid already was large, only one refinement step was possible for each geometry.

3.4.1 Results

Figure 3.14 shows the obtained static inductance results. These are compared with results obtained from other simulation methods which are explained later in this work. Since the two other simulation methods yield equal results, these values probably correspond to the correct solution. The x-axis shows the number of degrees of freedom used for modeling each component of the magnetic vector potential. Results with higher number of degrees of freedom correspond to results obtained after one grid refinement step. In case of the meander geometry the result obtained after grid refinement is worse than without refinement. The solution is obviously not independent from the grid and therefore probably not correct (apart from the order of magnitude). How many degrees

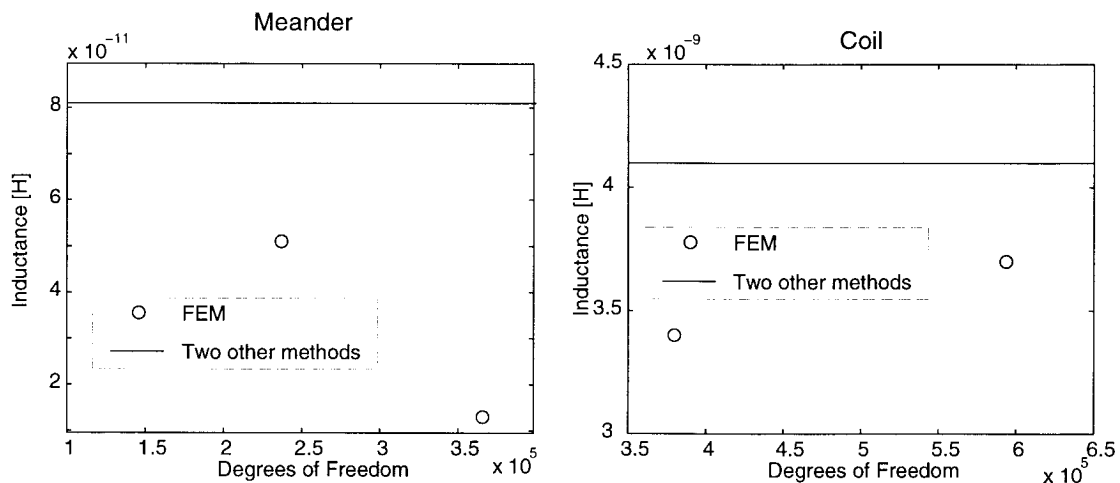


Figure 3.14: *FEM results of static inductance extraction. Left: Meander. Right: Coil. Circles indicate FEM results with respect to the number of degrees of freedom used for modeling each component of the magnetic vector potential. Solid lines indicate results obtained from two other simulation methods.*

of freedom will be necessary in order to obtain a good solution can be estimated from the results in Sec. 3.2.1 where around 10000 degrees of freedom were required for inductance extraction of one rectangular conductor. Most grid refinement was required in the vicinity of the conductor. In case of the meander geometry the magnetic vector potential changes more dramatically in the conductor vicinity and therefore probably here a much higher grid refinement is required. Compared to the computation of the magnetic vector potential the time required for the computation of the current density distribution is negligible. Here, the current density was modeled with 6164 degrees of freedom and 27611 degrees of freedom without grid refinement and after the first grid refinement step respectively. Obtaining the first solution of $\mathbf{A}(\mathbf{r})$ took 15min with 800MB of memory. Obtaining the field solution for the refined grid took another 25min with 1.2GB of memory. Due to high memory requirement for the preconditioner, solving the matrix equation with higher number of degrees of freedom was not feasible.

The quality of the result for the coil conductor is higher. Here, less grid refinement in the conductor vicinity is required, because the current direction does not change between neighboring windings and the magnetic field distribution inside the coil is homogeneous. Here, the current density was modeled with 18564 degrees of freedom and 19998 degrees of

freedom without refinement and after one adaptive grid refinement step respectively. Obtaining the first solution of the magnetic vector potential took 25min with 1.2GB of memory. Obtaining the field solution for the refined grid took another 40min with 1.6GB memory.

All simulations have been performed with a Compaq AlphaServer ES40 with 4x667 MHz.

3.5 Discussion

Clearly the FEM as used here is at its limits, because simple iterative solver routines become unstable when the number of unknowns exceed 500000. Beyond that multi grid methods have to be used like in a very recent approach for capacitance extraction. Two approaches for two dimensional capacitance extraction have been found in literature [46, 47]. To the authors knowledge, the proposed algorithms have not been extended towards inductance extraction so far.

The following problems have been encountered and these solutions can be found in literature.

1. **Fine initial grid:** This is the main disadvantage of the used structured grid formalism. The general FEM puts only few constraints on the shape of grid elements. Here, grid lines have to be introduced in order to represent the conductor geometry. Due to the formalism these stretch from one grid boundary to the opposite. Correspondingly a fine grid is generated near the boundary where in fact a coarse grid would be sufficient. In order to avoid fine grid resolution near the grid boundary, mixed element grids can be used. Generation of mixed element grids, however, requires a higher computational effort.
2. **Boundary:** Here, only very simple boundary conditions have been investigated in detail. Some other boundary conditions are given in [48]. The investigated “ballooning” technique is rather simple. Also quite simple is the use of “infinite elements”, where elements with a given decay (e.g. $1/r$ or exponential) are attached to the grid boundary. These infinite elements conserve the sparsity of the FEM matrix which allows fast matrix assembly and solution and

are therefore quite accepted in engineering. The decay however depends on the modeled field. It has been shown in Sec. 2.5.4 that despite of the long range $1/r$ interaction between current filaments fields do not necessarily decay like $1/r$. The user therefore has to be very careful when infinite elements are used. A more complicated and more accurate boundary condition is obtained by combining the FEM with the **B**oundary **E**lement **M**ethod (BEM) [49]. The BEM uses Green's theorem Eq. (A.3) or its vector equivalent to transform a volume integral into a surface integral. Here, the field outside the grid is solved with the BEM, which is easy because only a homogeneous Laplace equation has to be solved. Inside the grid where Poisson or Helmholtz equations have to be solved, field solutions are obtained from FEM. At the boundary both solutions are coupled such that the derivative of the potential is continuous. Hence, an accurate solution to the unbound problem is obtained. A disadvantage of BEM is the resulting dense matrix equation. With n_b the number of nodes on the grid boundary each row of the coupled matrix associated with a node on the boundary therefore has at least n_b nonzero entries. Coupling of FEM with BEM first appeared as McDonald–Wexler algorithm [50]. Another possibility is to express boundary values as integrals over the current distribution with Eq. (2.28). With n_c the number of nodes representing the current density here at least n_c nonzero entries in every row associated with a node on the boundary is introduced. Boundaries should be chosen, such that the product $n_b \cdot n + b$ and $n_b \cdot n_c$ is minimal respectively. This strategy results in a matrix with fewest entries. Sometimes it can be useful to choose a grid boundary on the conductor surface directly, in case of more complicated conductor geometries it can be useful to choose a grid boundary with a higher distance from the conductors and model the empty space in between with FEM. Note, that as grid elements can be larger with increasing distance from the conductor, n_b does not necessarily increase proportional to the size of the grid .

3. **Grid refinement:** It is astonishing that inductance results from field distributions shown in Fig. 3.13 and Fig. 3.11 are not exact despite the fact that solutions “look quite good”. Results from Sec. 3.2 and Sec. 3.3 indicate that grid refinement is required where the mixed mode part of Eq. (3.7) and magnetic field energy density are high. This strongly indicates the need for p-refinement. However currently no commercial FEM-Electromagnetic s code is

available where p-refinement is used. This is probably because no simple refinement indicator exists which tells whether to use p-refinement or h-refinement. Another reason could be that p-refinement increases the number of unknowns per element and therefore the gain in computational efficiency is small compared to the effort to decide which refinement to use and where to refine the grid. Moreover the dense grids in Fig. 3.7 indicate that a small increase of the polynomial order in Eq. (3.7) might not really reduce the number of required grid elements. It seems rather that high degree polynomials are required for interpolation. With high degree polynomials used for interpolation, however, sparsity of the FEM matrix is reduced and obtaining a numerical solution with iterative solver routines becomes more difficult. The simulation of the rectangular conductor (c.f. Fig. 3.5) started with an initial grid with 3500 degrees of freedom. Above 10000 degrees of freedom the result is quite accurate. At this stage almost no grid refinement took place near the grid boundary. Hence, grid resolution can be coarse near the grid boundary and has to be fine near the conductor. The distance between grid boundary and conductor does not seem to be the limiting factor of FEM in case of self inductance simulations. In the meander example it comes out clearly, that the limiting factor is in fact the resolution of the magnetic vector potential near conductors. This is different in the case of an inductive coupling between distant conductors (when the conductor distance is in the range of the conductor grid-boundary distance). Here, field distributions are smooth, but influenced by the close grid boundary. It shall be added that a coupling of BEM and FEM does not reduce the necessity of grid refinement inside the conductors and on the grid boundary. It is therefore assumed that the meander conductor example might also be difficult to solve with such a hybrid method.

3.6 Quasistatic Approximation

Numerous publications exist on FEM for the use of the simulation of the skin effect. Here either Eqs. (2.46) and (2.47) or Eqs. (2.66) and (2.67) are solved simultaneously. It has already been explained in Sec. 2.7 that the use of the current vector potential inside conductors and magnetic

scalar potential everywhere reduces the number of unknowns in the FEM matrix equation at the cost of defining cut planes. When linear nodal elements are used, inside conductors four unknowns are required per node, only one outside. Since reducing the number of unknowns is the only way to increase the complexity of models for FEM this is an attractive approach.

FEM simulations are done in frequency as well as in time domain. Some recent approaches for transient skin effect simulations include [51, 52]. Note again, that in case of time domain simulations the associated matrix equation has to be solved for every single time step. A good overview on FEM treatment of skin effect in frequency and in time domain is given in [17] and [34]. Due to the required simultaneous solution of potentials, examples are usually less complicated than examples for static inductance extraction shown in Fig. 3.9.

3.7 Conclusions

The influence of grid boundaries on static inductance results (self- and coupling-inductance) has been investigated for a very simple test structure. Here, influence of Neumann boundary conditions is smaller than the influence of Dirichlet boundary conditions. Results from grid refinement and from magnetic field energy computation strongly indicate a need for higher degree polynomials for magnetic vector potential interpolation (p-refinement), when high accuracy (self-)inductance results are required. Examples are given where necessary grid refinement limits the use of FEM rather than the influence of boundary conditions. Due to the encountered difficulties this approach has not been extended towards inductance extraction including the skin effect.

Seite Leer /
Blank leaf

Static Inductance Extraction by Means of the Monte Carlo Method

The difficulties encountered with FEM regarding necessary grid refinement for the computation of the magnetic vector potential and the influence of the boundary conditions made it necessary to develop a new method for static inductance extraction. The new approach is based on the current density computation by means of FEM with subsequent magnetic field energy estimate by means of Monte Carlo sampling. Due to the long range interaction in the integral Eq. (2.57), the integrand is “almost” constant. The idea of Monte Carlo sampling is as follows: when the integrand is almost constant, few energy samples suffice in order to obtain an energy estimate with high accuracy. The sampling process hence will be short. Furthermore, no equation has to be solved for computation of the magnetic vector potential and therefore memory requirements are low. This chapter is structured as follows. First, Monte Carlo sampling including computation of an error estimate is presented. Then convergence for simple geometries is analyzed, the implementation of the algorithm is explained and a first example – computation of the inductance of a bonding wire – is given. The sampling method could be highly accelerated with use of several different variance reduction techniques which are motivated and explained. Examples are given and convergence is analyzed in detail for geometries already investigated in the previous chapter shown in Fig. 3.9.

4.1 Monte Carlo Sampling

For Monte Carlo sampling the sample mean method [53] is used. As in case of the FEM for static inductance extraction, inductance results are obtained from the magnetic field energy and from total conductor currents with Eq. (2.53) and Eq. (2.50). In order to calculate the magnetic field energy by means of the Monte Carlo method, the volume integral Eq. (2.57) is expanded by a probability density $p_2(\mathbf{r}, \mathbf{r}')$, which depends on both locations \mathbf{r} and \mathbf{r}'

$$W_{ij} = \frac{\mu}{8\pi} \int_V \int_V \frac{\mathbf{J}_i(\mathbf{r})\mathbf{J}_j(\mathbf{r}')}{|\mathbf{r} - \mathbf{r}'|} d^3r d^3r'$$

$$= \frac{\mu}{8\pi} \int_V \int_V \frac{\mathbf{J}_i(\mathbf{r})\mathbf{J}_j(\mathbf{r}')}{|\mathbf{r} - \mathbf{r}'|p_2(\mathbf{r}, \mathbf{r}')} p_2(\mathbf{r}, \mathbf{r}') d^3r d^3r'. \quad (4.1)$$

$$(4.2)$$

The probability density has to be normalized, i.e.

$$\int_V \int_V p_2(\mathbf{r}, \mathbf{r}') d^3r d^3r' \equiv 1, \quad (4.3)$$

where V denotes the conductor volume, only. Equation (4.2) is in fact an expectation value.

$$W_{ij} \approx \frac{1}{N} \sum_{\kappa} W_{ij\kappa}, \quad (4.4)$$

with N the number of samples and samples

$$W_{ij\kappa} = \frac{\mu}{8\pi} \frac{\mathbf{J}_i(\mathbf{r}_{\kappa})\mathbf{J}_j(\mathbf{r}_{\kappa}')}{|\mathbf{r}_{\kappa} - \mathbf{r}_{\kappa}'|p_2(\mathbf{r}_{\kappa}, \mathbf{r}_{\kappa}')}. \quad (4.5)$$

In Eq. (4.5) for each sample two locations \mathbf{r}_{κ} and \mathbf{r}_{κ}' are selected. Locations are not re-used and therefore all energy samples $W_{ij\kappa}$ are independent from each other.

4.2 Error Estimate

Errors of inductance results can be traced back to two independent sources. One error source is the current density distribution, which

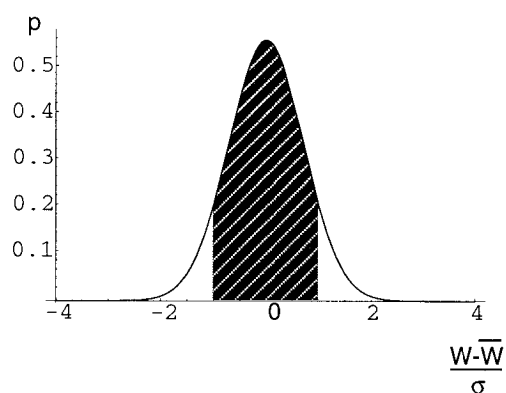


Figure 4.1: *Distribution of sample mean results according to the central limit theorem of statistics [53]. Deviations are given in terms of the standard deviation σ (Eq. (4.6)). The integral between $[-\sigma, \sigma]$ corresponds to the probability of obtaining a result within this interval.*

interval	probability
$[\bar{W} - \sigma, \bar{W} + \sigma]$	0.843
$[\bar{W} - 2\sigma, \bar{W} + 2\sigma]$	0.9954
$[\bar{W} - 3\sigma, \bar{W} + 3\sigma]$	0.99998
$[\bar{W} - \infty, \bar{W} + \infty]$	1

Table 4.1: *Probability for obtaining an energy estimate within the interval around the exact energy value \bar{W} . The probability is the integral below the probability density distribution shown in Fig. 4.1 in the respective interval. The probability for obtaining an energy estimate inside an infinitely wide interval equals one.*

in most cases is not exact. In order to minimize the influence of an inaccurate current density result, grid refinement techniques should be applied. Corresponding changes of inductance results, however, only provide a differential error. An absolute error cannot be given.

Another error comes from the magnetic field energy estimate by means of Monte Carlo sampling. It is now explained, how this error can be computed. Furthermore it is shown that in fact an absolute error can be given.

Since all energy samples $W_{ij\kappa}$ are computed independent from each other, the central limit theorem of statistics [53] can be applied for computation of the (statistical) error of the average Eq. (4.4). The central limit theorem states that the average is normally distributed for multiple runs with different samples, when the number of samples N is large. The error of the result ΔW_{ij} can therefore be calculated from the variance σ^2 of the sampled values $W_{ij\kappa}$

$$\sigma^2 = \frac{1}{N} \sum_i W_{ij\kappa}^2 - \left(\frac{1}{N} \sum_i W_{ij\kappa} \right)^2 \quad (4.6)$$

and from the number of samples.

$$\Delta W = 3 \frac{\sigma}{\sqrt{N}}. \quad (4.7)$$

The “three sigma” criterion gives a very good measure for the computed error. According to values given in Tab. 4.1 less than $2 \cdot 10^{-5}\%$ of multiple computations lead to a result with larger error than estimated. Once a relative error, e.g. 5%, is chosen, σ and the approximate magnetic field energy W are computed with Eqs. (4.6) and (4.4) respectively. The simulation can be stopped when $\Delta W/W < 0.05$, with ΔW being the error estimate from Eq. (4.7). In case ΔW is computed with only 1σ instead of 3σ it becomes less probable that the computed value lies within the interval $[\bar{W} - \Delta W, \bar{W} + \Delta W]$. According to Tab. 4.1 16% of results are outside of this confidence interval. Accepting this less tight error criterion however accelerates the algorithm by a factor of 9.

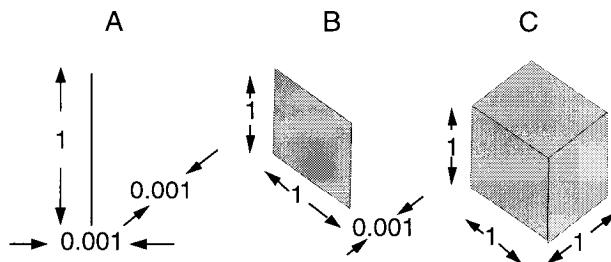


Figure 4.2: Geometries *A*, *B* and *C* for which the inductance is calculated with Monte Carlo sampling.

4.3 Convergence

In this section convergence during sampling for typical geometries is discussed. For some geometries sampling converges faster than for others. Here three example geometries are analyzed and hints are given on how to interpret the results for any type of geometry. The three example geometries are shown in Figure 4.2.

Geometry “A” is a long conductor, “B” is a flat conductor and “C” is a cube shaped conductor. “A”, “B” and “C” are extended in one, two and three dimensions respectively. For this discussion homogeneous current densities $\mathbf{J} = 8\pi/\mu \cdot p_2$ with constant probability density p_2 are assumed. The energy samples $W_{ij\kappa}$ in Eq. (4.5) therefore become $W_{ij\kappa} = 1/(|\mathbf{r}_\kappa - \mathbf{r}_\kappa'|)$. In order to understand convergence of the algorithm, it is important to analyze the distribution of inverse distances in these simple geometries and where the average is, because the average corresponds to magnetic field energy and inductance.

Distributions are shown in Fig. 4.3. In case “C” the expectation value is very close to the most probable value. This distribution also has the highest maximum. The maximum of the distribution decreases in case “B” and “A” and the distance between expectation value and most probable value increases. Figure 4.4 shows the running average of inductance calculations of Eq. (4.4) for multiple simulations. Since the average is also the most probable value in case “C”, fast convergence here as well as slower convergence in cases “B” and “A” can be understood. A measure for convergence is the standard deviation of the sampled values σ which is also shown.

The average or expectation values of distributions shown with dashed lines in Fig. 4.3 in “2D” and “3D” correspond to the inductances of geometries “B” and “C”. The inductance of a line (1D) is actually not defined. Here, the expectation value is the inductance of “A”. The

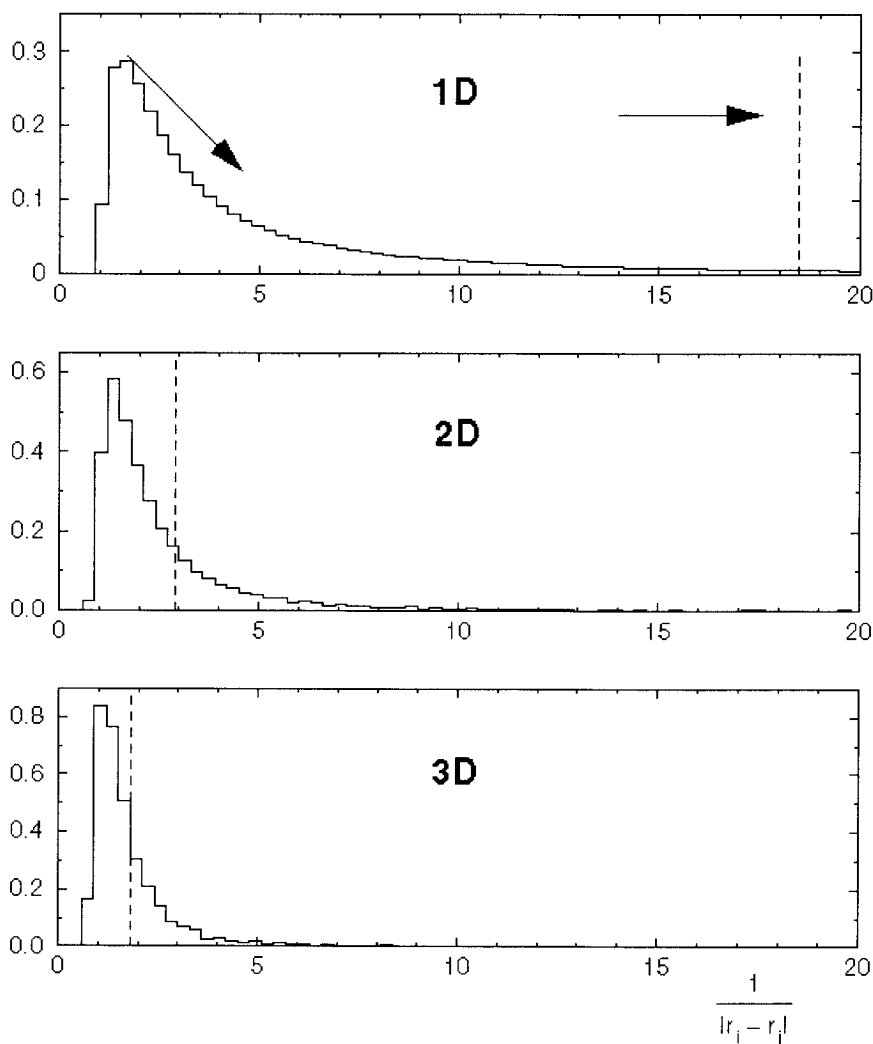


Figure 4.3: Distribution of values $1/|r-r'|$ on a line with length 1 (1D), on a square shaped surface with area 1 (2D) and on a cube with volume 1 (3D). For computation of distributions in each case $\approx 250.000.000$ terms were taken into account. Locations r and r' were taken from regularly distributed coordinates. Distributions are normalized. The average of each distribution is marked with a dashed line.

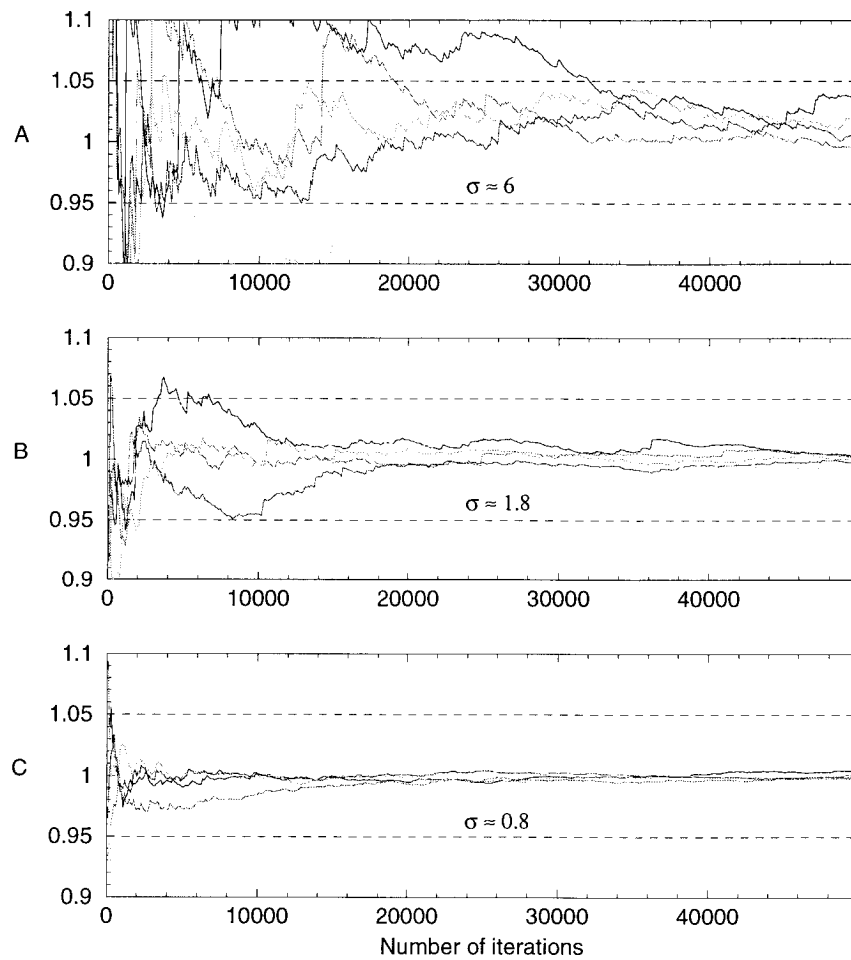


Figure 4.4: *Running average of inductance divided by the analytical result for geometries shown in Figure 4.2. The standard deviation σ of the sampled normalized values is also shown.*

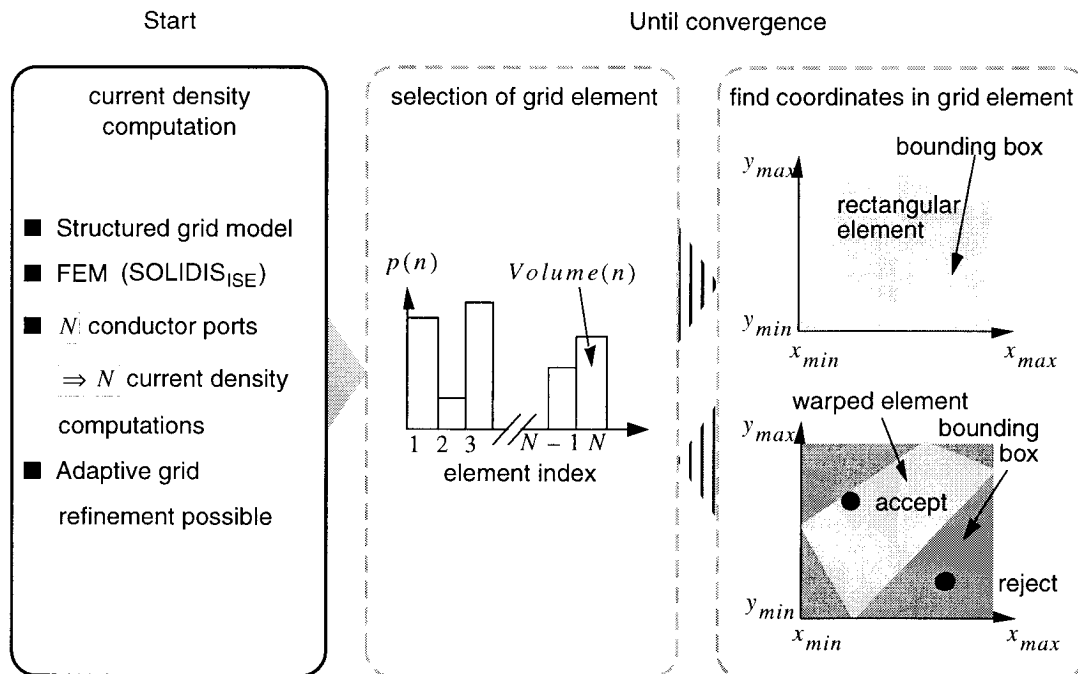


Figure 4.5: Coupling with FEM and implementation of the Monte Carlo algorithm.

inductance, i.e. the expectation value was calculated analytically for geometries with even higher aspect ratio than of “A” and it was found a strong increase. This increase of the inductance comes with a further broadening of the distribution of inverse distances which is indicated with arrows in Fig. 4.3. A broader distribution of inverse distances leads to a higher standard deviation of sampled values for geometries with aspect ratio greater than the aspect ratio of “A” and therefore slower convergence.

Convergence for real examples is difficult to predict. Inhomogeneous current density and complicated shape alter the results from the previous discussion. An example for the influence of an inhomogeneous current density is given later in this chapter in Sec. 4.7.2 where despite of the cube shaped geometry convergence is rather slow.

4.4 Implementation

This section briefly explains the implementation of the algorithm. An overview is shown in Fig. 4.5. The algorithm starts with necessary current density computations which are performed by the FEM program `SOLIDISISE`. It shall be noted that any other method – also analytical methods – for current density computations can be used here. In a second stage magnetic field energies are estimated with the previously described Monte Carlo algorithm. For computation of self and coupling inductances Eq. (2.57) is used. Since magnetic field energies are symmetric, i.e. $W_{ij} = W_{ji}$, in order to determine the full inductance matrix Eq. (2.55) in case of N_c conductor ports $1/2N_c(N_c + 1)$ magnetic field energy estimates are required (c.f. Sec. 2.5.4). For each single magnetic field energy estimate a high number of random locations inside the conductor volume has to be generated and corresponding current densities have to be retrieved from the FEM result. It is not feasible to generate random locations inside the bounding box of the whole set of conductors and then to try to find out whether a conductor has been hit at all, and if yes to find out which element is hit and what the current density is. This procedure would be too time consuming. A more efficient way for generation of random locations inside grid models of conductor geometries has been developed during this work and is presented in the following section.

4.4.1 Implementation of a Probability Density

This section describes the implementation of a probability density which allows the efficient generation of random locations inside grid models of conductor geometries. The same algorithm is also used for generation of joint probabilities, which are required for implementation of variance reduction techniques.

The most simple six dimensional probability density $p_2(\mathbf{r}, \mathbf{r}')$ is the constant probability density $p_2(\vec{r}, \vec{r}') = \text{const.}$ Due to Eq. (4.3)

$$p_2(\mathbf{r}, \mathbf{r}') = \frac{1}{V^2}. \quad (4.8)$$

Obviously the constant probability density factorizes

$$p_2(\vec{r}, \vec{r}') = p_1(\vec{r})p_1(\vec{r}'), \quad (4.9)$$

saying, that the two locations required for each sample in Eq. (2.57) can be chosen independently. For implementation the three dimensional probability density p_1 is again split into two probability densities

$$p_1(\vec{r}) = p_e(k)p_{kl}(\vec{r}). \quad (4.10)$$

The first factor p_e is the discrete, one dimensional probability of selecting grid element k . This probability density is indicated in the center of Fig. 4.5. The second p_{kl} is the constant three dimensional probability density for generating a random location inside element k . This probability density is shown on the right in Fig. 4.5. It is chosen constant for all investigated probability densities p_2 , because current density solutions do not yield information about different locations in the same element. Note that p_{kl} is different for all grid elements. Implementation for rectangular elements is straight-forward. However, when element corners are not rectangular, first a random location inside the bounding box of the selected element is generated, then a check is performed, whether the random location is in fact inside the element. In case the element is not hit, random generation of a location and checking is repeated. This step has to be repeated more often, if the element's volume differs largely from the volume of its bounding box.

The discrete probability density for random selection of a grid element $p_e(k)$ is implemented efficiently using partly the "Bucket Sort" or "Hash Sort" algorithm [54]. First, an array P_e with same length as number of grid elements ν is initialized with

$$P_e[k] = \sum_{i < k} V_i/V, \quad (4.11)$$

where V_i denotes the volume of grid element i and V denotes the total conductor volume. Elements k are selected randomly by generating a random number r from the interval $[0, 1)$. The problem then is to find the smallest index i , where $P_e[i] > r$. This is the same problem as finding the position where to insert an arbitrary number into a list of sorted numbers. Here the insertion part of the "Hash Sort" algorithm is used. During initialization of P_e a hash table also of length ν with equidistant entries k/ν is initialized. Entries in this table are indices i in P_e , where i is the smallest index with $P_e[i] > k/\nu$. This index gives the position where to start a linear search. When entries in P_e are equally spaced, the computational effort for finding an element is $O(1)$. The

worst case for finding an element would be $P_e[1] = 1 - 1/\nu$, i.e. one very large element and the rest is not resolved by the hash table. However hitting one of the small elements is unlikely and an analysis of the average computational effort has also to include the small probability of a long linear search. When the large element is hit, i.e. with probability $1 - 1/\nu$, the computational effort of the search algorithm is $O(1)$, because the large element is initially found. With probability $1/\nu$ one of the small elements is hit and the effort of finding it is $\nu/2$, due to the linear search. This gives an average effort of $O((\nu - 1)/\nu \cdot 1 + 1/\nu \cdot \nu/2) \approx 1,5 \cdot O(1)$, i.e. the effort is independent of ν , the number of elements. Clearly, the time and memory effort for setting up the probability density grows only linearly with ν . Information for normalization is available from $P_e[\nu]$ and does therefore not require an extra summation.

4.5 Example Bonding Wire

This section gives a first example of inductance extraction with the newly developed algorithm.

The top of Fig. 4.6 shows the electric potential in a bonding wire after one grid refinement step. Regions with strongly varying gradient of the electric scalar potential have been refined. The center shows a cut through the model with the amplitude of the corresponding current density. A magnification of the region around the right contact with current direction displayed is also shown.

Figure 4.7 shows the running average of the inductance during five different computations. Figure 4.8(a) shows the corresponding standard deviation divided by the running average. This value becomes stable after ≈ 50.000 iterations. This seems to be the necessary number of samples for application of the central limit theorem. Note that the standard deviation is between standard deviations of geometries A and B shown in Fig. 4.2. The corresponding error estimate is shown in Fig. 4.8(b). 150.000 iterations take 220 secs time. The final result is given with 2% accuracy. A result with 5% accuracy is already obtained after 25.000 iterations, i.e. after 35 secs (when the error estimate is computed with the three-sigma criterion Eq. (4.7)).

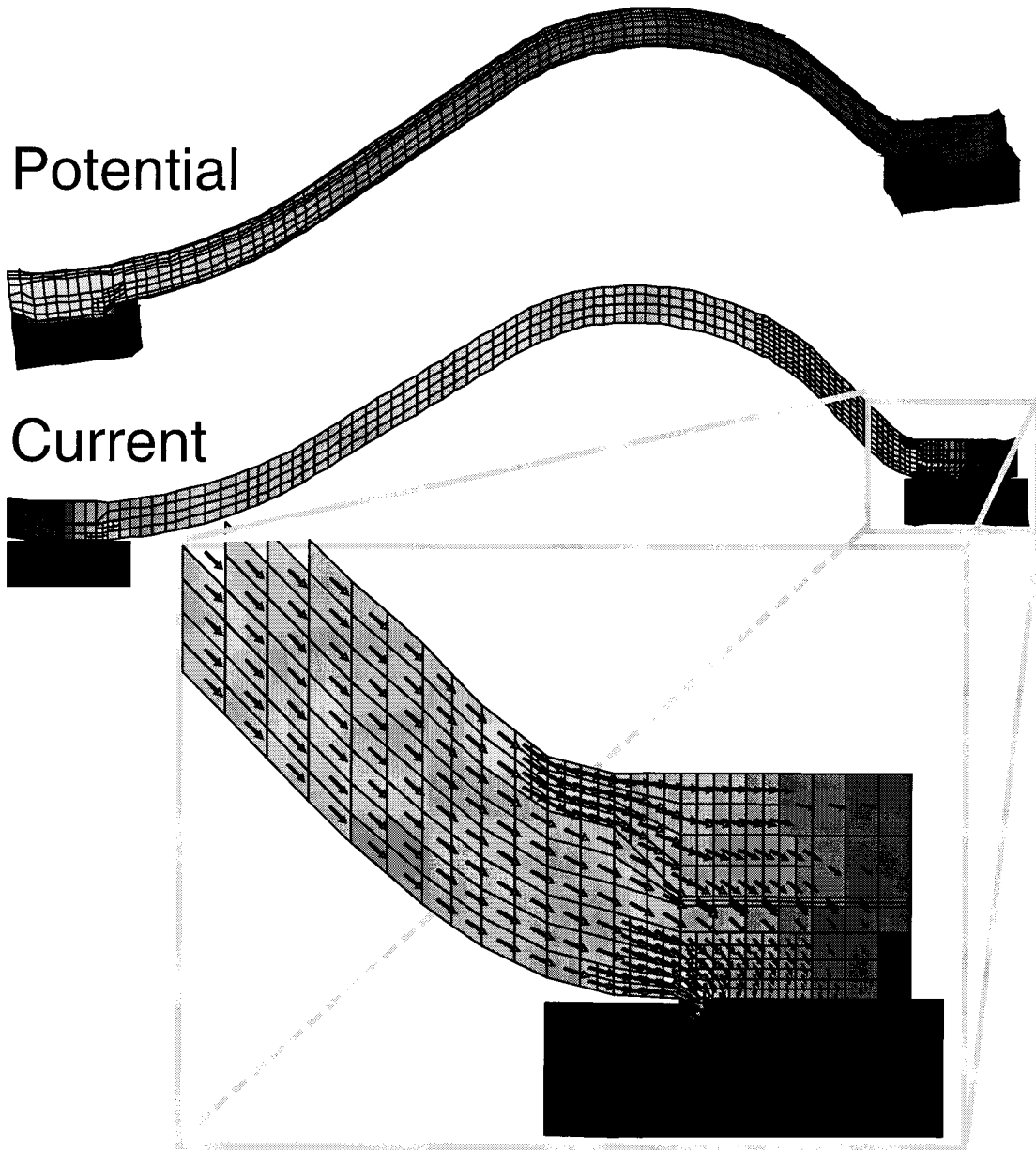


Figure 4.6: Top: Scalar electric potential in a bonding wire model. Center: Corresponding current density. Bottom: Magnification of right contact with current direction.

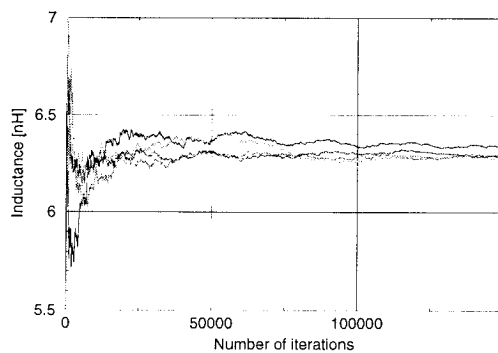


Figure 4.7: Inductance extraction of bonding wire shown in Fig. 4.6. Running average of inductance during Monte Carlo sampling. Five different computations are shown.

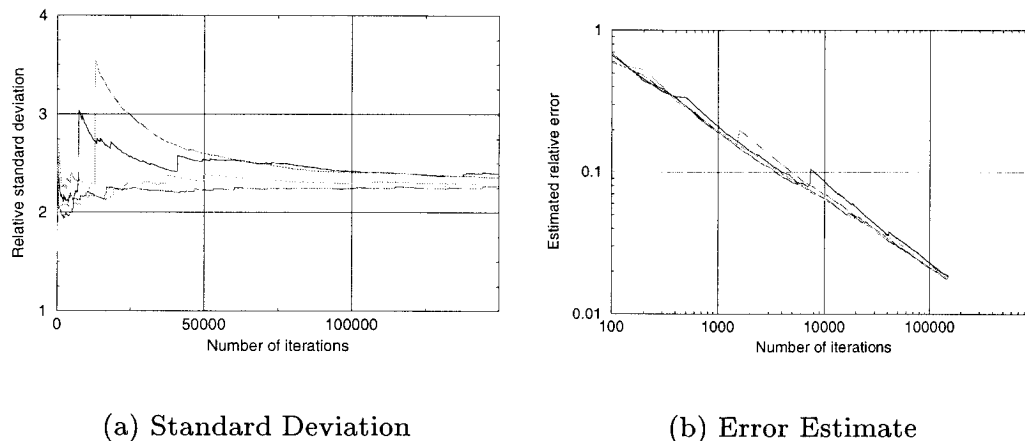


Figure 4.8: (a) Standard deviation divided by the running average (Fig. 4.7). Used for computation of an error estimate. (b) Running error estimates (relative error) for inductance values.

4.6 Variance Reduction Techniques

The aim of all variance reduction techniques is to reduce the variance of sampled values Eq. (4.5). When the variance Eq. (4.6) is reduced by a factor of four, the number of necessary samples for obtaining a result with same accuracy also is reduced by a factor of four Eq. (4.7).

Deployed variance reduction techniques [53] are

- importance sampling,
- stratified sampling,
- combinations of both.

All variance reduction techniques are implemented as explained in Sec. 4.4.1. The computational effort and the amount of memory needed for setting up all probability densities grows therefore only linearly with the number of elements. The time required for performing a Monte Carlo sample is always independent of the total number of grid elements. All investigated probability densities are summarized in Tab. 4.3.

The idea of importance sampling is to put as much easily accessible information as possible about the integrand in Eq. (2.57) into the probability density in order to obtain energy samples in Eq. (4.5) which are almost constant.

For stratified sampling the integral is separated

$$W = \sum_s W_s. \quad (4.12)$$

In this case the energy stored in every “stratum” s is calculated separately with Monte Carlo sampling. Before performing a sample of stratum s , this stratum is selected randomly with probability p_s . Then according to p_{2s} two random locations are selected from this stratum. Normalization is analogous to Eq. (4.3)

$$\begin{aligned} 1 &\equiv \sum_s p_s \int_V \int_V p_{2s}(\vec{r}, \vec{r}') d^3 r' d^3 r \\ &= \sum_s p_s. \end{aligned} \quad (4.13)$$

The average becomes

$$W \approx \sum_s p_s \frac{1}{N_s} \sum \kappa_s = 1^{N_s} W_{\kappa_s}. \quad (4.14)$$

Here, N_s denotes the number of samples of stratum s and W_{κ_s} denotes a sample from this stratum. The idea of stratified sampling is, that the sum of single variances is smaller than the variance of sampled values in the unsplit integral

$$\sum_s p_s \sigma_s^2 < \sigma^2.$$

The error estimate of energy W in Eq. (4.7) is modified. Here, the total error is given by

$$\Delta W = 3 \sqrt{\sum_s \frac{p_s^2 \sigma_s^2}{N_s}}. \quad (4.15)$$

4.6.1 Probability Densities 1 and 2

The easiest approach for importance sampling is to take the current density into account, i.e.

$$p_{2s}(\vec{r}, \vec{r}') \propto |J_s(\vec{r})||J_s(\vec{r}')|. \quad (4.16)$$

Note that in this case we also have to stratify in order to obtain a probability density which factorizes. Factorization is important, because otherwise locations could not be selected independently and time and memory requirements for setting up the probability density would grow $\propto \nu^2$, ν being the number of grid elements. Absolute current values have to be considered in order to fulfill condition $p_2 \geq 0$.

Stratification of integral Eq. (2.57) according to Eq. (4.14) is given by

$$W = \sum_{s=x,y,z} \frac{\mu}{8\pi} \int_V \int_V \frac{\vec{J}_s(\vec{r}) \cdot \vec{J}_s(\vec{r}')}{|\vec{r} - \vec{r}'|} d^3r' d^3r, \quad (4.17)$$

i.e. the magnetic field energy stored in the three coordinate directions is calculated separately.

Setting up the probability density p_{2s} is similar to the algorithm explained in Sec. 4.4.1. Instead of one array P_e , here three arrays P_{es} are needed, i.e. one for every coordinate direction. Entries in the P_{es} are

$$P_{es}[k] = \sum_{i < k} |J_{is}|V_i / \sum_l |J_{ls}|V_s,$$

where J_{is} denotes component s of the current density in element i and V_i denotes the volume of element i .

The difference between probability densities 1 and 2 in Tab. 4.3 is the probability for selection of a stratum p_s . In case of probability density 1, p_s is equal for all strata, i.e. $1/3$. In case of probability density 2, p_s is weighted according to $\sum_l |J_{ls}|V_s$. The samples according to Eq. (4.5) are in both cases

$$W_\kappa \propto \frac{\pm 1}{|\vec{R}_\kappa - \vec{R}_\kappa'|}. \quad (4.18)$$

Samples from elements with both positive or negative current density lead to a positive contribution to the total energy, samples from elements with opposite current density lead to negative contributions. Additionally elements with high current density are hit more often than

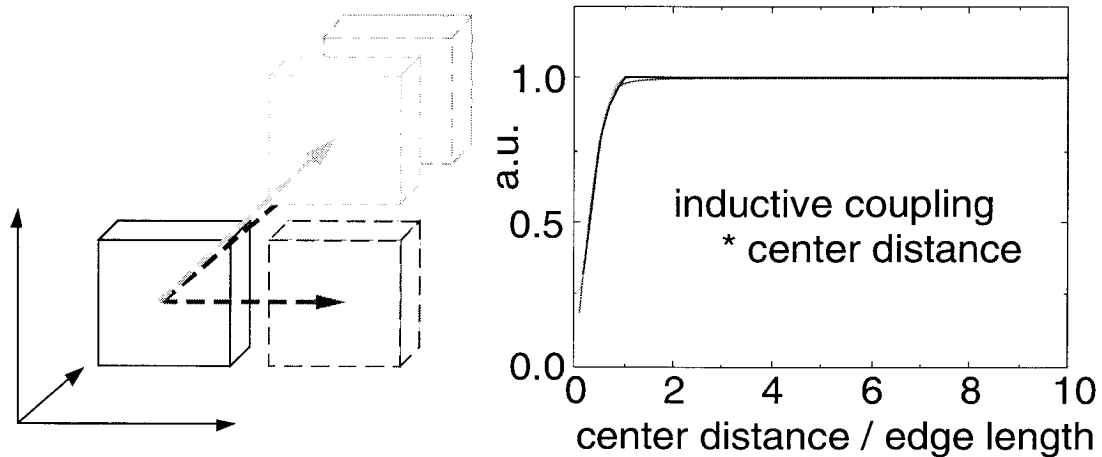


Figure 4.9: *Inductive coupling between cubes with homogeneous current density.*

elements with low current density. With these probability densities, current inhomogeneities do not lead to a spreading of samples. Samples Eq. (4.18) are, apart from the fact that they are positive or negative, only determined by the shape of the conductor geometry.

4.6.2 Probability Density 3

Another idea for importance sampling comes from the notion that the mutual inductance between cubes with constant current density decreases almost proportionally with their inverse center distance, as is shown in Fig. 4.9. Here, coupling inductances have been calculated with a formula similar to Eq. (B.2) which is taken from [35]. Obviously only one edge length distance between centers suffices in order to apply this center distance law and still obtain results with good accuracy. Furthermore, this relation for coupling inductances between cubes is independent of the direction of translation.

This behavior however cannot be included in Eq. (4.16) for $p_2(\mathbf{r}, \mathbf{r}')$ directly, because it does not factorize. When $p_2(\mathbf{r}, \mathbf{r}')$ does not factorize, the two locations required for computation of an energy sample Eq. (4.5) could not be selected independently, i.e. $p_2(\mathbf{r}, \mathbf{r}')$ would be different for each location \mathbf{r} . Initialization and storage of $p_2(\mathbf{r}, \mathbf{r}')$ would be as complicated as direct computation of the energy integral Eq. (2.57).

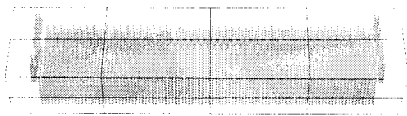


Figure 4.10: *Coil (Fig. 3.9) with “super grid” with $2 \times 2 \times 4$ elements superimposed.*

The problem is solved by use of a coarse “super grid” with constant grid spacing and number C cells and $C \ll \nu$, where ν again denotes the number of grid elements. An example of a “super grid” with $2 \times 2 \times 4$ cells is shown in Fig. 4.6.2 where it is superimposed on the coil conductor shown in Fig. 3.9. Each grid element is now associated with the nearest element of the “super grid”. The volumes of all structured grid elements associated with one “super grid”

element are added and the center of gravity \vec{r}_{ck} for each “super grid” element k is calculated. Below, all grid elements associated with the same “super grid” element are denoted by the term *block*. Finding the nearest “super grid” element for each grid element requires $\log C$ operation, because a binary search is used. Sorting all grid elements therefore requires $\nu \cdot \log C$ operations.

A new probability density is introduced, given by

$$p_l(c_{ij}) = \frac{V_{ci}V_{cj}}{|\vec{r}_{ci} - \vec{r}_{cj}|} \frac{1}{\sum_k \sum_l \frac{V_{ck}V_{cl}}{|\vec{r}_{ck} - \vec{r}_{cl}|}}, \quad (4.19)$$

where c_{ij} is the interaction between blocks i and j and V_{ci} denotes the sum of all volumes of grid elements belonging to block i . Entries $p_l(c_{ii})$ are initialized with the self inductance of a cube with volume V_{ci} . Implementation of p_l works similar to the algorithm explained in Sec. 4.4.1 and requires an array of length C^2 . The probability density for selecting two locations now becomes a product

$$p_2(\vec{r}, \vec{r}') = p_l(c_{ij})p_{2ij}(\vec{r}, \vec{r}') \quad (4.20)$$

with p_{2ij} the probability density for selection of locations from the pair blocks i and j . Note, that p_{2ij} again factorizes

$$p_{2ij}(\vec{r}, \vec{r}') = p_{1i}(\vec{r})p_{1j}(\vec{r}'),$$

and as in Eq. (4.10)

$$p_{1i}(\vec{r}) = p_{ie}(k)p_{kl}(\vec{r}). \quad (4.21)$$

Here, p_{ie} is the probability density for selecting one grid element from block i only. Note that implementation of all the p_{1i} requires in total only one array with length ν , the number of grid elements. The random number generated from p_l yields the block interaction and therefore the volume intervals, where to look for locations. Multiplication of Eq. (4.20) yields probability density 3 given in Tab. 4.3. Here, it looks like as if \vec{r}_c is the mapping of any location to the nearest center of gravity of “super grid” elements. Nevertheless every sample requires three random numbers for selecting two grid elements. One random number is needed for selecting the block interaction, two are needed for selecting two elements from the respective blocks.

The energy samples according to Eq. (4.5) are in this case given by

$$W_i \propto \frac{\vec{J}(\vec{R})\vec{J}(\vec{R}')}{|\vec{R}_i - \vec{R}_i'|} |\vec{r}_c(\vec{R}_i) - \vec{r}_c(\vec{R}_i')|. \quad (4.22)$$

With a fine “super grid”, i.e. a large C , the center of gravity of blocks is approximately the same as the actual location. In this case the conductor geometry does not alter samples in Eq. (4.22). Samples are only determined by current density values. However, due to the memory and time C^2 required for initialization of p_l a high number C is not feasible.

4.6.3 Probability Density 4

More improvement is gained from including also the current density as done in probability density 2. For stratification p_l is split into three probability densities p_{ls} with $s = x, y, z$, i.e. one for every coordinate direction

$$p_{ls}(c_{ij}) = \frac{\tilde{V}_{cis}\tilde{V}_{cjs}}{|\vec{r}_{ci} - \vec{r}_{cj}|} \cdot \frac{\tilde{V}_{cks}\tilde{V}_{cls}}{\sum_k \sum_l \frac{\tilde{V}_{cks}\tilde{V}_{cls}}{|\vec{r}_{ck} - \vec{r}_{cl}|}}. \quad (4.23)$$

In contrast to Eq. (4.19) the block interaction is weighted with

$$\tilde{V}_{cis} = \sum_{k \in ci} |J_{ks}| V_k,$$

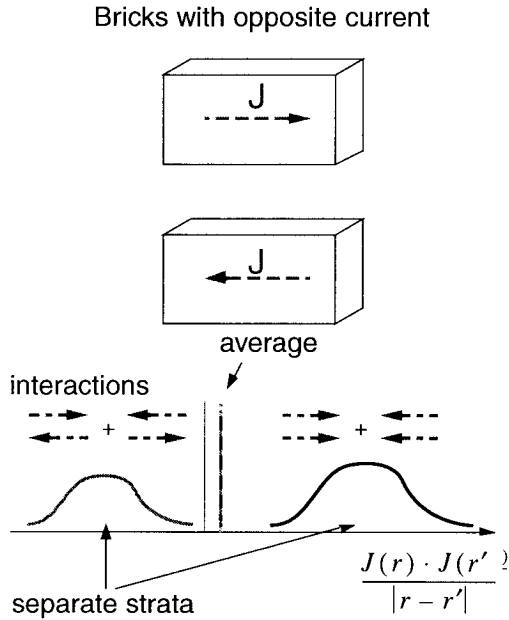


Figure 4.11: *Rectangular conductors with opposite current and corresponding distribution of energy samples Eq. (4.5).*

where J_{k_s} denotes component s of the current density in element k and V_k is the volume of grid element k . The probability density for selecting one grid element from elements associated with “super grid” element i only is set up as in Eqs. (4.16) and (4.21).

The samples according to Eq. (4.5) are in this case given by

$$W_i \propto \frac{\pm 1}{|\vec{R}_i - \vec{R}_i'|} |\vec{r}_c(\vec{R}_i) - \vec{r}_c(\vec{R}_i')|. \quad (4.24)$$

Except for positive and negative entries in case of a fine “super grid” all samples are almost constant.

4.6.4 Probability Density 5

Another idea for an improvement comes from the example shown in Fig. 4.11. Two cubes with reverse current yield two distant peaks in the distribution of samples in Eq. (4.2) with average somewhere in between. As an example consider both locations in the same cube. The current density now points in the same direction which results in a positive sample. When both locations are, by coincidence, in different cubes, the current densities point in opposite direction, which results in a negative sample. The variance of sampled values can be reduced by treating these two peaks separately. So Eq. (4.17) is separated once more into J_s^+ and

J_s^- terms, i.e positive and negative current density components. This increases the number of strata in Eq. (4.17) by a factor of 4.

For implementation the technique introduced for implementing probability density 4 in Sec. 4.6.3 is used. The samples according to Eq. (4.5) are in this case all positive.

$$W_i \propto \frac{1}{|\vec{R}_i - \vec{R}_i'|} |\vec{r}_c(\vec{R}_i) - \vec{r}_c(\vec{R}_i')| \quad (4.25)$$

With fine “super grid” resolution these samples become almost constant.

4.6.5 Computational Effort

Time and memory requirements for all investigated probability densities are listed in Tab. 4.2. Here, memory for storage of current density and geometry information is not mentioned. Additionally during every sample at least six random numbers are required for selecting two location inside the selected grid elements.

When calculating mutual inductances, probability densities sometimes have to be reinitialized. When using probability densities without consideration of current densities, only one setup at the beginning of the program is required. When current densities are considered, the one dimensional probability densities are initialized at program start. The probability densities for selection of stratum and “super grid” element interaction have then to be initialized for calculation of integral Eq. (4.2) separately.

4.7 Examples

In this section some examples are given in order to show the efficiency of the new algorithm. However – since all investigated methods are critically examined – also a rather difficult example is given in order to show its limits. The “super grid” is always constructed such that it contains roughly between 100 and 200 elements, all elements are cubes and its boundary almost matches the bounding box of the simulated conductor geometry.

Method	Memory	Random Numbers
no	ν	2
1	6ν	3
2	6ν	3
3	$C^2 + \nu$	3
4	$3C^2 + 6\nu$	4
5	$12C^2 + 12\nu$	4

Table 4.2: Time and memory requirements for all sampling methods. ν and C denote the number of grid elements and the number of “super grid” elements respectively. Memory indicates the length of probability density arrays Eq. (4.11). Here also a search array of same length is required. Random numbers indicate the number of random numbers and search processes required for selecting grid elements during every Monte Carlo sample Eq. 4.5. Listed random processes consist in selection of a stratum, selection of “super grid” element interaction and selection of elements.

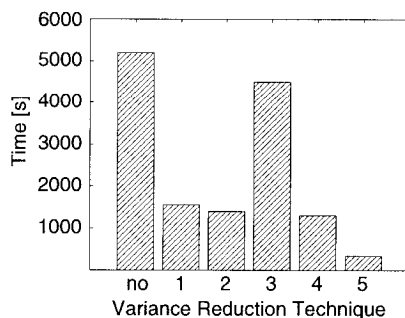


Figure 4.12: Time effort for computation of the full 16×16 inductance matrix (example Fig. 4.7.1 with variance reduction methods shown in Tab. 4.3).

Errors are given with the three sigma criterion Eq. (4.7). All simulations, current density computations and magnetic field energy estimate by means of the Monte Carlo method, have been performed on a 832M Sun Ultra 2 Model 2170 UltraSparc with 2x167 MHz.

4.7.1 DIP Package Lead Frame

Figure 4.7.1 shows the structured grid model of a DIP package lead frame and the electric potential after adaptive grid refinement respectively. Figure 4.12 shows the time effort for computation of the 16×16 inductance matrix with total 136 independent entries. Each entry was computed with 5% accuracy. For this example probability densities 1

Table 4.3: Tested probability densities for sampling of Eq. (2.57). p_s is the probability for selection of stratum s and p_{2s} is the probability density for selection of locations Eq. (4.13). $\vec{r}_c(\vec{r})$ is the function which maps locations to the nearest center of gravity of all elements associated with one element of the “super grid” Eq. (4.21).

variance reduction	no. of strata	p_s	$p_{2s}(\vec{r}, \vec{r}')$
no	1	1	$\frac{1}{V} \cdot \frac{1}{V}$
1	3	$\frac{1}{3}$	$\frac{ J_s(\vec{r}) \cdot J_s(\vec{r}') }{\int_V \int_V J_s(\vec{r}) \cdot J_s(\vec{r}') d^3r' d^3r}$
2	3	$\frac{\int_V \int_V J_s(\vec{r}) \cdot J_s(\vec{r}') d^3r' d^3r}{\sum_s \int_V \int_V J_s(\vec{r}) \cdot J_s(\vec{r}') d^3r' d^3r}$	$\frac{ J_s(\vec{r}) \cdot J_s(\vec{r}') }{\int_V \int_V J_s(\vec{r}) \cdot J_s(\vec{r}') d^3r' d^3r}$
3	1	1	$\frac{1}{ \vec{r}_c(\vec{r}) - \vec{r}_c(\vec{r}') } / \int_V \int_V \frac{1}{ \vec{r}_c(\vec{r}) - \vec{r}_c(\vec{r}') } d^3r' d^3r$
4	3	$\frac{\int_V \int_V J_s(\vec{r}) J_s(\vec{r}') / \vec{r}_c(\vec{r}) - \vec{r}_c(\vec{r}') d^3r' d^3r}{\sum_s \int_V \int_V J_s(\vec{r}) J_s(\vec{r}') / \vec{r}_c(\vec{r}) - \vec{r}_c(\vec{r}') d^3r' d^3r}$	$\frac{ J_s(\vec{r}) J_s(\vec{r}') / \vec{r}_c(\vec{r}) - \vec{r}_c(\vec{r}') }{\int_V \int_V J_s(\vec{r}) J_s(\vec{r}') / \vec{r}_c(\vec{r}) - \vec{r}_c(\vec{r}') d^3r' d^3r}$
5	12	$\frac{\int_V \int_V J_s^\pm(\vec{r}) J_s^\pm(\vec{r}') / \vec{r}_c^\pm(\vec{r}) - \vec{r}_c^\pm(\vec{r}') d^3r' d^3r}{\sum_{s\pm} \int_V \int_V J_s^\pm(\vec{r}) J_s^\pm(\vec{r}') / \vec{r}_c^\pm(\vec{r}) - \vec{r}_c^\pm(\vec{r}') d^3r' d^3r}$	$\frac{ J_s^\pm(\vec{r}) J_s^\pm(\vec{r}') / \vec{r}_c^\pm(\vec{r}) - \vec{r}_c^\pm(\vec{r}') }{\int_V \int_V J_s^\pm(\vec{r}) J_s^\pm(\vec{r}') / \vec{r}_c^\pm(\vec{r}) - \vec{r}_c^\pm(\vec{r}') d^3r' d^3r}$

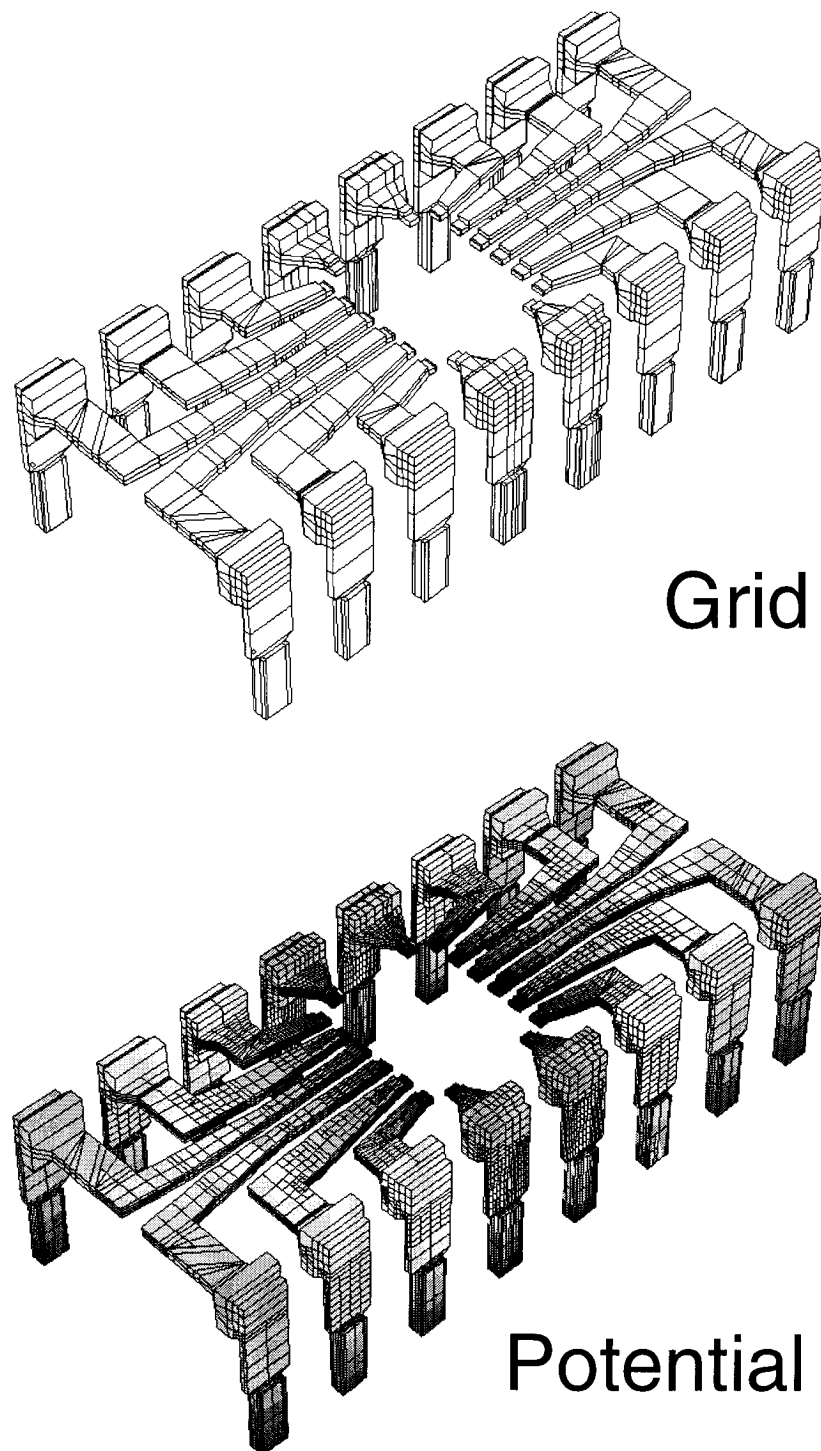


Figure 4.13: *Refined grid and scalar electric potential of DIP package lead frame which is shown in Fig. 1.1 with plastic casing included.*

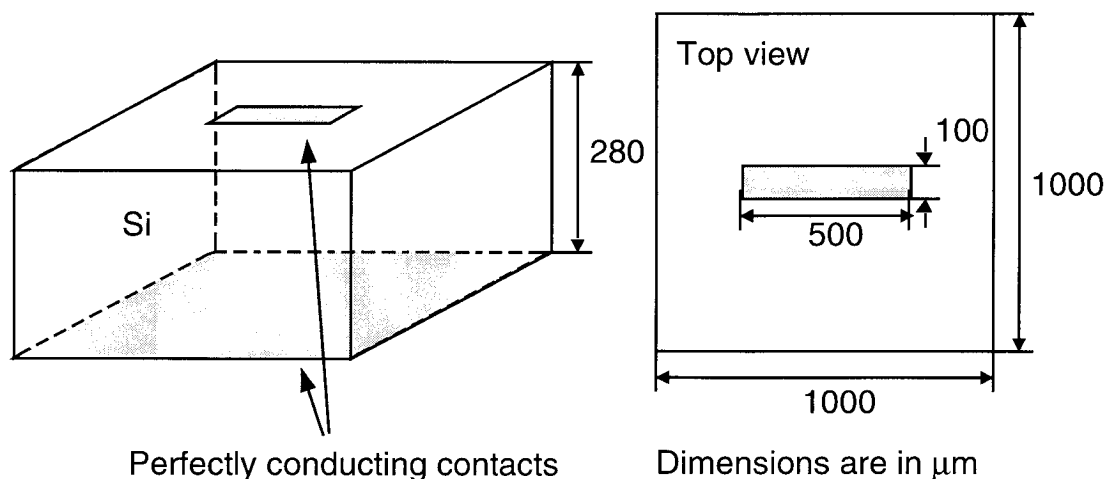


Figure 4.14: *Geometry of substrate.*

and 3 were slightly modified. In order to avoid “zero” samples, only grid elements with nonzero current were considered. Consideration of all grid elements would have led to a high number of samples with result 0 and hence a much higher variance and even slower convergence. The total speed up achieved by use of variance reduction techniques is 15.

Memory requirements have been about 100MB. The preceding 16 current density computations have taken 39mins including 3 adaptive grid refinement steps. Here, memory requirements have been approximately 80MB. Reasonable results could also have been obtained with less adaptive grid refinement steps, and therefore faster current density computations. Nevertheless, an estimate for the error introduced by these coarse current densities cannot be given without the refined grid results.

4.7.2 Substrate

Figure 4.14 shows the geometry of a p-doped Silicon block with ideal electric contacts at the top and at the bottom. The bulk conductivity is assumed to be $1.667 \cdot 10^4 \text{S/m}$, corresponding approximately to a doping concentration of $10^{19}/\text{cm}^3$.

Figure 4.15 shows three different grid models of the Silicon block shown in Fig. 4.14 with different grid resolution. With different grid models, the influence of grid refinement on the inductance result is studied.

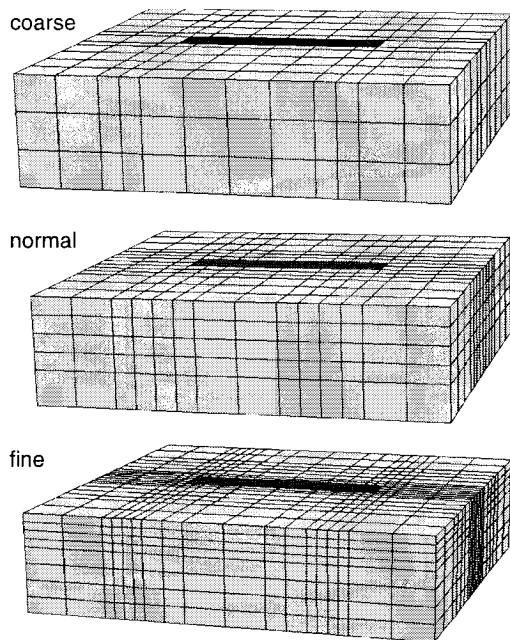


Figure 4.15: *Grid models of substrate shown in Fig. 4.14. Top: Coarse resolution. Center: Medium resolution. Bottom: Fine resolution.*

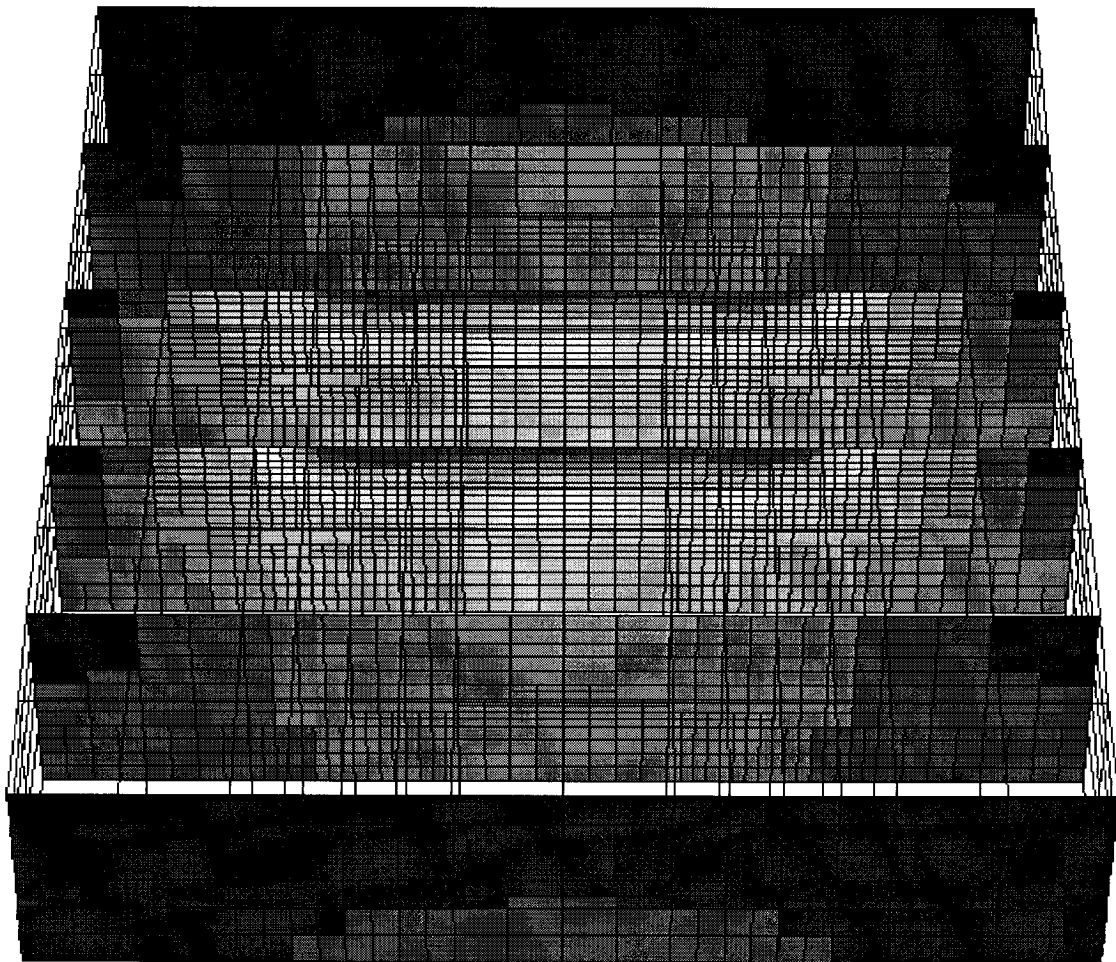


Figure 4.16: *Cuts through substrate from Fig. 4.14 with current density on adaptively refined grid.*

Grid	DoF	Memory	Time	R [Ω]	L [H]
coarse	624	3 MB	8 s	$6.67 \cdot 10^{-2}$	$2.96 \cdot 10^{-11}$
normal	1350	3 MB	10 s	$7.09 \cdot 10^{-2}$	$3.03 \cdot 10^{-11}$
fine	3591	15 MB	22 s	$7.65 \cdot 10^{-2}$	$3.05 \cdot 10^{-11}$
adaptive	23064	71 MB	338 s	$7.91 \cdot 10^{-2}$	$3.11 \cdot 10^{-11}$

Table 4.4: Time and memory requirements for current density simulations for grid models shown in Fig. 4.15. DoF denotes the number of degrees of freedom for computation of the electric scalar potential. The adaptive grid has been generated from the coarse grid model by performing four adaptive grid refinement steps. The given time and memory requirements include all refinement steps.

Figure 4.16 shows the result of a current density simulation after 4 adaptive grid refinement steps. The highest amplitude of the current density occurs at the top contact. Current then spreads towards the bottom contact (Fig. 4.14).

Table 4.4 shows the computational effort for simulation of the current density distribution. In case of the adaptively refined grid, the Monte Carlo algorithm required 13MB total memory and 7s for obtaining an inductance result with 1% accuracy when variance reduction from Sec. 4.6.4 was used. With respect to no variance reduction, the variance was reduced by a factor of 50, which resulted in speed up by the same factor. With variance reduction applied, inductance results always were obtained from approximately 40000 energy samples.

4.7.3 Meander and Coil

In this section the same conductor geometries as in the previous chapter are investigated (c.f. Fig. 3.9). In case of the meander geometry, computation of the current density took around 5s, since only 6064 degrees of freedom were used for modeling the scalar electric potential. Variance reduction with probability density in Sec. 4.6.4 reduced the number of samples by a factor of 7 when results with same accuracy are computed. In case of the coil geometry, computation of the current density took 25s with 13984 degrees of freedom. Variance reduction with probability density in Sec. 4.6.4 reduced the number of samples by a factor of 15 when results with same accuracy are computed.

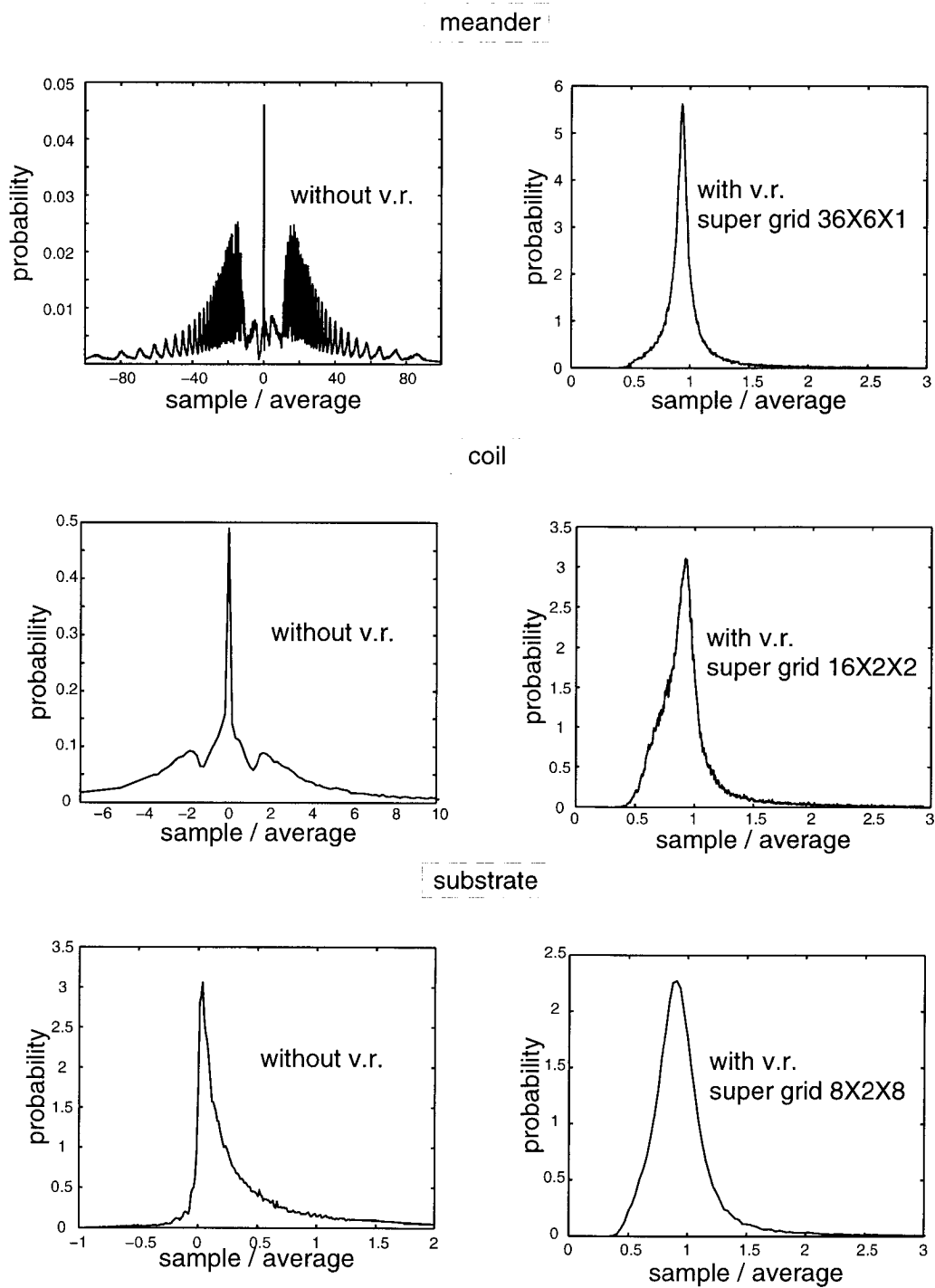


Figure 4.17: *Distribution of samples Eq. 4.5 with and without use of variance reduction technique.*

Grid	DoF	Time	R [Ω]	L [H]
Meander	6064	3950 s	$7.53 \cdot 10^1$	$8.04 \cdot 10^{-11}$
Coil	13984	45 s	$3.01 \cdot 10^2$	$4.05 \cdot 10^{-9}$

Table 4.5: *DoF* denotes the number of degrees of freedom for modeling the electric scalar potential. *Time* denotes the time spent for Monte Carlo sampling in order to achieve an error below 1% according to the three sigma criterion Eq. (4.7). *R* and *L* are the results.

4.7.4 Further Analysis

This section presents a further analysis of the effect of variance reduction on energy samples Eq. (4.5). Figure 4.17 shows histograms of sampled values for the previously discussed geometries. All curves are scaled such that the area below equals one. Histograms therefore correspond to a probability density of obtaining a certain sampled value. The x-axis is also scaled such that the average sampled value corresponds to $x = 1$. Histograms without variance reduction have been generated from samples obtained with Eq. (4.5) with constant probability density $p_2(\mathbf{r}, \mathbf{r}')$. Histograms displaying distributions of samples with variance reduction technique have been generated from samples obtained with Eq. (4.25).

Histograms of meander and coil conductor without variance reduction clearly exhibit the behavior shown in Fig. 4.11, where two peaks have been expected for alternating current densities. The center peak stems from samples, where current densities are orthogonal. The oscillating distribution of samples of the meander structure also reflects the gaps between turns of the conductor. In case of the substrate example, zero samples do not occur, because the geometry is not bent and therefore one component of the current density with direction from one contact to the opposite is always non zero. The average of sampled values is in all cases removed from the maximum, which leads to slow convergence as has been mentioned in Sec. 4.3. The broadest distribution of samples comes from the meander geometry, which also most resembles a two dimensional conductor.

Use of all proposed variance reduction techniques leads to a completely different distribution of samples. Here, all distributions look almost

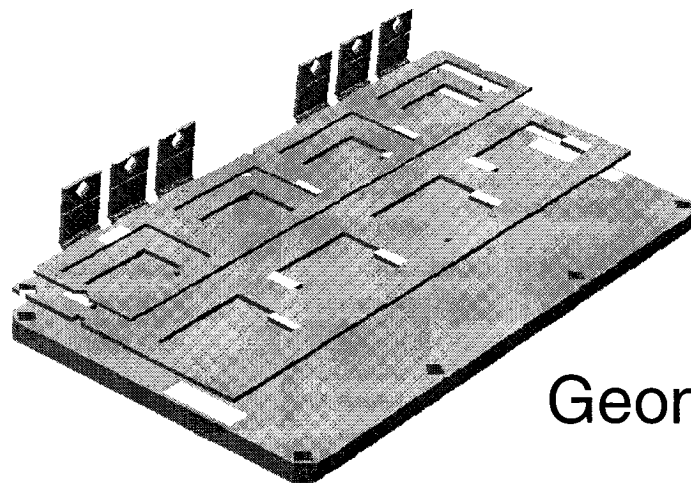
equal. Hence, all geometry and current density information seems to be compensated by the coarse “super grid” and current density information put into the probability density. Their maximum almost matches the average. This means that the most probable sampled value already is the average and convergence is obtained quickly.

One question remains: Why is convergence in case of the meander structure slow, despite the fact that the probability density quite efficiently maps the samples towards unity? The reason is the difference between two large numbers. Calculation of only the positive contributions in Eq. (4.12) yields an inductance of $1.2 \cdot 10^{-8} \text{H}$. The negative contributions are equivalent to an inductance $-1.192 \cdot 10^{-8} \text{H}$, which almost corresponds to the positive contribution due to the strong inductive coupling between conductor branches. Both values are calculated efficiently, but the error Eq. (4.15) is amplified when divided by the small average.

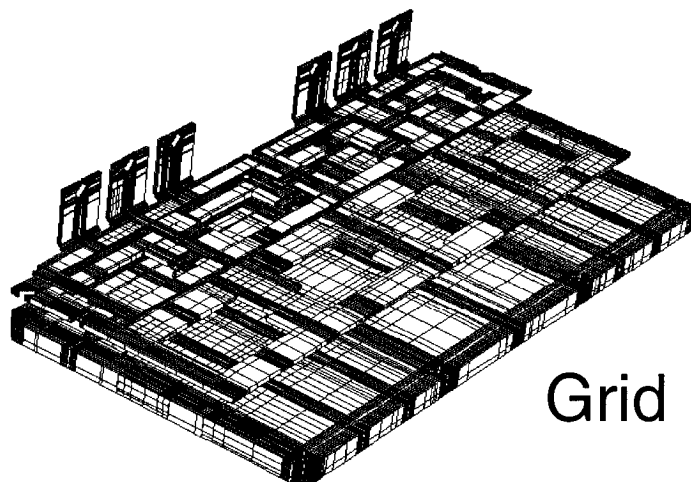
4.7.5 IGBT Bus Bar

Figure 4.18 shows another example which has already been shown in Fig. 1.1. Due to the number of electric contacts and their positions, resistive and inductive behavior can be characterized with 18×18 resistance and inductance matrices. The electric potential shown on the right has been calculated after one grid refinement step, where different EMF's have been applied to different ports. This grid refinement procedure assures an almost optimal grid for any port current distribution, which is realized during the subsequent magnetic field energy estimates. Hence, all current density distributions are modeled on the same grid. For this example, the scalar electric potential was modeled with 83484 degrees of freedom. Time and memory requirement including one grid refinement step for computations of all 18 current density distributions was 47min and 452MB respectively.

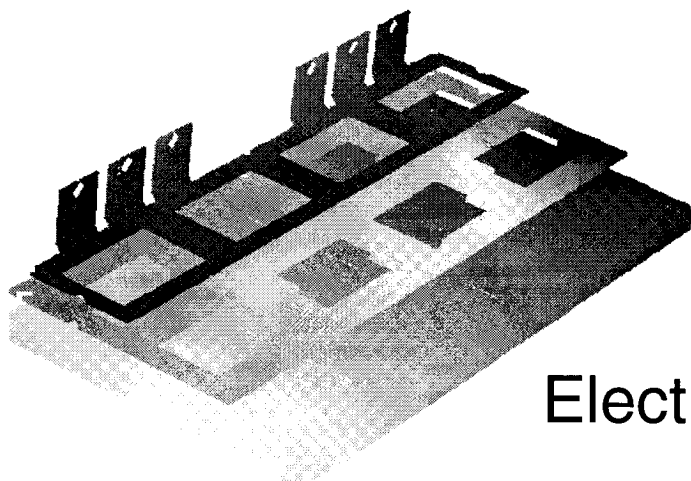
Subsequent magnetic field energy estimates of all $1/2 \cdot 18(18 + 1) = 171$ energy terms in Eq. (4.2) took 49min and required 280MB of memory. This relatively high amount of memory is required due to the fact, that all current density distributions are loaded at the same time in order to switch current density distributions rapidly. The maximum number of samples per energy estimate was limited to 500000. This value assured a relative error less than 1% for more than half of all energy terms. Errors



Geometry



Grid



Electric Potential

Figure 4.18: *Top: Model of IGBT busbar as shown in Fig. 1.1. Electrical contacts are marked with white color. Inductive and resistive behavior is described with 18 conductor ports. Center: Tensor grid. Bottom: Electric potential simulated for grid refinement.*

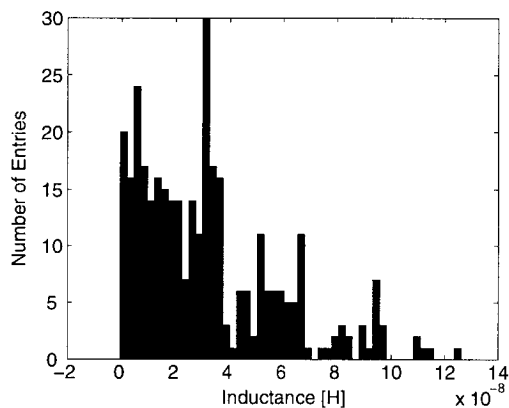


Figure 4.19: *Entries in inductance matrix of IGBT busbar shown in Fig. 4.18.*

of the rest are in the range 1% - 3%.

The resulting inductance matrix reveals a highly complex system. A histogram of all entries in the inductance matrix – self and mutual inductances – is shown in Fig. 4.19. It is not clear, if and how the complexity can be reduced. It is therefore believed that inductive port behavior as described in [4] probably comes from the interaction of all present inductors and inductive couplings.

4.8 Conclusions

Because of several limitations of the FEM as presented in the previous chapter, a new method for static inductance extraction based on current density simulations by means of FEM and subsequent magnetic field energy estimate by means of the Monte Carlo method has been developed. Memory requirements of the new method are considerable lower, since only the current density distribution inside conductors is computed by means of FEM. Furthermore, an absolute error estimate can be given which makes the method suitable for industrial applications. The new method is self adjusting, i.e. the number of Monte Carlo samples necessary for obtaining a result with predefined accuracy is determined automatically. The memory requirement for sampling grows only linearly with the number of grid elements. The time requirement for performing one sample is independent of the number of grid elements. Monte Carlo sampling could be highly accelerated by use of different variance reduction techniques. Convergence has been analyzed in detail for basic classes of geometries and for examples given in the previous

chapter. Results can be used to estimate convergence and efficiency for any conductor geometry. Finally a larger example has been presented, which could not have been simulated with the previously presented FEM program.

Related Approaches

This chapter has been written in order to put the newly developed static inductance extraction method into the context of other approaches. Other approaches for numerical static inductance extraction are reviewed and extensions towards inductance extraction under the quasistatic approximation are discussed. Since equations for capacitance extraction are similar, these methods are reviewed, too. Two kinds of numerical methods are discussed – Monte Carlo methods and hierarchical methods. Due to the fact that the other Monte Carlo program was not available for testing, it is compared on a theoretical basis. Respective advantages and disadvantages are given and possible extensions are discussed.

5.1 Capacitance Extraction by Means of the Monte Carlo Method

This section discusses capacitance extraction by means of a floating random walk algorithm (QuickCapTM algorithm [55]). It is based on a floating random walk algorithm for electric potential computation [56, 57]. Monte Carlo methods are attractive, since memory requirements are low. This special algorithm moreover does not require any meshing of the geometry.

The QuickCapTM algorithm is sketched in Fig. 5.1. Before the algorithm starts, electric field and electric potential in the center of a square (cube in 3D) are tabulated for all combinations of electric potential on its boundary (left of Fig. 5.1). Boundary potentials are prescribed on discrete points. The potential on the boundary is interpolated linearly

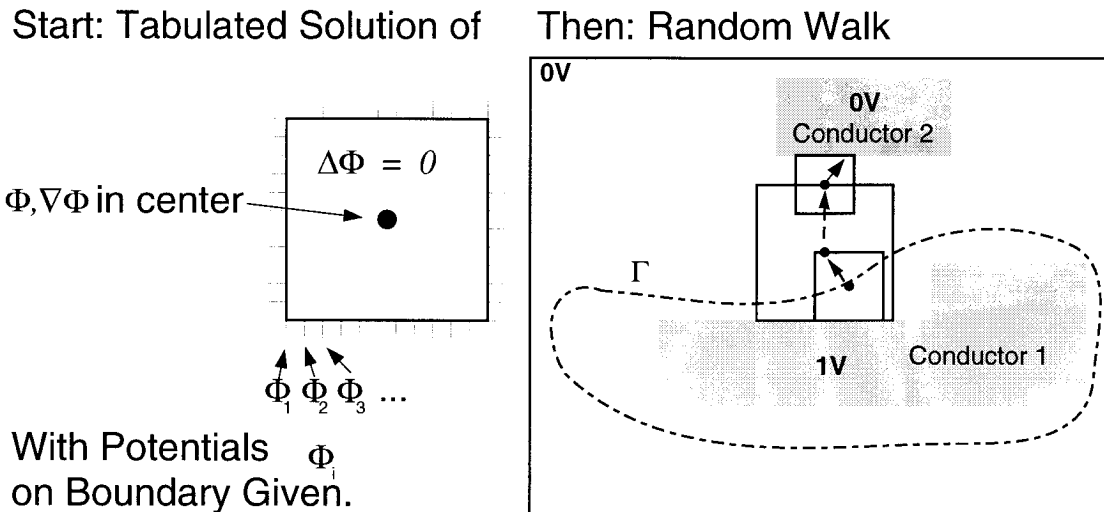


Figure 5.1: Idea of QuickCapTM [55] capacitance extraction algorithm. Left: Electric potential and electric field in the center of a square are tabulated for all combinations of electric potential values on its boundary. Right: Floating random walk of squares between conductors and domain boundary.

between those points. It can be shown that the center potential is independent of the square size, i.e. the center potential stays constant once boundary potentials remain unchanged and the edges are scaled by a factor λ . The derivative of the center potential however changes $\nabla\Phi \rightarrow 1/\lambda\Phi$. The center potential depends linearly on the boundary potential values, because the Poisson equation is linear. Hence, only the relation between each single boundary potential value and the center potential has to be tabulated.

During the Monte Carlo procedure the capacitances are extracted with Eq. (2.31). The electric field flux through a surface Γ around conductors is determined from single electric field values on Γ . These are computed by placing squares with center on Γ and maximum size, such that they do not intersect with conductors. The electric field in the center of squares and hence the electric field flux through Γ is determined from the potential on the boundary of squares. The potential is directly available where squares hit conductors. When the potential is not available, another square with maximum size and center where the potential is to be determined is placed between conductors. This algorithm results in

a large number of squares, which have to be placed between conductors in the described recursive manner. Now, instead of evaluating the potential whenever required, for every square only one location on the boundary is selected in a random manner. The resulting center electric field or electric potential is scaled up according to the surface of the square. This random selection and scaling results in the *random walk* of squares between conductors, which is shown on the right in Fig. 5.1. Each random walk stops, once a random location either hits a conductor or the domain boundary, where the electric potential is known. Efficiency stems from the fact, that due to scaling of the size of squares empty space between conductors is abridged rapidly. The distance between conductors and the outer boundary of the simulation domain therefore can be large without loss of performance. Note, that random walks do not have to be carried out again when the conductor potentials change. Results of random walks can be stored separately for every conductor which is finally hit. Respective conductor potentials can be inserted afterwards. Hence, the complete capacitance matrix can be evaluated with only one set of random walks. Treatment of dielectric materials is shown in [58].

5.1.1 Convergence

It is often reported by users that the algorithm is slow for conductor geometries with high aspect ratio, i.e. long and thin conductors. The authors of QuickCapTM claim in [55] that their algorithm is suitable for all kinds of geometries. Here, it is explained why convergence is slow in some cases and why QuickCapTM is best suited for rectilinear geometries. During this work the program was not available for testing. Therefore the algorithm is evaluated on a theoretical basis.

To the author's knowledge distribution of samples like in Sec. 4.7.4 has not been investigated for this method. However, it can be assumed that strong inhomogeneities of the electric flux distribution on the flux-surface lead to slow convergence as in the case of the newly developed static inductance extraction method. A few flux samples already lead to flux estimates with high confidence when the flux distribution is homogeneous. A parallel plate capacitor is an example with homogeneous flux distribution and two vertically aligned rectangular conductors is an example with inhomogeneous flux distribution.

Convergence is also determined by the number of steps required during

each random walk. A random walk stops when the potential on a random location on the square surface is known, i.e. when a conductor is hit. This can occur right in the beginning when the random location on the surface of the initial floating square lies on a conductor surface. Termination of a random walk is very likely, when a floating square is almost covered by conductors. It is very unlikely, when only a small part of a floating square is covered by conductors as in the case of very small and narrow conductors with large space between, where floating random walk squares become large. This is probably the strongest reason for slow convergence in case of conductor geometries with high aspect ratio. Convergence is also slow, when non rectilinear geometries are treated. These are represented by sets of small rectilinear conductors, i.e. diagonal conductor surfaces are approximated by staircase functions. Here, expansion of floating random walk squares is hindered by only small parts of conductor surfaces. Consequently it is unlikely that the potential at a random location on a floating square surface is known. The average number of random walk steps therefore will be considerably higher than in case of non rectilinear conductor geometries.

5.1.2 Inductance Extraction with Floating Random Walk

The floating random walk algorithm has already been extended towards inductance extraction [59]. The authors presented a two dimensional transmission line example where the inductance is determined by evaluation of the magnetic flux between two conductors. Surface current densities \mathbf{K} are prescribed by means of a current boundary condition for the magnetic vector potential on the conductor – dielectric interface [33]

$$\frac{1}{\mu}(\nabla \times \mathbf{A}(\mathbf{r})) \times \mathbf{n} = \mathbf{K}. \quad (5.1)$$

The boundary condition Eq. (3.4) used in Finite Element analysis correspondingly represents a surface without any surface currents. Assuming a pure surface current density and no current inside conductors means that the interior of a conductor is field free. This corresponds to a skin-depth much smaller than the diameter of a conductor and occurs in the high frequency case of the quasistatic approximation. Flux computation now works exactly like the capacitance extraction algorithm. However instead of tabulating $\nabla \mathbf{A}$ in the center of a square, here $\nabla \times \mathbf{A}$ is stored

for all combinations of boundary magnetic vector potential values. Random walks start at the surface where the flux is to be computed and they end either at the conductor surface or at the outer boundary (with no surface current density defined).

Both the newly developed static inductance extraction algorithm and the modification of QuickCapTM do not compute the current density. The newly developed algorithm (Chap. 4) could be applied to pure surface current densities in two dimensions as well. Here, the Green function Eq. (2.15) would have to be changed, i.e. $1/|\mathbf{r} - \mathbf{r}'| \rightarrow \ln|\mathbf{r} - \mathbf{r}'|$. Since Finite Element methods are quite efficient for two dimensional inductance extraction, this modification however has not been investigated. Since the random walk algorithm was not available for evaluation, it is compared with the newly developed method on a theoretical basis.

- The floating random walk algorithm uses a random walk for evaluation of the magnetic vector potential derivative whereas the newly developed algorithm evaluates magnetic vector potential samples directly.
- The newly developed algorithm deploys variance reduction techniques for accelerated convergence, whereas the floating random walk algorithm does not apply any variance reduction techniques.
- Convergence of the floating random walk algorithm is slow for non rectilinear conductor geometries.
- a flux surface is required by the random walk algorithm whereas the newly developed method uses only the current density distribution.
- The floating random walk algorithm cannot easily be extended towards inductance extraction of volume current distributions whereas the newly developed technique can be extended towards inductance extraction of arbitrary two- or three dimensional current densities distributions – almost without any modifications.

5.1.3 Current Density Computation

This section discusses the possibility of extending the floating random walk algorithm towards the computation of the current density. As it is more easy to compute a static current distribution than to compute a

current density with the quasistatic approximation including the skin effect, only computation of a static current distribution is discussed. Since the capacitance matrix Sec. 2.5.2 and the resistance matrix Sec. 2.5.6 have the same properties, the floating random walk algorithm can be applied both for computation of electric field flux and current density flux through boundaries inside conductors. However, in case of current density computations, floating random walks are handicapped by conductor walls which cannot be traversed. Therefore situations can occur, e.g. in long and thin conductors, where a random walk does reach the opposite contact and commutes between conductor walls instead. Another difficulty arises from the conductor walls, where $\mathbf{J}(\mathbf{r}) \cdot \mathbf{n}(\mathbf{r}) = 0$ with $\mathbf{n}(\mathbf{r})$ the normal on the conductor walls. The potential in the center of the floating square and its derivative here not only depend on the square's surface potentials, but also on the respective boundary conditions. Hence, current density computation with the floating random walk does not seem feasible.

5.2 Method of Moments

In electromagnetics the **Method of Moments** (MoM) is often associated with Harrington's method [60, 61]. It can be used for capacitance extraction, where the integral equation Eq. (2.27) is solved numerically. Only the surface of conductors has to be discretized, because the inner of conductors is field free. The surface charge density then becomes

$$\sigma(\mathbf{r}) = \sum \sigma_i f_i(\mathbf{r}), \quad (5.2)$$

with

$$f_i(\mathbf{r}) = \begin{cases} 1 & \text{when } \mathbf{r} \in \Delta S_i \\ 0 & \text{otherwise} \end{cases} \quad (5.3)$$

and ΔS_i the surface elements. Discretization leads to a matrix equation

$$\underline{\mathbf{A}}\mathbf{q} = \Phi, \quad (5.4)$$

where \mathbf{q} is the vector of total charges on surface elements, Φ is the vector of electric potential in the center of surface charge elements and $\underline{\mathbf{A}}$ is a dense matrix with entries

$$A_{ij} = \frac{1}{4\pi\epsilon} \frac{1}{|\Delta S_i|} \int_{\Delta S_i} \frac{1}{|\mathbf{r} - \mathbf{r}_{jc}|} d^2 r \quad (5.5)$$

with $|\Delta S_i|$ the size of surface element ΔS_i and \mathbf{r}_{cj} the center of ΔS_j . Diagonal entries are calculated with functions in [35] or approximates. Full matrix assembly requires $O(n^2)$ operations and solution for a given surface potential requires $O(n^3)$ operation with n the number of surface elements. This is not feasible for large values of n . Solution can be accelerated with use of iterative solver routines D [29, 62]. Here, the solution becomes

$$\mathbf{q}_{i+1} = D(\underline{\mathbf{A}}\mathbf{q}_i, \underline{\mathbf{A}}\mathbf{q}_{i-1}, \dots, \underline{\mathbf{A}}\mathbf{q}_0, \mathbf{q}_0). \quad (5.6)$$

In Eq. (5.6) \mathbf{q}_i denotes the i -th approximation of the solution. Note that D only requires the result of a matrix vector product $\underline{\mathbf{A}}\mathbf{q}$ for generation of a new approximate solution. Evaluation of this matrix vector product corresponds to the evaluation of the vector of electric potential Φ for a given charge distribution. Each matrix vector product requires $O(n^2)$ operations. When the matrix $\underline{\mathbf{A}}$ is well conditioned, typically much less than n solver iterations are required in order to compute \mathbf{q} with sufficient accuracy. With k the number of solver iterations and $k \ll n$, in total only $O(k \cdot n^2) < O(n^3)$ operations are required. Despite of this acceleration, still $O(n^2)$ memory is required for matrix storage. This amount can be reduced with hierarchical expansions, where the first algorithm was developed by Barnes and Hut [63] originally intended for force evaluation in N-body simulations. Here, surface elements are clustered and interactions Eq. (5.5) between elements from different clusters are assumed constant, when the distance between clusters is large compared to their size. Clusters are treated as pseudo surface elements. These are arranged within clusters on a higher level. When the distance between these clusters is large compared to their size, interaction between pseudo surface elements from different clusters is assumed constant and so on.

Note that this algorithm can be used for sorting surface elements in space. When the potential is known, also its derivative is known. The derivative corresponds to the force. Translation of surface elements according to the force will spread all surface elements according to their relative position and hence sort the surface elements. From theoretical computer science it is known that sorting elements without any prior knowledge of their positions cannot be done with less than $O(n \log n)$ operations. This minimum number of operations therefore forms a lower limit for accelerating the calculating of the matrix vector product $\underline{\mathbf{A}}\mathbf{q}$. The Barnes and Hut algorithm actually treats clusters as monopoles. Larger clusters with the same accuracy can be formed, when higher mo-

- Source Locations
- Evaluation Points

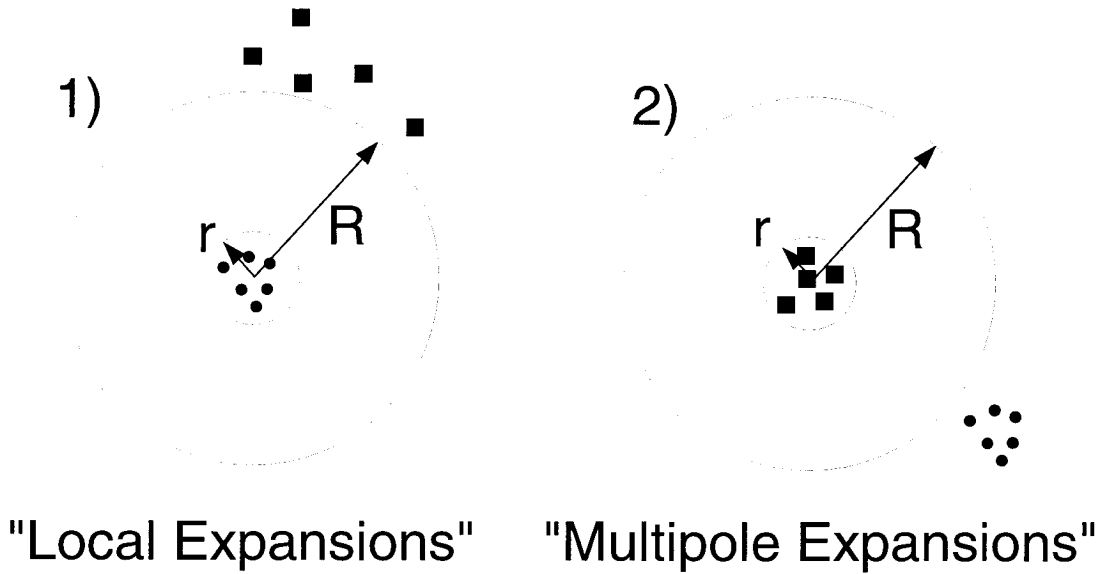


Figure 5.2: *Multipole and local expansion.*

ments of the electric potential outside clusters are considered, too. These are considered by the Greengard algorithm [64]. The expansion of potentials is sketched in Fig. 5.2. Two kinds of expansions with coefficients M_n^m and L_n^m exist. The multipole expansion is used for evaluation of the potential outside a sphere due to charges inside the sphere

$$\Phi(r, \theta, \phi) = \sum_{n=0}^l \sum_{m=-n}^n \frac{M_n^m}{r^{n+1}} Y_n^m(\theta, \phi). \quad (5.7)$$

The local expansion is used for evaluation of the electric potential inside a sphere due to charges outside a sphere

$$\Phi(r, \theta, \phi) = \sum_{n=0}^l \sum_{m=-n}^n L_n^m r^n Y_n^m(\theta, \phi). \quad (5.8)$$

In Eqs. (5.7) and (5.8) the $Y_n^m(r, \theta, \phi)$ denote the spherical harmonic functions.

One expansion can be transformed into the other. It can be shown that the error δ introduced by a truncated expansion with order l is smaller

than

$$\delta < K_1 \left(\frac{r}{R} \right)^{l+1} \quad (5.9)$$

in case of the multipole expansion Eq. (5.7) and smaller than

$$\delta < K_2 \left(\frac{r}{R} \right)^{l+1} \quad (5.10)$$

in case of the local expansion, K_1 and K_2 being some constants and r , R the radii shown in Fig. 5.2. A very important feature of multipole and local expansions is the conservation of errors. Once a multipole expansion is constructed for the area outside a sphere with radius R and this expansion is transformed into another expansion with same order l , the errors Eq. (5.9) and Eq. (5.10) still apply for the region outside the sphere with radius R . The relative error introduced by the use of expansions is typically smaller than $1 \cdot 10^{-3}$. The resulting approximate representation $\tilde{\mathbf{A}}$ of the dense matrix in Eq. (5.4) is therefore

$$\tilde{\mathbf{A}} = \left\{ \mathbf{1} + \begin{pmatrix} \Delta_{11} & \cdots & \Delta_{1\nu} \\ \vdots & \ddots & \vdots \\ \Delta_{\nu 1} & \cdots & \Delta_{\nu\nu} \end{pmatrix} \right\} \mathbf{A}, \quad (5.11)$$

with $\mathbf{1}$ the unity matrix and $|\Delta_{ij}| < 10^{-3} \quad \forall i, j$.

Variants of the algorithm include [65, 66]. Below, the algorithm is compared with the newly developed Monte Carlo sampling method. The implementation of the program used for benchmarking is described in [67]. The key for implementation is the trade-off between calculating the matrix entries Eq. (5.5) directly or doing the more complicated expansions. In any case interactions between near panels are calculated directly. Therefore only the near interactions are available for a preconditioning of the matrix.

Other approaches for reducing the complexity of the matrix vector product include:

- Use of the **F**ast **F**ourier **T**ransformation (FFT) [68, 69]. Equation (2.27) is a convolution of the charge density with the Green function Eq. (2.26). Fourier transforming the Green function and the charge density allows the electric potential to be computed with

a multiplication and back transformation with another FFT. Before Fourier transformations are being carried out, charges have to be mapped onto a grid. Interactions between near surface elements are calculated directly. This algorithm is inspired by algorithms originally developed for plasma simulations by means of the particle in cell method [70]. As only the result of a matrix–vector product is available, preconditioning of the matrix is not possible. The main disadvantage of the algorithm is the required grid for the FFT. This makes the algorithm less attractive for a calculation of a capacitive coupling between distant conductors.

- Sparsification of the matrix in Eq. (5.4) directly with use of the single value decomposition technique [71, 72]. Single value decomposition is applied in a hierarchical manner yielding a sparse matrix representation with controlled error of the matrix vector product results. This sparsification technique allows the use of matrix preconditioners for accelerated convergence of iterative matrix equation solver routines Eq. (5.6).

Surface elements can be understood as single capacitors. Due to shielding of capacitances as described in Sec. 2.5.2, far range interactions in Eq. (5.4) can be left out. A sparse approximation of the inverse of the resulting sparse matrix can be constructed with algorithms from [73, 74]. This algorithm however only yields self capacitances. The more interesting coupling capacitances required for construction of an equivalent circuit Sec. 2.9.1 cannot be calculated from this sparse representation of Eq. (5.4).

It shall be noted that due to the properties of the capacitance matrix Sec. 2.5.2 self consistent iterations cannot be used for simulating the charge density for a given electric contact potential. A self consistent iteration scheme could be transformed into a Markov process [53] and Monte Carlo methods could be used for solution.

5.3 PEEC Method

This section explains the **p**artial **e**lement **e**quivalent **c**ircuit (PEEC) method [31] for simulation of current density distributions with the quasi-static approximation Sec. 2.5. In case of the PEEC method, conductor

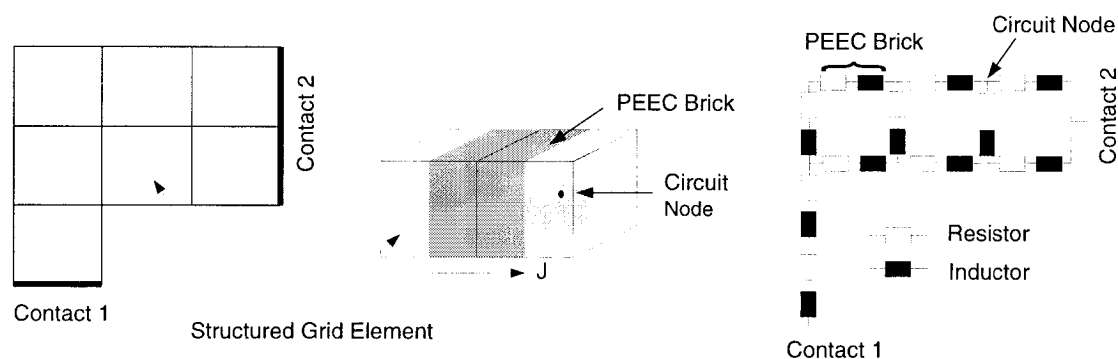


Figure 5.3: *Generation of a PEEC model: structured grid model of a conductor with two contacts (left), placement of PEEC bricks into structured grid elements (middle), complete equivalent circuit (right).*

geometries are discretized and interactions between discrete elements are evaluated similar to Eq. (5.5).

The PEEC method was originally developed for translation of arbitrary three-dimensional conductor geometries into circuit models, which can then be simulated with common circuit simulator programs like SPICE [15]. The idea behind PEEC is to subdivide the geometry into elements with known electrical behavior, in this case bricks with constant current density. The skin effect can be simulated properly, when the skin depth Eq. (2.74) is large compared to the diameter of the PEEC bricks. Calculation of resistance, inductance and inductive coupling of bricks already has been explained in Sec. 2.8.1. The elements are electrically connected according to neighborhood. All circuit elements are electrically characterized by a resistor and an inductor connected in series. For simulation also inductive couplings are included in the circuit analysis.

Construction of PEEC models from a geometry given in structured grid format is shown in Fig. 5.3. The left part shows contours of structured grid elements. The middle part shows how the PEEC bricks with known electrical behavior are placed into the structured grid, namely between centers of adjacent structured grid elements. The direction of the current density \vec{J} is predefined from one center to the other. Note, that these bricks do in fact overlap when a structured grid element has neighbors in different coordinate directions. The right part shows the complete PEEC model. As stated before, every brick is electrically characterized by a resistor and an inductor connected in series. Nodes representing

the same contact are set to the same electric potential.

Overlapping PEEC bricks have to be aligned rectangularly. When overlapping PEEC bricks are not aligned rectangularly, the ohmic power loss $P(\mathbf{r})$ Eq. (2.58) is not simulated correctly

$$\begin{aligned} P(\mathbf{r}) &\propto (\mathbf{J}_1(\mathbf{r}) + \mathbf{J}_2(\mathbf{r})) \cdot (\mathbf{J}_1(\mathbf{r}) + \mathbf{J}_2(\mathbf{r})) \\ &= \mathbf{J}_1(\mathbf{r}) \cdot \mathbf{J}_1(\mathbf{r}) + 2\mathbf{J}_1(\mathbf{r}) \cdot \mathbf{J}_2(\mathbf{r}) + \mathbf{J}_2(\mathbf{r}) \cdot \mathbf{J}_2(\mathbf{r}) \\ &= \mathbf{J}_1(\mathbf{r}) \cdot \mathbf{J}_1(\mathbf{r}) + \mathbf{J}_2(\mathbf{r}) \cdot \mathbf{J}_2(\mathbf{r}), \quad \text{when } \mathbf{J}_1(\mathbf{r}) \perp \mathbf{J}_2(\mathbf{r}), \end{aligned} \quad (5.12)$$

$\mathbf{J}_1(\mathbf{r})$ and $\mathbf{J}_2(\mathbf{r})$ being the constant current densities in two overlapping PEEC bricks.

Treatment of all coupling inductances makes the use of ordinary circuit simulators prohibitive for circuits with many PEEC bricks.

An alternative to volume discretization and therefore considerable saving of unknowns in the high frequency case is the “surface ribbon method” [75]. Due to a small skin depth Eq. (2.74) the current distribution is almost limited to the surface of conductors. Hence only the surface of conductors has to be discretized and appropriate expansion functions have to be used. This approach however does not yield correct inductance values when the skin depth is large compared to the conductor diameters.

The evaluation of induced voltages due to changing currents Eq. (2.28) is the same problem as the evaluation of the electric potential for a given charge distribution Eq. (2.17). However unlike as in the capacitance extraction case Sec. 5.2, due to the properties of the inductance matrix Sec. 2.5.4, far range interactions cannot be left out of the analysis.

The PEEC simulation program FastHenry [76] makes use of this similarity between capacitance extraction by means of the moment method and the evaluation of induced voltages due to alternating currents. It uses the previously described multipole algorithm and its implementation [67] for evaluating the induced voltages for each coordinate direction separately. FastHenry uses the full volume discretization with bricks as shown in Fig. 5.3. The equation of continuity Eq. (2.47) is fulfilled by solving the corresponding circuit equations. Here the Kirchhoff voltage law is preferred to the Kirchhoff current law, because matrices are better conditioned for solution with iterative matrix equation solver routines [41]. Use of the Kirchhoff voltage law leads to a problem where the unknowns

are currents through meshes in the circuit. The necessary number of meshes is determined by the circuit topology [32] (fundamental meshes). Meshes with minimum number of edges however can only be found with an iterative procedure [77]. FastHenry solves the circuit equations in the frequency domain for given total port currents. The inductance is calculated from the complex impedance Eq. (2.55).

5.3.1 Examples

This section gives some examples to show the efficiency of the FastHenry algorithm. Results from the algorithm can be compared with results from static inductance extraction algorithms, when the frequency of the applied current is low, such that the skin effect does not alter the current density distribution. The current density distribution is not altered by an alternating magnetic field, when the skin depth Eq. (2.74) is large compared to the diameter of conductors. The computational effort is compared in a different way. Each matrix vector product executed by the FastHenry algorithm during the iterative matrix equation solution process corresponds to one energy estimate of the newly developed Monte Carlo algorithm Chap. 4. The relative error 0.001 of the calculated energy is given by Eq. (5.11). Note that this error is independent of current distributions. In order to compare the computational effort of the energy estimate by means of Monte Carlo sampling with the multipole algorithm used by FastHenry, the number of FastHenry solver iterations is limited to one and the preconditioner of FastHenry is switched off. All simulations have been performed on a 832M Sun Ultra 2 Model 2170 with 2x167 MHz.

5.3.2 Meander and Coil

This section presents another analysis of the meander and coil conductor geometries shown in Fig. 3.9 from Sec. 3.4 and Sec. 4.7.3. Structured grid models are translated into PEEC models as described in Sec. 5.3.

Table 5.1 can be compared directly with Tab. 4.5. Since during the PEEC analysis the current density is modeled with bricks, the number of bricks is given instead of the number of degrees of freedom. As has been explained in the previous section Sec. 5.3.1 one matrix vector product of

Model	Bricks	Time	R [Ω]	L [H]
Meander (c)	1541	10 s	$7.92 \cdot 10^1$	$8.05 \cdot 10^{-11}$
Meander (f)	27108	369 s	$7.75 \cdot 10^1$	$7.96 \cdot 10^{-11}$
Coil (c)	3509	40 s	$3.07 \cdot 10^2$	$4.07 \cdot 10^{-9}$
Coil (f)	65936	1815 s	$3.03 \cdot 10^2$	$4.08 \cdot 10^{-9}$

Table 5.1: (c) and (f) denote coarse and fine models respectively. Bricks denotes the number of bricks in the PEEC model. Time denotes the time spent for setting up the multipole structure and for executing one matrix vector product. R and L are the results.

Model	Meshes	Memory	Time
Meander (c)	1	10 MB	10 s
Meander (f)	12324	270 MB	2450 s
Coil (c)	1	24 MB	41 s
Coil (f)	28030	500 MB	3215 s

Table 5.2: As in Tab. 5.1 (c) denotes coarse models and (f) denotes fine models. Meshes denotes the number of fundamental meshes in the PEEC circuit. Memory is the amount of memory allocated by FastHenry. Time denotes the time spent for solving the circuit equation for one frequency.

the FastHenry program corresponds to evaluation of the magnetic field energy with the Monte Carlo sampling algorithm. Timing results are given for coarse (c) and fine (f) models, where the coarse model was used during the analysis of the Finite Element Method and Monte Carl sampling method. Refined models were constructed by dividing each element of the structured grid model into eight parts.

Corresponding memory requirements of the FastHenry algorithm and the total time for solution of the circuit equation are shown in Tab. 4.5.

The required amount of memory obviously strongly increases with increasing number of PEEC bricks. The time spent for the solution of the circuit equation increases, too. Despite the fact that modeling the skin effect is theoretically possible it is not feasible due to the large amount of memory required (for a coarse resolution of the skin effect each structured grid element has to be divided at least three times). The coarse resolution however is sufficient for the static inductance extraction in this case. Results are in good agreement with those obtained from the

Grid	Meshes	Memory	Time
coarse	729	13 MB	406 s
normal	1836	41 MB	2460 s
fine	5496	190 MB	25200 s

Table 5.3: *Time and memory requirements for current density simulations for grid models shown in Fig. 4.15 with FastHenry. Meshes denotes the number of degrees of freedom of the circuit equations. Given times include the computation of 14 frequency points. Inductance and resistance results are given in Fig. 5.4.*

Monte Carlo sampling algorithm (Tab. 4.5). The coil example is simulated as quick as with the Monte Carlo algorithm. The meander example is simulated faster.

5.3.3 Substrate

In this section the substrate conductor geometry Fig. 4.14 from Sec. 4.7.2 is analyzed with the PEEC method. The time and memory requirements of FastHenry are given in Tab. 5.3.

Figure 5.4 shows the computed resistance and inductance values. The results from the current density computation by means of the Finite Element Method and subsequent energy estimate with Monte Carlo sampling are given, too. These results do not change with frequency, whereas the frequency dependent FastHenry results show an increase of the resistance (which corresponds to higher current densities at the surface of the conductor) and a decrease of the inductance (which corresponds to decrease of the magnetic field energy since the inner of the substrate is field free at high frequencies).

Note the saturation of resistance and skin effect due to coarse resolutions of the PEEC model. Since the same grids were used for simulation with different methods, the convergence for grid refinement can be compared directly. Assuming that the adaptively refined current distribution Fig. 4.16 yields the correct static inductance and resistance values, static resistance results converge faster when the current distribution is calculated with the Finite Element Method. Both PEEC and Finite Element Method converge similarly for static inductance extraction.

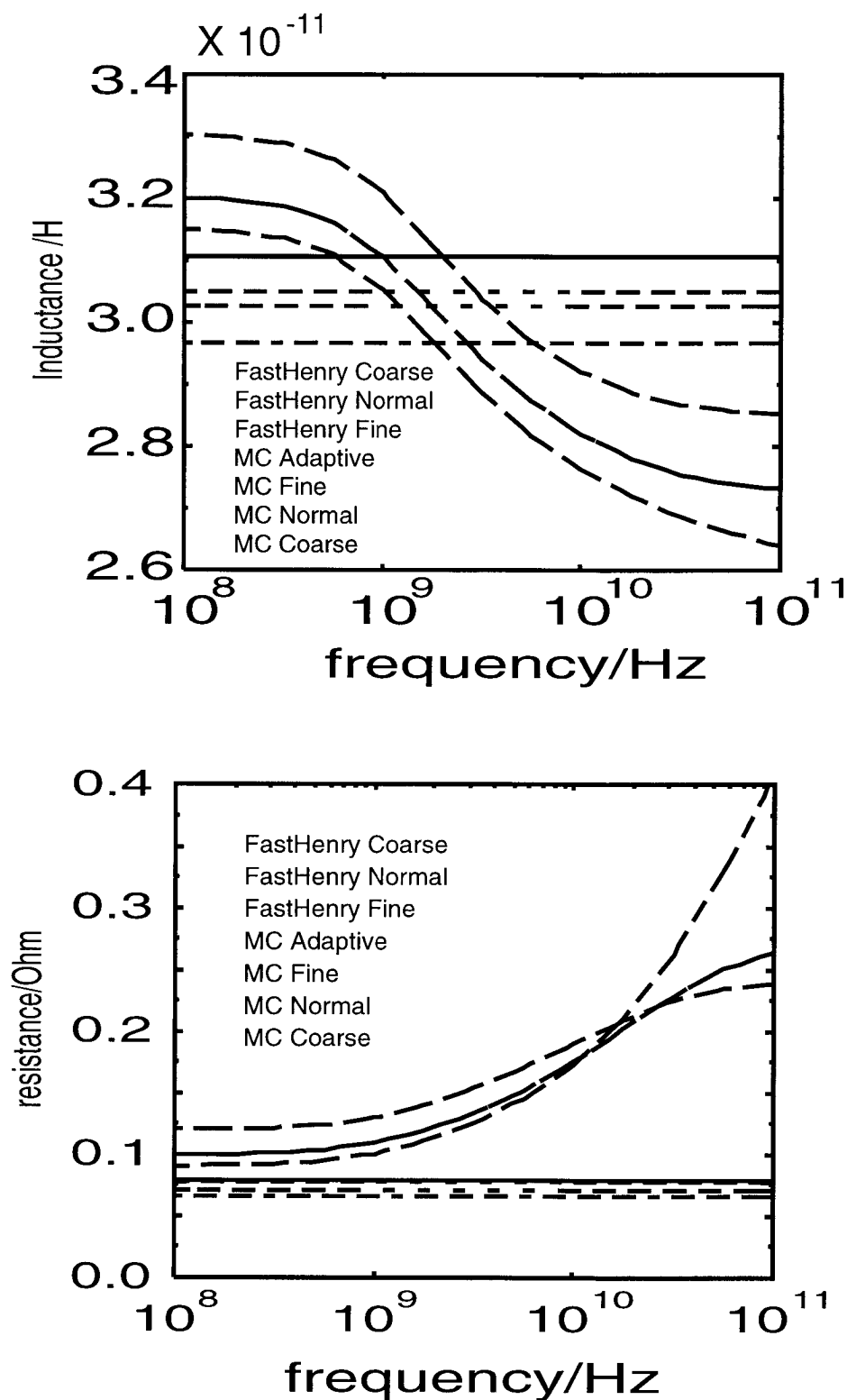


Figure 5.4: Top: resistance, bottom: inductance of the substrate geometry shown in Fig. 4.14. The order of the legends corresponds to the order of the curves on the left side of the diagrams. Legends indicate the used method and the grid model from Fig. 4.15.

5.4 Conclusions and Outlook

It has been shown that the newly developed static inductance extraction by means of Monte Carlo sampling method is better than inductance extraction with a floating random walk. An extension of Monte Carlo methods towards current density simulations under the quasistatic approximation does not seem feasible.

The PEEC method for current density simulations has been reviewed. Several hierarchical methods have been discussed which can be used for a direct evaluation of the magnetic vector potential. For all shown examples a direct evaluation of the magnetic vector potential performs better than evaluation by means of the Finite Element Method. Small geometries are simulated very rapidly. When the number of unknowns increases, the time and memory requirements of the investigated multipole algorithm increases that much, that a simulation of the IGBT busbar geometry shown in Fig. 4.18 was not feasible (with the automatically generated grid). A performance increase of hierarchical methods is limited by the minimum number of operation $n \log n$, where n denotes the number of unknowns. Hence, a better performance can only be achieved at the cost of accuracy. However, due to the properties of the inductance matrix listed in Sec. 2.5.4 – in contrast to the properties of the capacitance matrix – it seems that high accuracy is required even for distant PEEC bricks.

In order to better exploit the hierarchical algorithms it is expedient to save as much degrees of freedom as possible used for modeling the current density distributions. In order to simulate more complicated geometries under the quasistatic approximation it is therefore suggested to use edge elements [78], mixed element grids and adaptive grid refinement schemes instead of bricks with constant current density. Current continuity would have to be assured at grid nodes. Moreover use of edge elements would allow to model non rectilinear conductor geometries, which is not possible with the shown PEEC algorithm. When adaptive grid refinement techniques require too many degrees of freedom and a simulation of the whole conductor is not feasible due to high memory requirements, it is expedient to divide the conductor into parts. Coupling inductances between conductor parts can be calculated, when two parts are simulated at the same time. The inductive behavior of the complete set of conductor parts can simulated on circuit level, when all coupling inductances

are known.

Comparison With Full Wave Results

This chapter briefly presents a comparison of full wave measurement results, full wave simulation results obtained from the **Finite-Difference Time-Domain** (FD-TD) method [79] and results from circuit simulations of a lumped element equivalent circuit. This example already has been published [80]. Therefore only a brief summary of the results is given here.

FD-TD solves the Maxwell equations Eqs. (2.1c) and (2.1d) in the time domain. Fields $\mathbf{E}(\mathbf{r})$ and $\mathbf{H}(\mathbf{r})$ are discretized on two interleaved finite difference grids. During the first half of a time step Δ_t the magnetic field is advanced in time $\mathbf{H}(\mathbf{r}, t + \Delta_t/2) = \mathbf{H}(\mathbf{r}, t - \Delta_t/2) + f(\mathbf{E}(\mathbf{r}, t))$. During the second half of a time step, the electric field is advanced in time $\mathbf{E}(\mathbf{r}, t + \Delta_t) = \mathbf{E}(\mathbf{r}, t) + f(\mathbf{H}(\mathbf{r}, t + \Delta_t/2))$. The time step Δ_t is bounded by the Courant stability criterion [79]

$$\Delta_t \leq \frac{1}{c \cdot \sqrt{\frac{1}{\Delta x^2} + \frac{1}{\Delta y^2} + \frac{1}{\Delta z^2}}} \quad (6.1)$$

where c is the propagation velocity and Δx , Δy and Δz are the minimum cell spacings of the FDTD grid. The electromagnetic behavior of a structure can be characterized by scattering parameters.

$$S_{ab}(f_i) = \frac{U_{a,scat}(f_i)}{U_{b,inc}(f_i)} \cdot \frac{\sqrt{Z_{0,b}}}{\sqrt{Z_{0,a}}} \quad (6.2)$$

In Eq. (6.2) S_{ab} is the scattering parameter between ports a and b , $Z_{0,a}$ and $Z_{0,b}$ are the impedances of connecting transmission lines and

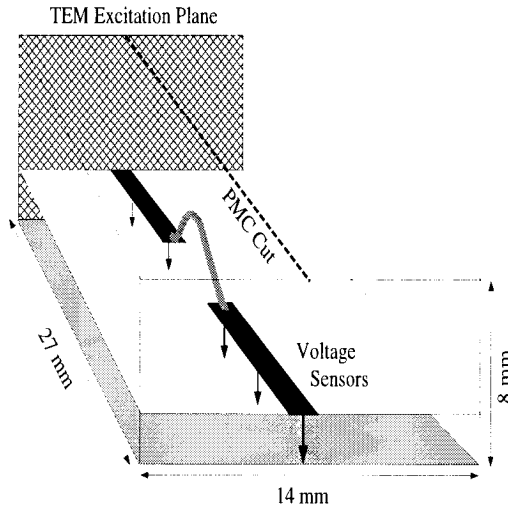


Figure 6.1: *Simulation domain with bonding wire and connecting transmission lines. The bottom is bounded by an ideally conducting ground plane. Symmetry is exploited by introducing a perfect magnetic conductor $\mathbf{H}(\mathbf{r}) \times \mathbf{n}(\mathbf{r}) = 0$ in the middle of the simulation domain. Only one half is simulated by the FD-TD algorithm.*

$U_{a,scat}(f_i)$, $U_{b,inc}(f_i)$ are frequency dependent port voltages. Here scattered voltage and incoming voltage from scattered waves and incoming waves respectively are distinguished. Incoming and scattered waves are separated by performing two simulations. One simulation is performed without the scattering structure and one simulation is performed with the scattering structure. Frequency data are obtained from time domain results by means of an FFT, where the discrete frequency points f_i are given by:

$$f_i = i \cdot \frac{1}{T} \quad (i = 0, 1, \dots, N/2 + 1). \quad (6.3)$$

In Eq. (6.3) N is the (even) number of time steps simulated and $T = N \cdot \Delta t$ is the simulation time.

6.1 Bonding Wire With FD-TD

This section presents the FD-TD analysis of the bonding wire shown in Fig. 6.1. The figure shows the simulation domain with a bonding wire inside. The bonding wire is connected with two transmission lines. The ground plane below is a perfect conductor. The symmetry of the system is exploited by inserting a symmetry plane and simulating only one half of the structure. The minimum grid spacing is $50\mu\text{m}$, a stable time step Eq. (6.1) is $\Delta t = 100\text{fs}$. The total simulation time is 0.5ns . This leads to a total of 5000 time steps and a frequency spacing Eq. (6.3) of

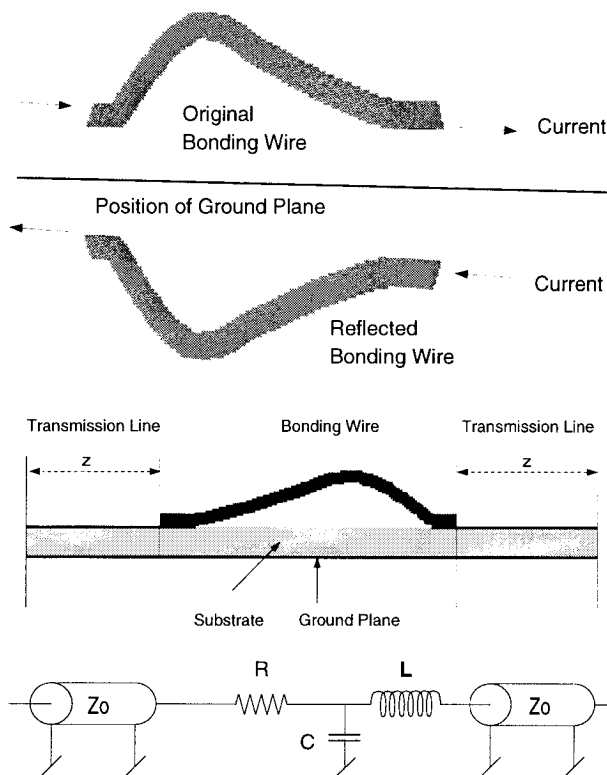


Figure 6.2: *Bonding wire and explicitly reflected bonding wire for modeling the ideal conducting ground plane.*

Figure 6.3: *Cut through model and equivalent circuit model with transmission lines and lumped elements R , L and C .*

$\Delta f = 2\text{GHz}$. Due to the large number of time steps, simulation time was $46.8 \cdot 10^3\text{s}$ and 245MB of memory were allocated.

6.2 Bonding Wire With Monte Carlo Algorithm

This section presents lumped circuit parameter extraction of the same model as investigated in the previous section. Since the Monte Carlo algorithm for static inductance extraction cannot model ideal ground planes, the boundary condition Eq. 3.3) has to be enforced explicitly by adding a mirrored current distribution to the model. Both bonding wire and mirrored bonding wire are shown in Fig. 6.2.

Figure 6.3 shows the equivalent circuit model with resistance, inductance and capacitance. Simulation of the required current density distribution took 75s with 75MB of memory. Subsequent inductance extraction required another 10s with use of variance reduction techniques and 80MB of memory. The capacitance was computed with SOLIDIS_{ISE} on a coarsened grid with 450MB of memory in 600s.

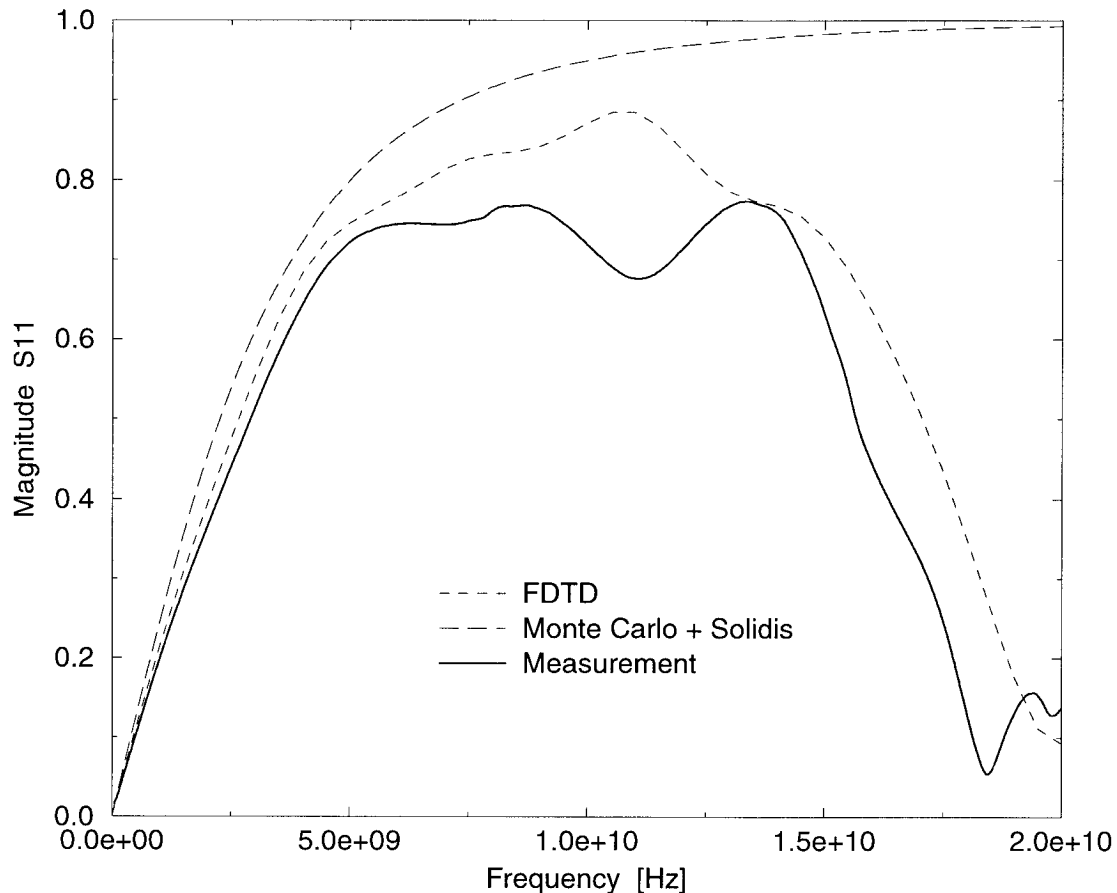


Figure 6.4: Results for the return loss obtained from measurement, full wave simulation and lumped element model generated with the Monte Carlo sampling method for inductance extraction and $SOLIDIS_{ISE}$ for capacitance and resistance extraction.

The corresponding scattering parameter is calculated with [81]

$$S_{11} = \frac{j\omega Z_0^2 C - j\omega^3 L^2 C/4 + j\omega L}{j\omega Z_0^2 C - \omega^2 LC Z_0 + 2Z_0 - \omega^3 L^2 C/4 + j\omega L}, \quad (6.4)$$

where the resistance is neglected.

6.3 Results

Figure 6.4 shows the results which match quite well also with measurement results. The lumped model predicts the low frequency behavior quite accurately, whereas a resonance can only be modeled with the FD-

TD algorithm. Due to Eq. (6.3) even lower frequency resolution would be more costly with the FD-TD algorithm.

6.4 Conclusion

Simulation methods should be used according to the interesting frequency range. When radiation effects are interesting, lumped element models cannot be used. Use of lumped element models however is expedient in the low frequency range.

Seite Leer /
Blank leaf

Conclusions

The main contribution of this work is the development of new method for static inductance extraction by means of Monte Carlo sampling. The method needs an appropriate set of current distributions inside conductors, which is simulated with the Finite Element program `SOLIDISISE` during this work. Memory requirements are minimal, i.e. only the current density and geometry information has to be stored. Convergence has been analyzed for general classes of geometry and for some examples. Several variance reduction methods have been combined for accelerated convergence. The new method provides an absolute error for given results which makes it useful for industrial applications. Once an error is predefined, the sampling procedure stops only when the actual error is smaller than the predefined error.

The new method has been integrated into a TCAD environment, where lumped element *RLC* circuit models are generated from conductor geometries automatically. Capacitances in the lumped element circuit model are simulated with the Finite Element program `SOLIDISISE`. The validity of the generated circuit models has been investigated on a theoretical basis and by comparison with full wave simulation and measurement results. For evaluation on a theoretical basis circuit models are derived from the complete set of Maxwell equations. During derivation emphasis is put on common and different features of inductance, resistance and capacitance extraction in order to show difficulties as well as possible simplifications.

Examples given for the new method have been simulated with the Finite Element Method and with the Partial Element Equivalent Circuit

Method when possible. It is shown that the Partial Element Equivalent Circuit Method with its direct integration of the magnetic vector potential is superior to a computation of the magnetic vector potential by means of the Finite Element Method. Direct integration of the magnetic vector potential however limits the size of Partial Element Equivalent Circuit models. The new Monte Carlo method can be competitive with the Partial Element Equivalent Circuit method even for small examples. An example is shown which cannot neither be simulated with the Partial Element Equivalent Circuit method, nor with the Finite Element Method.

An outlook has been given on possible future developments towards inductance extraction under the quasistatic approximation, which includes modeling of the skin effect.

Vector Calculus

Throughout this work all vector variables are marked with **bold** letters. All matrices are underlined, i.e. **M**.

A.1 Vector Calculus

The following well known formulas for vector calculus are taken from [25].

$$\nabla(\mathbf{a} \times \mathbf{b}) = \mathbf{b}(\nabla \times \mathbf{a}) - \mathbf{a}(\nabla \times \mathbf{b}) \quad (\text{A.1})$$

$$\nabla \times \nabla \times \mathbf{a} = \nabla \nabla \mathbf{a} - \Delta \mathbf{a} \quad (\text{A.2})$$

A volume integral can be transformed into a surface integral with Green's theorem

$$\begin{aligned} \int_V \Psi(\mathbf{r}) \Delta \Phi(\mathbf{r}) - \Phi(\mathbf{r}) \Delta \Psi(\mathbf{r}) d^3 r \\ = \int_{\Gamma} (\Psi(\mathbf{r}) \nabla \Phi(\mathbf{r}) - \Phi(\mathbf{r}) \nabla \Psi(\mathbf{r})) \mathbf{n}(\mathbf{r}) d^2 r, \end{aligned} \quad (\text{A.3})$$

where Φ and Ψ are scalar fields, V and Γ denote the integration volume and closed surface respectively and $\mathbf{n}(\mathbf{r})$ stands for the normal vector pointing out of Γ at position \mathbf{r} .

A.2 Time Average of Complex Vector Fields

In [25] it is shown for harmonically varying vector fields, that

$$\overline{\mathbf{X}(\mathbf{r})\mathbf{Y}(\mathbf{r})} = \frac{1}{2}\Re\{\mathbf{X}^*(\mathbf{r})\mathbf{Y}(\mathbf{r})\}. \quad (\text{A.4})$$

This formula is frequently needed during the evaluation of average field energies.

A.3 Divergence of the Magnetic Vector Potential

Despite enforcement of the Coulomb Gauge $\nabla\mathbf{A} = 0$ it shall be noted that $\nabla\mathbf{A} \neq 0$ once current continuity is not fulfilled. With Coulomb Gauge enforced the magnetic vector potential can be calculated with Eq. (2.28) for a given current density. The divergence of this expression becomes

$$\begin{aligned} \nabla_r\mathbf{A}(\mathbf{r}) &= \nabla_r\left(\frac{\mu}{4\pi}\int_V\frac{\mathbf{J}(\mathbf{r}')}{|\mathbf{r}-\mathbf{r}'|}d^3r'\right) \\ &= \frac{\mu}{4\pi}\int_V\mathbf{J}(\mathbf{r}')\nabla_r\frac{1}{|\mathbf{r}-\mathbf{r}'|}d^3r \\ &= -\frac{\mu}{4\pi}\int_V\mathbf{J}(\mathbf{r}')\nabla_{r'}\frac{1}{|\mathbf{r}-\mathbf{r}'|}d^3r \\ &= \frac{\mu}{4\pi}\int_V\frac{1}{|\mathbf{r}-\mathbf{r}'|}\nabla_{r'}\mathbf{J}(\mathbf{r}') - \nabla_{r'}\frac{\mathbf{J}(\mathbf{r}')}{|\mathbf{r}-\mathbf{r}'|}d^3r' \end{aligned} \quad (\text{A.5})$$

The first term in Eq. (A.5) vanishes when $\nabla\mathbf{J}(\mathbf{r}) = 0$. For the second term a sphere with radius R around \mathbf{r} is considered and for evaluation spherical coordinates are used. It then turns out that the second term vanishes when the same amount of current enters and leaves the sphere, i.e. when current continuity is fulfilled. Hence $\nabla\mathbf{A} \neq 0$ when $\nabla\mathbf{J} \neq 0$.

Symbols

The following symbols are used for labelling variables throughout this thesis.

D	[A/m ²]	the electric displacement current,
B	[Wb]	the magnetic induction or magnetic flux density,
E	[V/m]	the electric field
H	[A/m]	the magnetic field,
J	[A/m ²]	the electric current density.
ρ	[C/m ²]	Electric surface charge density
Q	[C]	Total charge
W	[J]	Total energy
$W_{e,m}$	[J]	Total electric, magnetic field energy
σ	[S/m]	Electrical conductivity
ε	[F/m]	the dielectric permittivity

The following symbols are used for labelling lumped circuit parameters throughout this thesis.

R	[Ω]	Ohmic resistance
Z	[Ω]	(Complex) impedance
L	[H]	Inductance
I	[A]	Current
U	[V]	Voltage
P	[W]	Power

B.1 Static Self- and Mutual-Inductance of Rectangular Conductors

Hoer [35] derived analytical expressions for self and mutual inductances of parallel rectangular conductors with constant current density. His equations can also be applied to self and mutual partial capacitances of rectangular plates with constant surface charge.

He calculated inductances from the magnetic field energy with Eq. (2.52d). The self inductance of a rectangular conductor with cross section $a \cdot b$ and length l is given by

$$L = \frac{\mu}{4\pi a^2 b^2} \int_0^a \int_0^b \int_0^l \int_0^a \int_0^b \int_0^l \frac{1}{\sqrt{(x-x')^2 + (y-y')^2 + (z-z')^2}} dz' dy' dx' dz dy dz, \quad (\text{B.1})$$

where the factor $a^2 b^2$ accounts for the square of the current density $J^2 = I^2/(a^2 b^2)$ with I the total conductor current. The analytic expression is rather lengthy.

$$L = \frac{\mu}{4\pi a^2 b^2} \left[\left[[f(x, y, z)]_{0,0}^{-a,a}(x) \right]_{0,0}^{-b,b}(y) \right]_{0,0}^{-l,l}(z), \quad (\text{B.2})$$

with

$$\begin{aligned}
 f(x, y, z) = & \frac{1}{\sqrt{y^2 + z^2}} \left(\frac{1}{4} y^2 z^2 - \frac{1}{24} y^4 - \frac{1}{24} z^4 \right) \log(x + \sqrt{x^2 + y^2 + z^2}) \\
 & + \frac{1}{\sqrt{x^2 + z^2}} \left(\frac{1}{4} x^2 z^2 - \frac{1}{24} x^4 - \frac{1}{24} z^4 \right) \log(y + \sqrt{x^2 + y^2 + z^2}) \\
 & + \frac{1}{\sqrt{x^2 + y^2}} \left(\frac{1}{4} x^2 y^2 - \frac{1}{24} x^4 - \frac{1}{24} y^4 \right) \log(z + \sqrt{x^2 + y^2 + z^2}) \\
 & + \frac{1}{60} (x^4 + y^4 + z^4 - 3x^2 y^2 - 3y^2 z^2 - 3x^2 z^2) \sqrt{x^2 + y^2 + z^2} \\
 & - \frac{1}{6} x y z^3 \arctan\left(\frac{xy}{z\sqrt{x^2 + y^2 + z^2}}\right) \\
 & - \frac{1}{6} x y^3 z \arctan\left(\frac{xz}{y\sqrt{x^2 + y^2 + z^2}}\right) \\
 & - \frac{1}{6} x^3 y z \arctan\left(\frac{xy}{z\sqrt{x^2 + y^2 + z^2}}\right)
 \end{aligned} \tag{B.3}$$

and

$$\begin{aligned}
 & \left[\left[[f(x, y, z)]_{q_2, q_4}^{q_1, q_3}(x) \right]_{r_2, r_4}^{r_1, r_3}(y) \right]_{s_2, s_4}^{s_1, s_3}(z) \\
 & = \sum_{i=1}^4 \sum_{j=1}^4 \sum_{k=1}^4 (-1)^{i+j+k+1} f(q_i, r_j, s_k). \tag{B.4}
 \end{aligned}$$

This approach is quite complicated and hence time consuming. Hoer himself gave an approximative formula for conductors with small thickness to width ratio.

Integration for mutual inductive coupling is similar, Here, only the integration limits are changes accordingly.

Seite Leer /
Blank leaf

Bibliography

- [1] S. Ramo, J. Whinnery, and T. v. Duzer, *Fields and Waves in Communication Electronics*. New York: John Wiley & Sons, Inc., 1965.
- [2] H. W. Johnson and M. Graham, *High-Speed Digital Design : A Handbook of Black Magic*. Englewood Cliffs, NJ: PTR Prentice Hall, 1993.
- [3] Interational Sematech, *International Technology Roadmap for Semiconductors*. Austin: <http://www.sematech.org>, 1999.
- [4] Siemens Semiconductor Group, *IGBT Power Semiconductors IGBT Modules Data Book 05.96*. Munchen: Siemens AG, 1996.
- [5] ISE Integrated Systems Engineering AG, *LIGAMENT-ISE User Manual and Reference*. Zurich: ISE AG, 1997.
- [6] ISE Integrated Systems Engineering AG, *PROSIT-ISE User Manual and Reference*. Zurich: ISE AG, 1997.
- [7] ISE Integrated Systems Engineering AG, *DFISETOOLS-ISE User Manual and Reference*. Zurich: ISE AG, 1997.
- [8] ISE Integated Systems Engineering AG, *SOLIDIS-ISE User Manual and Reference*. Zurich: ISE AG, 1997.
- [9] ISE Integrated Systems Engineering AG, *TED-ISE User Manual and Reference*. Zurich: ISE AG, 1999.
- [10] G. Leonhardt, C. Hager, P. Regli, and W. Fichtner, "Inductance extraction by means of the monte carlo method," *Proceedings of the MSM'98 Conference, Santa Clara CA 1998*, pp. 671–675, 1998.
- [11] G. Leonhardt and W. Fichtner, "Acceleration of inductance extraction by means of the monte carlo method," *Proceedings of the MSM'99 Conference, San Juan PR 1999*, pp. 225–228, 1999.
- [12] C. Schuster, *Simulation, Analysis and Parameter Extraction of Electronic Components and Circuits Using the Finite-Difference Time-Domain Method*. Konstanz: Hartung-Gorre, first ed., 2000.

- [13] G. Leonhardt and W. Fichtner, "Inductance extraction by means of the monte carlo method and variance reduction techniques for acceleration," *Journal of the MSM*, vol. 1, 2000.
- [14] ISE Integrated Systems Engineering AG, *INDEX-ISE User Manual and Reference*. Zurich: ISE AG, 1999.
- [15] Avant Corporation, *Star-Hspice Manual Release 1998.2*. Fremont, CA: Avant Corporation and Avant! Subsidiary, 1998.
- [16] J. C. Maxwell, *A Treatise on Electricity and Magnetism*. New York: Dover Publications, 1954.
- [17] C. W. Steele, *Numerical Computation of Electric and Magnetic Fields*. New York, NY: International Thomson Publishing, 1996.
- [18] R. J. Luebbers and F. Hunsberger, "FDTD for nth-order dispersive media," *IEEE Trans. Antennas and Propagation*, vol. 40, pp. 1297–1301, 1992.
- [19] R. J. Luebbers, D. Steich, and K. Kunz, "FDTD calculation of scattering from frequency-dependent materials," *IEEE Trans. Antennas and Propagation*, vol. 41, pp. 1249–1257, 1993.
- [20] N. Chang, L. Barford, and B. Troyanowsky, "Fast time domain simulation in spice with frequency domain data," in *Proceedings of the 47th Electronic Components and Technology Conference*, 1993.
- [21] S. D. Corey and A. T. Yang, "Interconnect characterization using tie domain reflectometry," *IEEE Trans. on Microwave Theory and Techniques*, vol. 43, no. 9, pp. 2151–2156, 1995.
- [22] L. M. Sileira, M. Kamon, and J. White, "Algorithms for coupled transient simulation of circuits and complicated 3-d packaging," *IEEE Trans. on Components Packaging Manufacturing and Technology*, vol. 18, no. 1, pp. 92–98, 1995.
- [23] E. Chiprout and M. Nakhla, *Asymptotic Waveform Evaluation and Moment Matching for Interconnect Analysis*. Boston, MA: Kluwer Academic Publishers, 1994.
- [24] P. Feldmann and R. Freund, "Efficient linear circuit analysis by pade approximation via the lanzcos process," *IEEE Trans. on Computer-Aided Design of Integrated Circuits and Systems*, vol. 14, no. 5, pp. 639–649, 1995.
- [25] J. D. Jackson, *Classical Electrodynamics*. New York: John Wiley & Sons, second ed., 1982.
- [26] R. G. Olsen, "Power-transmission electromagnetics," *IEEE Antennas Prop. Mag.*, vol. 36, no. 6, pp. 7–16, 1994.
- [27] A. Ruehli, *Advances in CAD for VLSI Vol. 3 – Part 2: Circuit Analysis, Simulation and Design*. Amsterdam: North-Holland, 1987.

- [28] P. A. B. A. E. Ruehli, "Efficient capacitance calculations for three-dimensional multiconductor systems," *IEEE Trans. on Microwave Theory and Technique*, vol. MTT-21, no. 2, pp. 76–82, 1973.
- [29] Y. Saad and A. Sameh, "A parallel block stiefel method for solving positive definite systems," in *Elliptic Problem Solvers* (M. H. Schultz, ed.), pp. 405–412, New York: Academic Press, 1981.
- [30] A. Konrad, "Integrodifferential finite element formulation of two-dimensional steady-state skin effect problems," *IEEE Transactions on Magnetics*, vol. MAG-18, no. 1, pp. 284–292, 1982.
- [31] A. Ruehli, "Inductance calculations in a complex integrated circuit environment," *IBM J. res. Develop.*, vol. 16, no. 5, pp. 470–81, 1972.
- [32] M. Swamy and K. Thulasiraman, *Graphs, Networks and Algorithms*. New York: John Wiley & Sons, 1981.
- [33] O. Biro and K. Richter, "Cad in electromagnetism," *Advances in Electronics and Electron Physics*, vol. 82, pp. 1–96, 1991.
- [34] S. Ratnajeevan and H. Hoole, *Finite Elements, Electromagnetics and Design*. Amsterdam: Elsevier, 1995.
- [35] C. L. C. Hoer, "Exact inductance equations for rectangular conductors with applications to more complicated geometries," *Journal of research of the National Bureau of Standards*, vol. 69C, no. 2, pp. 127–37, 1965.
- [36] J. Strain, "Locally corrected quadrature rules for singular functions," *SIAM J. Scientific Computing*, pp. 1447–1459, 1995.
- [37] F. Grover, *Inductance Calculations*. New York: van Nostrand Co., 1946.
- [38] C. S. Walker, *Capacitance, Inductance and Crosstalk Analysis*. Boston, MA: Artech House, first ed., 1990.
- [39] R. L. Stoll, *The Analysis of Eddy Currents*. Oxford: Clarendon Press, 1974.
- [40] J. A. Tegopoulos and E. E. Kriezis, *Eddy Currents in Linear Conducting Media*. Amsterdam: Elsevier, first ed., 1985.
- [41] M. Kamon, *Fast Parasitic Extraction and Simulation of Three-dimensional Interconnect via Quasistatic Analysis*. Boston, MA: PhD Thesis Massachusetts Institute of Technology, 1998.
- [42] O. Zienkiewicz, *The Finite Element Method*. New York: McGraw-Hill, first ed., 1977.
- [43] J. Jin, *The Finite Element Method in Electromagnetics*. New York: John Wiley & Sons, first ed., 1993.
- [44] C. Crowley and P. Silvester, "Ballooning and infinitesimal scaling for unbounded field problems," *Computer Aided Engineering Journal*, vol. 3, no. 5, pp. 213–16, 1986.

- [45] I. Babuska, O. Zienkiewicz, J. Gago, and E. de A. Oliveira, *Accuracy Estimates and Adaptive Refinements in Finite Element Computations*. New York: John Wiley & Sons, first ed., 1986.
- [46] V. Jandhyala and E. M. abd R. Mittra, "A sparse multiresolution technique for fast capacitance comutation," *Microwave and Optical Technology Letters*, vol. 11, no. 5, pp. 242–247, 1996.
- [47] S. Putot and P. Witomski, "A fast and accurate computation of interconnect capacitance," *Proceeding of the IEDM'99*, pp. 893–896, 1999.
- [48] C. R. I. Emson, "Methods for the solution of open-boundary electromagnetic-field problems," *IEE Proceedings–A*, vol. 135, no. 3, pp. 151–158, 1988.
- [49] J. Shen, *Computational Electromagnetics using Boundary Elements Advances in Modelling Eddy Currents*. Southampton: Computational Mechanics Publications, first ed., 1995.
- [50] B. H. McDonald and A. Wexler, "Finite-element solution of unbounded field problems," *IEEE Trans. on Microwave Theory and Techniques*, vol. MTT-20, no. 12, pp. 841–847, 1972.
- [51] S. Celozzi, "On the finite element time domain solution of the skin effect equation in multiconductor systems," *IEEE Trans. on Magnetics*, vol. 30, no. 3, pp. 3180–3183, 1994.
- [52] O. Biro, P. Boehm, K. Preis, and G. Wachutka, "Edge finite element analysis of transient skin effect problems," *submitted to IEEE Trans. on Magnetics*, 1999.
- [53] R. Rubinstein, *Simulation and the Monte Carlo Method*. New York: John Wiley & Sons, 1981.
- [54] W. Dobosiewicz, "Sorting by distributive partitioning," *Information Processing Letters*, vol. 7, no. 1, pp. 1–6, 1978.
- [55] Y. L. LeCoz and R. B. Iverson, "A stochastic algorithm for high speed capacitance extraction in integrated circuits," *Solid-State Electronics*, vol. 35, no. 7, pp. 1005–1012, 1992.
- [56] M. E. Muller, "Some continuous monte carlo methods for the dirichlet problem," *Ann. Math. Stat.*, vol. 27, pp. 596–589, 1956.
- [57] G. M. Royer, "A monte carlo procedure for potential theory problems," *IEEE Trans. on Microwave Theory ad Techniques*, vol. MTT-19, no. 10, pp. 813–818, 1971.
- [58] J. N. Jere and Y. L. LeCoz, "An improved floating–random–walk algorithm for solving the multi–dielectric dirichlet medium," *IEEE Trans. on Microwave Theory and Techniques*, vol. 41, no. 2, pp. 325–329, 1993.
- [59] Y. L. LeCoz and R. B. Iverson, "A high–speed inductance–extraction algorithm for vlsi multilevel interconnect," *Proceedings of the VMIC Conference*, pp. 456–458, 1992.

- [60] R. F. Harrington, *Field Computation by Moment Methods*. New York: MacMillan, 1968.
- [61] A. Konrad and I. A. Tsukerman, "Application of integral and differential methods to electromagnetic field problems," in *Finite Elements, Electromagnetics and Design* (S. Ratnajeevan and H. Hoole, eds.), pp. 258–341, Amsterdam: Elsevier, 1995.
- [62] A. Greenbaum, *Frontiers in Applied Mathematics Vol. 17 Iterative Methods for Solving Linear Systems*. Philadelphia: Society for Industrial and Applied Mathematics SIAM, 1997.
- [63] J. Barnes and P. Hut, "A hierarchical $O(n \log n)$ force calculation algorithm," *Nature*, vol. 324, pp. 446–449, 1986.
- [64] L. Greengard, *The Rapid Evaluation of Potential Fields in Particle Systems*. Cambridge, Massachusetts: M.I.T. Press, 1988.
- [65] V. Rohklin, "Rapid solution of integral equations of classic potential theory," *J. Comput. Physics*, vol. 60, no. 2, pp. 187–207, 1985.
- [66] F. Zhao, *An $O(N)$ Algorithm for Three-Dimensional N-Body Simulations*. Cambridge, Massachusetts: Master's Thesis. M.I.T., Dept. of Elec. Eng. and Comp. Sci., 1987.
- [67] K. Nabors and J. White, "Fastcap: A multipole accelerated 3-d capacitance extraction program," *IEEE Trans. Computer-Aided Design*, vol. 10, pp. 1447–1459, 1991.
- [68] J. R. Phillips and J. White, "Efficient capacitance extraction of 3d structures using generalized pro-corrected fft methods," in *Proceedings of 1994 IEEE Electrical Performance of Electronic Packaging. 2-4 Nov.*, 1994.
- [69] J. Phillips and J. White, "A precorrected-fft method for electrostatic analysis of complicated 3-d structures," *IEEE Trans. Computer-Aided Design*, vol. 16, no. 10, pp. 1059–1072, 1997.
- [70] R. W. Hockney and J. W. Eastwood, *Computer Simulation Using Particles*. Bristol: Adam Hilger, 1988.
- [71] J. Stoer and R. Bulirsch, *Introduction to Numerical Analysis*. New York, NY: Springer Verlag, 1979.
- [72] S. Kapur and D. Long, "Ies3: Efficient electrostatic and electromagnetic simulation," *IEEE Computer Science & Engineering*, vol. 5, no. 4, pp. 60–67, 1998.
- [73] H. Nelis, P. Dewilde, and E. Deprettere, "Efficient modeling of interconnections in a vlsi circuit," in *Proceedings of the IEEE International Symposium on Circuits and Systems*, 1989.
- [74] H. Nelis, E. Deprettere, and P. Dewilde, "An efficient method for modelling vlsi interconnections," in *Proceedings of the European Conference on Circuit Theory and Design (conf. Publication No.308)*., 1989.

- [75] E. Tuncer, L. B. Taek, and D. Neikirk, "Interconnect series impedance determination using a surface ribbon method," in *Proceedings of 1994 IEEE Electrical Performance of Electronic Packaging. 2-4 Nov. 1994*, 1994.
- [76] J. W. M. Kamon, M.J. Tsuk, "Fasthenry: a multipole-accelerated 3-d inductance extraction program," *IEEE Transactions on Microwave Theory and Techniques*, vol. 42, no. 9, pp. 1750–1758, 1994.
- [77] L. O. Chua and L. Chen, "On optimally sparse cycle and coboundary bases for a linear graph," *IEEE Trans. on Circuit Theory*, vol. CT-20, no. 5, pp. 495–503, 1973.
- [78] J. P. Webb, "Edge elements and what they can do for you," *IEEE Transactions on Magnetics*, vol. 29, no. 2, pp. 1460–1465, 1993.
- [79] A. Tavlove, *Computational Electrodynamics – The Finite-Difference Time-Domain Method*. Norwood, MA: Artech House INC, first ed., 1995.
- [80] C. Schuster, G. Leonhardt, and W. Fichtner, "Electromagnetic simulation of bonding wires and comparison with wide band measurements," *IEEE Trans. on Advanced Packaging*, vol. 23, no. 1, pp. 69–79, 2000.
- [81] K. C. Gupta, R. Garg, and R. Chadha, *Computer-Aided Design of Microwave Circuits*. Dedham: Artech House, 1981.

Curriculum Vitae

I was born in Bremen, Northern Germany, on November 16th, 1967. After finishing High School at Viktoria Luise Gymnasium Hameln and after completing my civilian service I enrolled in Mathematics at the University of Osnabruck also in Northern Germany. Soon I found out that I felt better when dealing with applications rather than with pure theory. Therefore I changed the topic and enrolled in Physics at the same University. After the Prediploma I spent six months at the University of Edinburgh in Scotland whereafter I returned to Germany, in order to finish my Physics degree at the *Westfälische Wilhelms Universität* (WWU) at Munster in 1995. During my diploma thesis I worked on a simplified method for the simulation of plasmas inside **E**lectron **C**yclotron **R**esonance (ECR) Ion sources. The results helped to understand how the confining magnetic field had to be designed such that maximum ion currents could be extracted from the plasma. Since 1996 I have been with the Integrated Systems Laboratory at ETH, *Swiss Federal Institute of Technology, Zurich* where I have worked as a research and teaching assistant in the Electromagnetics group. The main area of research have been various numerical methods for inductance extraction and their integration into the **T**echnology **C**omputer **A**ided **D**esign (TCAD) environment of ISE Integrated Systems Engineering AG as part of a joint university/industry research and development which was funded by the Swiss Priority Program MINAST. Since July 2000 I am with Sun Microsystems where I got the chance to continue my work on inductance extraction.